Studies on Scintillation Properties and Defect Mechanism of Large-size $Bi_4Ge_3O_{12}$ Single Crystals

LANYING YUAN

2022/12

Department of Intelligent Robotics

Toyama Prefectural University

Abstract

Bismuth germanate ($Bi_4Ge_3O_{12}$, hereafter abbreviated as BGO) is an important single crystal scintillator. It has been widely applied in many fields, such as high-energy physics, nuclear medicine, nondestructive inspection, and dark matter detection, among others.

Growth and characterization methods of 600 mm-long BGO crystals are investigated in this thesis. Massive 600 mm-long full-size BGO crystals have been grown by a modified vertical Bridgman (MVB) technique, and these high-quality BGO crystals could meet the increasing requirements of many applications, especially for the project of dark matter detection. The scintillation properties of BGO crystals have been improved effectively in Shanghai Institute of Ceramics, Chinese Academy of Sciences (SICCAS), especially for the optical transmittance, energy resolution (ER), and light response uniformity (LRU). These properties can sufficiently satisfy the application of large-size electromagnetic calorimeters in DArk Matter Particle Explorer (DAMPE) in China.

In the thesis, an intense study focused on one of the hot topics in this area is the formation mechanism of various defects in as-grown BGO crystals by analyzing kinetics on thermal transportation, shape control of the solid–melt interface and surface reaction of $[GeO_4]^{4-}$ and $[BiO_6]^{9-}$ growth units. Two kinds of macro-defects, scattering particles and impurity cores, are often found in as-grown full-size BGO crystals and formed due to unsuitable heating power, temperature gradient and pulling-down speed. The scattering particles generally distributed uniformly in the entire bulk crystal, are caused by a convex solid–melt interface during the crystallization process. The impurity cores generally located at the tail section of 600 mm-long BGO crystals, are resulted from a concave solid–melt interface produced by the over-high heating power to compensate for the thermal dissipation at the later period of crystal growth.

Reddish color, a microdefect exhibiting visible absorption bands, especially from 310 to 390 nm, is occasionally found in the as-grown BGO crystals, particularly at the

later section of the tail. There are no clear correlations between the reddish and colorless BGO crystals in detected impurities.

The reddish color is verified on the reddish color BGO crystals as point defects, cross-checked by several techniques of structure analysis. The $V_o^{\bullet\bullet}$ is confirmed by means of electron paramagnetic resonance (EPR) peaks in the reddish BGO crystals. An intense signal of $g = 2.0035$ is typical of a singly ionized $V_o^{\bullet\bullet}$.

The V_{Bi}''' is verified by scanning electron microscopy-energy dispersive spectroscopy (EDS) analysis, and its existence is also cross-checked by high-angle annular dark-field (HADDF) scanning analysis. Oxygen and Bismuth oxide evaporation at high temperature easily produces $V_o^{\bullet\bullet}$ and V_{Bi}''' during crystal growth, resulting in reddish BGO crystals if the concentration of the defects exceeds a threshold. And bismuth with low valence states may be exist in reddish BGO.

The elimination technique on the reddish color is investigated by annealing in various atmospheres. While annealing in oxidizing atmosphere, oxygen can diffuse into the BGO crystal lattice to compensate $V_o^{\bullet\bullet}$, which treatment could improve the scintillation performances. After many trials, the parameters are optimized as 850 °C for 4 h in oxygen annealing. In this condition, oxygen compensation is accomplished almost completely for $V_o^{\bullet\bullet}$. The EPR intensity of $V_o^{\bullet\bullet}$ decreases, which is in line with X-ray photoelectron spectroscopy (XPS) peaks corresponding to the annealing treatment in the oxidizing atmosphere. However, the intense signal increases after annealing in the non-oxidizing atmosphere because of the formation of more $V_o^{\bullet\bullet}$.

Oxygen annealing can efficiently reduce the $V_o^{\bullet\bullet}$ and produce positive holes. Then, the V_{Bi}''' with three negative charges is recombined with the positive holes to produce optically insert V_{Bi}'''. The perfect lattice is achieved by oxygen compensation during oxygen annealing, and low valence state bismuth is also oxidized to Bi^{3+} when the reddish BGO crystal is annealed in oxygen atmosphere. Consequently, the optical transmission, light output, LRU and ER are improved.

By progress of the growth technique, the optical transmittance is improved at the scintillation wavelength range of 300 – 700 nm. The optical transmittance of the BGO

crystals is achieved at 76.62% in the transverse mode and 72.87% in the longitudinal mode at 480 nm wavelength in full-size (25 mm × 25 mm × 600 mm) BGO crystals provided for DAMPE. The LRU of the full-size BGO crystals is also enhanced by the oxygen annealing. Wrapped with a high-reflectivity material, an enhanced specular reflector film (ESR), almost all the produced BGO crystals could be applicable to DAMPE with excellent performances.

The average ER is approximately 18.80% with the 662 keV γ-ray source for the six positions, where the 600 mm (longitudinal length) BGO crystal is uniformly spaced. The ER is 19.68% when the entire crystal is irradiated from the side with an uncollimated ^{137}Cs. The LRU can be achieved to 2.2%, while the 600 mm-long BGO crystals wrapped with the ESR are measured from the tail end.

The quality and scintillation performances of the full-size BGO crystals can fully satisfy the DAMPE requirements based on the growth mechanism, and the formation of various defects of the crystal have been comprehensively elaborated in this study.

Acknowledgments

I would like to express my greatest appreciation and respect to my supervisors, Professor Tomoaki Karaki and Professor Dong Wang, for their superior help.

Professor Tomoaki Karaki has offered me meticulous guidance, constant encouragement, and selfless help in academic studies. Thanks to his patience, enthusiasm, and erudition, I could complete this thesis well.

Sincere gratitude should go to Professor Dong Wang, whose invaluable ideas, professional suggestions, and strong support are dispensable to this thesis. His knowledge, diligence and dedication inspire me to expand my potential.

I would like to extend my special gratitude to Professor Haosu Luo, who has offered me suggestions, criticisms and encouragements with his profound knowledge and rich experience. I am deeply influenced by his precise attitude to research work. I want to acknowledge Professor Yuntao Wu, whose guidance and insight motivates me intellectually.

I really appreciate Professor Yanlin Huang, who offered me timely and kindly valuable suggestions and help tirelessly when faced with difficulties during the process of writing the thesis. I acknowledge Doctor Yu Wang of Shanghai Synchrotron Radiation Facility, who helped measure the testing, and comprehensively guided and supported the lab experiment.

The work of this thesis mainly relies on BGO research group in SICCAS. I would like to thank the group members: Haihong Ni, Junfeng Chen, Guilan Song, Yun Li, Xuejun Qi, Xiang Li, Shiyun Sun, Yong Du, Peng Zhao, Wenpeng Li, Yugui Lu, Lei Chen, Shaohua Wang, as well as other members of BGO research group, for providing me excellent research environment and helpful discussion. I also want to acknowledge Zhiming Ji, who was actively involved in the project, many work was carried out and accomplished with him together.

I would like to thank Tao Zhang, Nan Wei, Yiqin Sun, Xu Wang, Yi Zhu, Kainan Xiong, and other members of the intelligent systems design engineering laboratory for their encouragement and companionship. I hope them the most successful future research endeavors.

I would like to express sincere gratitude to Toyama Prefectural University, Shanghai Institute of Ceramics, Chinese Academy of Sciences, and all tutors and colleagues for their profound knowledge and important advice to the thesis, who give me great brainstorming and stimulating discussion about this research in the last three years.

I also extend my gratitude to University of Science and Technology of China, Purple Mountain Observatory, Chinese Academy of Sciences, and other research cooperation institutions.

Last but not least, I am deeply indebted to my beloved family for their loving consideration, strong support, and great confidence in the whole Ph.D. studies.

List of Abbreviations

BGO	Bismuth germanate, $Bi_4Ge_3O_{12}$
DAMPE	DArk Matter Particle Explorer
EDS	Energy dispersive spectroscopy
EPR	Electron paramagnetic resonance
ER	Energy resolution
ESR	Enhanced specular reflector
FWHM	Full width at half maximum
GDMS	Glow discharge mass spectroscopy
HAADF	High-angle annular dark-field
HRTEM	High-resolution transmission electron microscopy
LO	Light output
LRU	Light response uniformity
MVB	Modified vertical Bridgman
PET	Positron emission tomography
Ph/MeV	Photons/MeV
PMT	Photomultiplier tube
RT	Room temperature
SAED	Selected area electron diffraction
SEM	Scanning electron microscopy
SICCAS	Shanghai Institute of Ceramics, Chinese Academy of Sciences
STEM	Scanning transmission electron microscopy
TL	Thermoluminescence
T_s	Theoretical transmittance

UV	Ultraviolet
V_{Bi}'''	Bismuth vacancy
$V_o^{\bullet\bullet}$	Oxygen vacancy
XPS	X-ray photoelectron spectroscopy
XRD	X-ray diffraction
Z_{eff}	Effective atomic number
γ-ray	Gamma ray

CONTENTS

Chapter 1 Introduction

1.1 Development and application of inorganic scintillation crystals

1.1.1 Inorganic scintillation crystals

Scintillation is an important domain in radio luminescence science and technology. Scintillators are a kind of materials that can convert high-energy radiation, such as X-ray or γ-ray, into ultraviolet (UV) or visible photons. In such process, radiation or particles are absorbed in a scintillator, and a small part of the energy are changed into UV or visible light. Such conversion process occurs on a time scale of 10^{-9} – 10^{-6} s, forming a fast light pulse upon each absorption in the scintillators.1) The quantity of light pulses and their respective intensity are proportional to what kind of particle and how much energy left in the scintillators, as shown in Fig. 1-1. The light is further processed by transferring the photon signal to an electrical signal. Scintillators could be an inorganic or organic, and crystalline or amorphous. In this thesis, inorganic scintillation crystals will be the focus on owing to their excellent properties for radiation detection.

After the development more than 100 years, scintillators have been widely applied in nuclear medicine, high-energy physics, safety control, homeland security, space physics, and nuclear exploration.2,3)

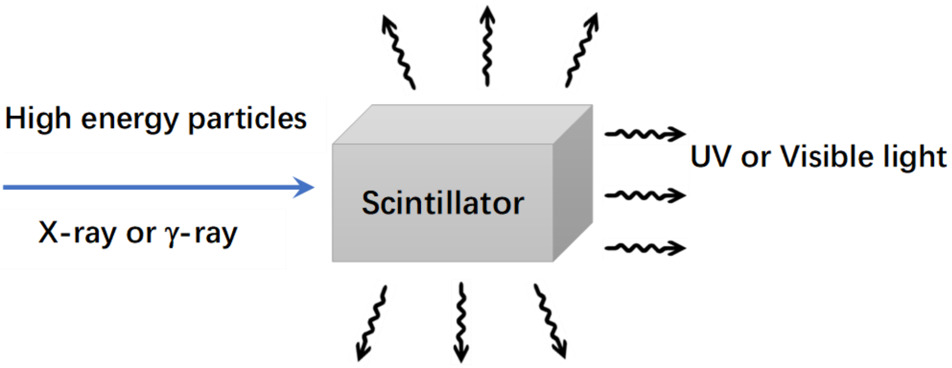

Fig. 1-1 Schematic illustration of principal of a scintillator.2)

1.1.2 Scintillation mechanism

Scintillators are classified based on the luminescence characteristics of luminescent species and radiative processes.4) Scintillation crystals can be simply divided into two types: intrinsic and extrinsic scintillators. Luminescence originated from intrinsic self-activated or extrinsic dopant scintillators has various kinds of radiative transitions, such as the recombination of an electron with a hole, free or impurity-trapped excitons, charge convert and core-valence band transitions.5) Intrinsic scintillators emit photons without introducing dopants, whereas extrinsic scintillators need to introduce an activator, usually rare-earth or transition metal ions, which mainly depends on the introduced doped ions into the scintillator lattice. The incident radiation is directly absorbed by the activator or first absorbed by the matrix lattice, and then it is transferred from the matrix lattice to the activator via carrier migration or energy transfer. Eventually, an excited and electronically activated atom is produced, and these electrons de-excite and decay to the ground state by emitting photons.

1) Intrinsic scintillators

Intrinsic scintillation crystals come in many forms, such as undoped $PbWO_4$, CeF_3 and $Bi_4Ge_3O_{12}$ (BGO) crystals; and they have both high density and fast attenuation, and the comprehensive properties are relatively well. However, for some intrinsic scintillation crystals, light output (LO) is relatively low. They are also usually ion-doped as activator in the crystal lattice to improve scintillation performance from an intrinsic scintillator transformed into to an extrinsic scintillator.

2) Extrinsic scintillators

In general, many ions can be doped in scintillators as activators, and they are usually rare-earth or transition metal ions, including Tl^+, Eu^{2+}, Yb^{3+}, Ce^{3+}, La^{3+}, Nd^{3+}, etc. Among these ions, Ce^{3+} is the most common ion used as activator in scintillation crystals. The luminescence of Ce^{3+} is caused by the 5d → 4f transition, showing large luminescence intensity and fast attenuation. Therefore, the scintillation crystals doped with Ce^{3+} usually have better time resolution and energy resolution (ER).

The inorganic scintillators with good optical performances typically take the form of single crystals composed of various compounds, such as fluorides, halides, oxide, and sulfide. They could be intrinsic scintillators with undoped single crystal (such as CsI and CeF_3) or extrinsic scintillator crystals with dopants (such as Eu^{2+}, Tl^{+}, Nd^{3+} and Ce^{3+}). Some examples of extrinsic scintillators are LaF_3:Nd, $LaBr_3$:Ce, NaI:Tl, Lu_2SiO_5:Ce, and SrI_2:Eu.2) It is important that the scintillation performances could be well studied from the lattice structure and bandgap energy. In a pure inorganic crystal, electrons only occupy discrete energy bands, as shown in Fig. 1-2.5) In the valence band, electrons are basically bound at the local positions.3) Lot of migration-free electrons are occupied conduction band. The forbidden band or band gap is also important related with the middle band of energies, where electrons cannot be found in undoped crystals. In an intrinsic pure crystal, energy absorption occurs when electrons transition across the energy gap, depositing holes in the valence band. In undoped intrinsic scintillator, the de-excitation of an electron with the light emission to the valence band is often ineffective. The band gaps of many undoped intrinsic oxide crystals are large, resulting in higher energy radiation than visible light, which are difficult to detect only with a photomultiplier tube (PMT).4,5)

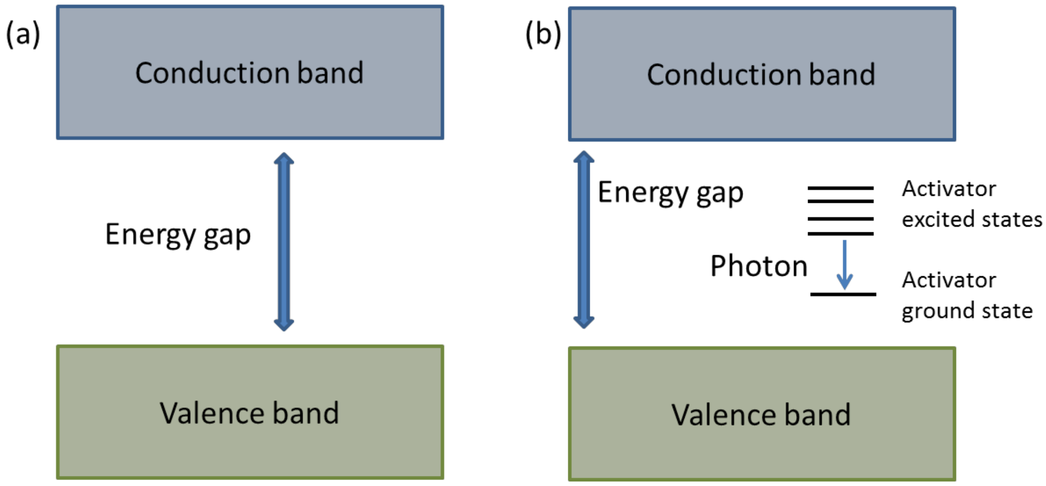

Fig. 1-2 (a) Energy band gap of undoped scintillator crystal and (b) Energyband gap of a dopant inorganic scintillator crystal.5)

The probability of photon emission is usually increased by adding dopants called activators to a crystal lattice. The small number of activators creates special lattice sites, where the energy band is changed from that of the undoped intrinsic crystal. Then, such activators may produce the middle energy levels in the energy band gap, where the electron could de-excite to the valence band that emits lower-energy photons. The de-excitation from the excited energy levels of the activator may lead to luminescence, therefore, de-excitation sites are usually named as luminescent centers.[5,6)]

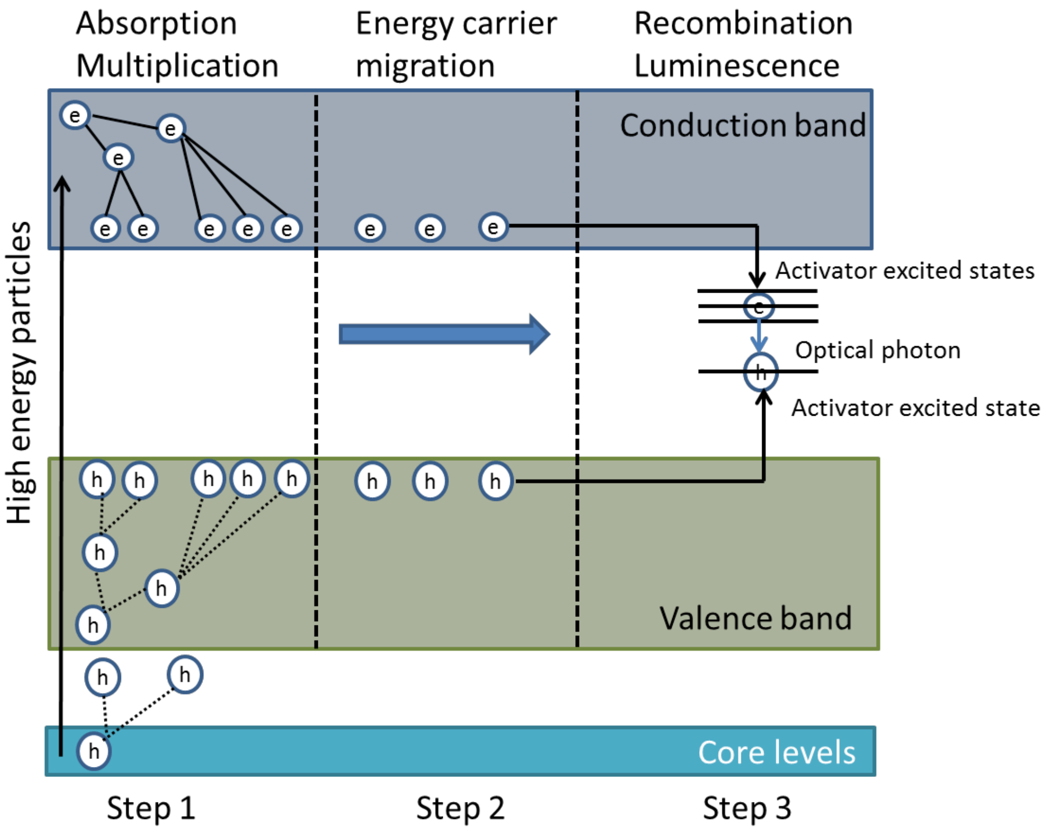

Fig. 1-3 Schematic of three steps of scintillation mechanism in inorganic scintillator.[5)]

The scintillation mechanism of inorganic crystals could be described as three main processes. Firstly, absorbed energy conversion involving the creation of electron-hole pairs, Secondly, thermalization and then migration of electron-hole pairs, and energy conveying to luminescence centers, and the third is recombination of electron-hole pairs to produce luminescence.

While the incident radiation is absorbed by a scintillator crystal, primary electron-hole pairs are created because of the stimulation of electrons from the top of valence band to the bottom of conduction band. High-energy electrons can move freely through the conduction band in the process lose their energy by producing other electron-hole pairs through in elastic Auger processes and electron scattering.$^{6)}$ Secondary electrons can also freely migrate through the lattice, electron-hole pairs are further created. Such process of increased holes and electrons continues till the electron energy decreased below the threshold of ionization electron-hole pairs. At the final process, the electrons and holes thermally excite to the valence band and the conduction band respectively. Then, they will migrate and recombine at the luminescence center of scintillator. If an excited configuration is created by the electron upon recombining with the hole at the luminescence center with a permitted transition to the ground, then it will de-excite with an emission of a photon.

However, if the transition state is forbidden to the ground state, then an additional energy is required by these states to raise them to a relatively high lying state from which it is possible for the de-excitation to the ground. The process results in the emission of photons with the appearance of afterglow and slower decay time in scintillation materials.$^{7)}$

While electrons and holes usually recombine at an activator site, definite types of radiation-less transition or those transition that do not involve the emission of visible light may also occur between the ground energy state and excited energy states. Such process is usually called as quenching, resulting in the reduced scintillation light yield. Moreover, the electron-hole pairs could also migrate together in a loosely associated configuration, which is named as an exciton. These exactions can migrate to luminescent centers and de-excite to the ground, forming scintillation luminescence in this process. Such phenomenon is universal in wide-band-gap halide and oxide scintillation crystals.

The scintillation mechanism of conventional inorganic scintillators is shown in Table 1-1.$^{5)}$

Table 1-1 Radiative transitions of conventional inorganic scintillators.5)

Scintillator	Type	Emission transition
Gd_2O_3: Eu	Extrinsic(activated)	4f-4f
$LaBr_3$: Ce	Extrinsic(activated)	5d-4f
NaI:Tl	Extrinsic(activated)	6p-6s
CeF_3	Intrinsic (self-activated)	5d-4f
BGO	Intrinsic (self-activated)	6p-6s
$CdWO_4$	Intrinsic(self-activated)	Charge transfer
BaF_2	Intrinsic (self-activated)	Core-valence band
CsI	Intrinsic (self-activated)	Self-trapped exciton

1.1.3 Application and properties of scintillators

Scintillation crystals have many important properties, including density, effective atomic number, LO, ER, light response uniformity (LRU), decay time, time resolution, transmittance, refractive index, emission wavelength, absorption coefficient, radiation length, Moliere radius, quality factor, radiation resistance, etc.8) The scintillation properties of conventional inorganic scintillators are listed in Table 1-2. And the fundamental requirements of many scintillation applications are specially introduced as follows.

1.1.3.1 Optical transmittance

A good scintillation crystal should have high transmittance in the region of emission wavelength to be able to obtain sufficient light when they are generated from an emitting scintillator to a PMT. Otherwise, the LO would be reduced significantly, affecting the practical applications. This is the reason why a good scintillation crystal should have high purity, few defects and wide band gap, and high transmittance in the emission spectral region.

Table 1-2 Some common inorganic scintillators, data at room temperature (RT).8)

Scintillator properties		BGO	GSO: Ce	NaI:Tl	CsI:Tl	$CdWO_4$	BaF_2	$PbWO_4$	LYSO:Ce
Emission max., nm	Slow	480		410	565, 420	500	310	420	420
	Fast		400				220		
Light yield, Photons/ MeV	Slow	9, 000		41, 000	66, 000	28, 000		200	25,000
	Fast		1000				1, 500		
Decay time, ns	Slow	0.30	0.6	0.23	0.8 to >6	-3/-17	0.60	15	45
	Fast		60				0.8		
Afterglow (% after 3/100 ms)		0.005/3	-	0.5-5.0/3	>2/0.3	<0.1/0.02	-		
Refractive index		2.15	1.85	1.85	1.80	2.2	1.50		1.82
Density, g/cm^3		7.13	6.71	3.67	4.51	7.9	4.88	8.3	7.15
$\rho Zeff^4, 10^6$		227	84	24.5	38	134	38		65
Radiation length, cm, 511 keV		1.1	1.4	2.6	1.8	1.1	2.0	0.87	1.2
ΔE/E (662 KeV), FWHM, %		9.0	7.8	5.6	4.3	6.8	7.7		
Hygroscopicity		No	No	Yes	Slightly	No	Slightly	No	No

1.1.3.2 Light output

Light yield is the ratio of the number of photons produced by a scintillation process to the energy lost by the charged ions in the scintillator (ph/MeV), also known as the optical output. With a much higher light yield, the more effective the photons can be released after receiving the same radiation energy, and then the higher the detection efficiency.

1.1.3.3 Energy resolution

ER can be described as the detectors' ability to distinguish among radiation events with energies that are extremely close to each other. A good scintillator can distinguish two radiation rays of different energies well after the ER is improved. ER is defined as the full width at half-maximum (FWHM) divided by the height of the peak.

Additionally, ER determines how well photoelectric interactions can be distinguished among scattered events, as shown in Eq. 1-1. In the formula, E is the energy of the annihilation photon, and the FWHM is full-width at the half-maximum of the photopeak at E.9-11)

$$ER = \frac{FWHM}{E} \times 100\% \qquad (1\text{-}1)$$

1.1.3.4 Density and atomic number

In radiation detection, scintillators need to have high blocking ability to ionize radiation, and all radiation incident on luminescent materials should always be absorbed. If radiation pass through the scintillator and are not absorbed, then excitation does not occur. High-density scintillation crystals can block radiation in a short distance, allowing them to be absorbed. Therefore, for scintillation materials to perform well, they need to have a high atomic number and a high density. High density and high atomic number scintillators are universally desirable because increased blocking power reduces the amount of scintillators needed.

1.1.3.5 Decay time

Decay time is a physical quantity representing the speed of light attenuation in a scintillation crystal. It also represents the time required when the ratio of photon number reduces to 1/e, which is an important physical property to characterize inorganic scintillators. All scintillation counting applications require inorganic scintillation crystals to have a fast decay time, so that the ghosting caused by energy accumulation can be eliminated to the greatest extent.

1.1.3.6 Radiation hardness

After long-term exposure in high-dose radiation, scintillation crystals produce certain color center defects in the lattice. After capturing electrons, the scintillation crystals also form defect traps and produce absorptions on the scintillation light emitted by the crystal, hence reducing the transmittance and LO.

Radiation hardness is defined as the threshold of maximum dose radiation for a scintillation detector, which could also be defined as the ratio of reducing LO at the emitting peak.

A good scintillator possesses the following properties: the high-probability of radiation attenuation, ability to generate a large number of light photons per radiation interaction in the shortest time, and ability to allow the light photons from a scintillation crystal towards the photo-sensor.

1.1.3.7 Light response uniformity

Generally, LRU is the most important property for large-size scintillation crystals.12,13) The dependence of light collection on the interaction position of an incident particle can be known as the LRU of scintillators.

Beside the basic requirements, scintillator crystals are required to be transparent around its emission wavelength, to be able to distinguish two radiations with close energy as well as ER, and cost-effective for the fabrication of large-size crystals. The ER is proportional to the atomic number of inorganic scintillators. Inorganic scintillators with large-size are usually particularly rare due to the difficulty for the fabrication. As a result, the large-size inorganic scintillation crystals are only applied in limited scope in large-size detectors.

1.1.4 Research update on inorganic scintillation crystals

Scintillation is an important topic in comprehensively understanding of radioluminescence, in which ionization radiation or particles are absorbed and a partial energy is converted into visible or UV light.1) The amount of light pulses and the intensity are related with the type of particle and the energy left on the scintillation crystal, which is further processed by changing the light signal into an electrical signal. Scintillators can be various forms, such as solid, liquid or gaseous, inorganic or organic, and crystalline or amorphous. In this thesis, the focus is on solid-state inorganic scintillation materials because of their excellent characteristics for radiation detection.

In 1895, the X-ray was discovered by Roentgen via the fluorescence excitation of a barium platinum cyanide scintillator. However, he discovered that this type of material was ineffective in absorbing X-rays prior to conversion into visible light emission. It was also demonstrated by Roentgen that $CdWO_4$ was much more effective changing absorbed X-rays into visible light for recording on photographic films.14) The realization of visible photon emission from some compounds while exposed to radiation resulting in the utilization of scintillators as the radiation detectors. Since then, a lot of compounds have been fabricated and tested for luminesce by X-ray irradiation. Undeniably, scintillators have played an important part in the development of high energy physics and nuclear physics.

α particles was observed by E. Rutherford on a zinc sulfide screen via scintillation. Until 1945, $CdWO_4$ and ZnS were the most common scintillator detector materials applied in nuclear physics. Some data procession techniques from related detection methods, such as electronic counting techniques were later applied by scintillation detectors.

NaI:Tl was discovered in 1947, and it became a widely used scintillation materials. γ particles were detected using used polycrystalline NaI:Tl scintillator by Hofstadter in 1948. Subsequently, single crystals are coupled with a PMT detector to provide spectroscopic information about the energy and type of radiation sources and their energy. Spectroscopic information could only be achieved by means of inefficient methods such as reflection by the use of with proportional gas ionization detectors before this discovery. Spectroscopic information was a huge obtainment in the field of irradiation detection, and it paved the foundation for further development of scintillators. Many compound scintillators, such as CsF, CsI:Na, CaF_2:Eu, and BGO, have been reported as good scintillators in the past two decades.

In the 1980s, significant progress was achieved in scintillator materials because of the demanding requirements of high energy physics and medical diagnosis. The development of lanthanum halides doped by cerium, including $LaCl_3$:Ce and $LaBr_3$:Ce scintillation crystals, yielded new milestone for excellent ER and high light yield in 1997.15,16) However, the disadvantages, such as hygroscopicity, easy cracking, high cost, and small size limited their application of these scintillators. The search for new scintillation materials remains to be a challenge, even nowadays. In addition to the development of new scintillators, much of the effort has focused on new fabrication techniques and detector configurations to enlarge the size and enhance detector performances. Fig. 1-3 shows the history of the important discoveries of inorganic scintillator materials in the last century.6,17,18)

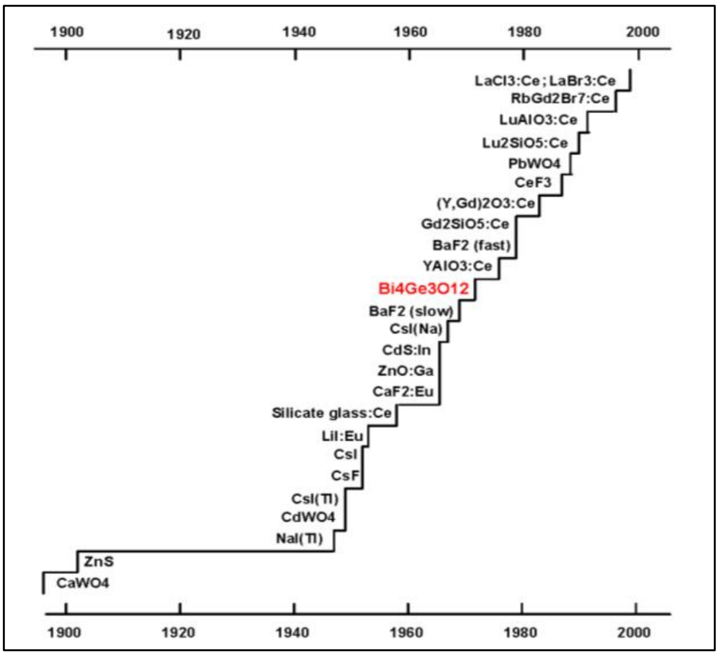

Fig. 1-3. Timeline for the discovery of important inorganic scintillators.6,17,18)

A scintillator is a scintillation material that changes high-energy particles, such as γ-ray or X-ray, into UV or visible photons that can be detected by PMT. Physical, optical, and chemical properties are usually used to assess scintillation materials.15,16) The common properties are listed in Table 1-4. None of the scintillator materials can solely address all requirements because different applications vary in the priorities. Oftentimes, a scintillation material is only selected after its comprehensive properties have been optimized to match the requirements of practical applications.

Table 1-4. The desired properties of an exceptional scintillator.[18-20)]

Criteria	Scintillation properties
Detection efficiency	High density and atomic number
Good spatial resolution	High light yield
Good energy resolution	Clear identification of energy event
High count rate capability	Short decay time; low afterglow
transmission for light to photodetector	Transparent at emission wavelength
Suitable emission spectra	matching with PMT or photodiode
Radiation hardness	Stable performance to ionizing radiation
Chemical, thermal and mechanical stability	Rugged and no hygroscopic;
Costive production	Low-cost raw materials; conventional growth technique

1.2 Development and properties of BGO scintillation crystal

1.2.1 Crystal structure of BGO scintillator

In 1957, Durif,[21)] the first scholar to synthesize BGO crystal through solid-state reaction, reported that BGO crystal had a bismuth-blended structure. Later, Fischer et al.[22)] confirmed the finding by means of X-ray diffraction.

BGO belongs to the $I\bar{4}3d$ space group symmetry and has four formula units in the unit cell. The atomic arrangement is characterized by its isolated tetrahedral $[GeO_4]^{4-}$ and distorted octahedral $[BiO_6]^{9-}$ (Fig. 1-5).

The unit cell of BGO contains 38 atoms (i.e., 6 Ge, 8 Bi, and 24 O) in (12a), (16c), and (48e) Wyckoff positions. Each Bi atom is surrounded by six O arranged in a strongly distorted octahedron: three of them are situated near Bi 2.1608 Å and the other three near 2.6038 Å. The Ge atoms are surrounded by four O, all at the same distance (i.e., 1.7396 Å) and arranged in the vertices of a perfect tetrahedron.[23)]

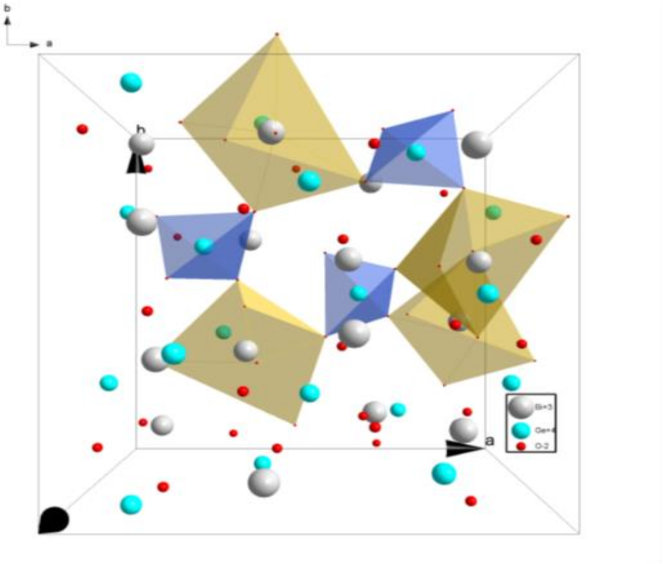

Fig. 1-5 BGO crystal structure.

The $[BiO_6]^{9-}$ octahedrons are strongly distorted from the regular octahedron symmetry to *C*3, and they have two types of Bi-O bond lengths and two distinct $[BiO_3]^{3-}$ triads with O-Bi-O bond angles of 84.7° and 114.1°, as shown in Fig. 1-6 (a). The $[GeO_4]^{4-}$ tetrahedrons have Ge-O bonds that are all equal in length but with two distinct values of O-Ge-O bond angles, resulting in a *D*2*d* local polyhedral symmetry,24) as shown in Fig. 1-6 (b).

Each O atom is shared between one $[GeO_4]^{4-}$ tetrahedron and two $[BiO_6]^{9-}$ octahedrons, i.e., the $[BiO_6]^{9-}$ octahedron are edge-shared to each other and corner-shared to the $[GeO4]^{4-}$ tetrahedron (Fig. 1-5).

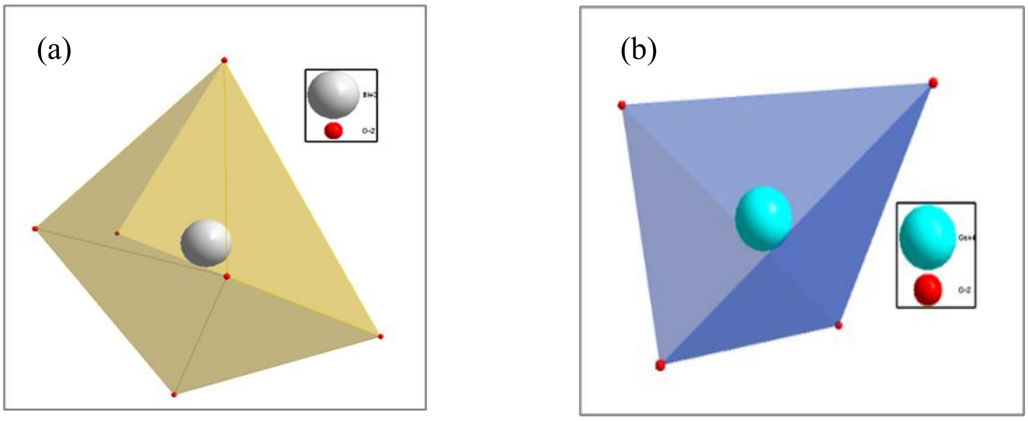

Fig. 1-6 (a) The $[BiO_6]^{9-}$ octahedron and (b) the $[GeO_4]^{4-}$ tetrahedron.

1.2.2 Growth methods of BGO crystals

Czochralski25) and Bridgman growth26,27) are the conventional methods to fabricate BGO single crystals. At present, the three major global providers of BGO crystals are Shanghai Institute of Ceramics, Chinese Academy of Sciences (SICCAS), Institute of Inorganic Chemistry of the Siberian Branch of the Russian Academy of Sciences (NIIC SB RAS) 28) and Saint-Gobain, France29), as presented in Table 1-5.

Table 1-5 Three major providers for BGO crystals in the world.28,29)

Providers	Growth method	Shape	Volatility	Efficiency
NIIC SB, Russia	Czochralski	Circular column	High	Single boule
Saint-Gobain, France	Czochralski	Circular column	High	Single boule
SICCAS, China	Bridgman	Variable shape	Low	22 boules

Among them, SICCAS adopts the vertical Bridgman growth of BGO crystals, whereas the two other providers use the Czochralski method for BGO growth. In contrast to the Czochralski method (Fig. 1-7),30) the Bridgman method has merits of customizable crystal shaping on the crucible, low volatility owing to the sealed Platinum (Pt) crucible, massive production, and cost-effectiveness.

The Bridgman technique (Fig. 1-8) is named after Percy Williams (P. W.) Bridgman, the first scientist who used this method to obtain many metal single crystals.31,32) The principle of this technique involves lowering a crucible through a furnace so that the solidification starts at the solid–melt interface with the largest temperature gradient in the zone of the baffle layer, and then the solid–melt interface slowly moves up along the crucible. The growth rates for these processes33,34) usually range from around 0.1 to 10.0 mm/h for different BGO crystals. A typical vertical Bridgman system is shown in Fig. 1-8.

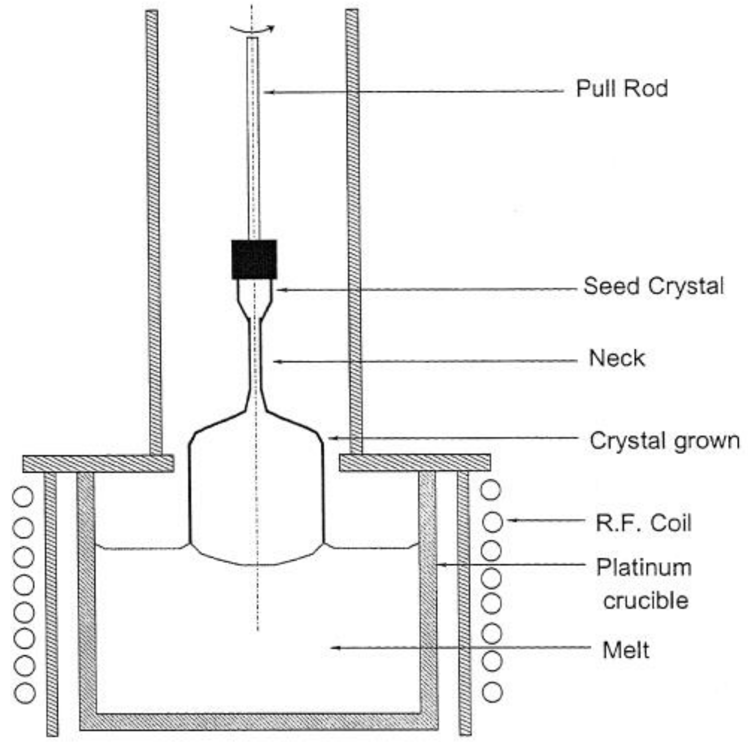

Fig. 1-7 Schematic diagram of Czochralski furnace.[30)]

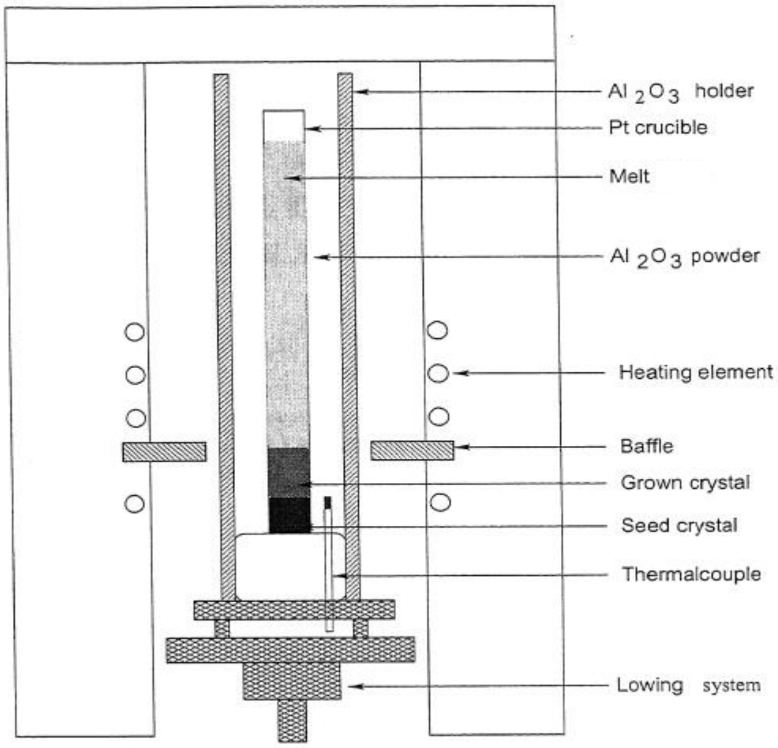

Fig. 1-8 Schematic diagram of vertical Bridgman furnace.[31)]

1.2.3 Luminescence mechanism of BGO scintillators

Table 1-6 presents some intrinsic scintillator materials and their radiative transitions. BGO is a self-activated intrinsic scintillator. The luminous center Bi^{3+} is evenly distributed on the lattice. The ground state electronic configuration of Bi^{3+} ions is $6s^2$ that forms the energy level $^1S_0$, while the excited state configuration $6s^16p^1$ forms the energy levels $^3P_0$, $^3P_1$, $^3P_2$, and $^1P_1$.1) The allowable transitions from the ground state to excited states are $^1S_0 \rightarrow {}^3P_1$ and $^1S_0 \rightarrow {}^1P_1$. The two luminescence peaks of BGO excitation spectrum at ~290 and ~250 nm can be attributed to $^1S_0 \rightarrow {}^3P_1$ and $^1S_0 \rightarrow {}^1P_1$ transitions, respectively.1) The $^3P_0$ state represents the lowest excited state of Bi^{3+}, but the $^3P_0 \rightarrow {}^1S_0$ transition is forbidden. However, if the energy difference between $^3P_0$ and $^3P_1$ is $\Delta E \backcong kT$, then $^3P_1$ will be largely filled by thermal excitation, suggesting a great probability of radiation decay. Bi^{3+} fluorescence is the radiation transition from $^3P_1 \rightarrow {}^1S_0$, and its central wavelength is near 480 nm.

Table 1-6. Selected intrinsic scintillator materials and their radiative transitions.1,34,35)

Category	Scintillation materials	Emission transition
Intrinsic (self-activated)	BGO	6p-6s
	CeF_3	5d-4f
	$CdWO_4$	charge transfer
	CsI, NaI, LaF_3	self-trapped exciton
	CsF, BaF_2	core-valence band

The detection of X-rays, γ-rays and charged particles involves the energy left by electrons generated by the incident irradiation. The BGO crystal is a good scintillator that can absorb ionizing radiation and convert the partial energy into visible or UV light, which are detectable by a photodiode or PMT.36,37) The schematic diagram of a BGO scintillator detector is shown in Fig. 1-9.

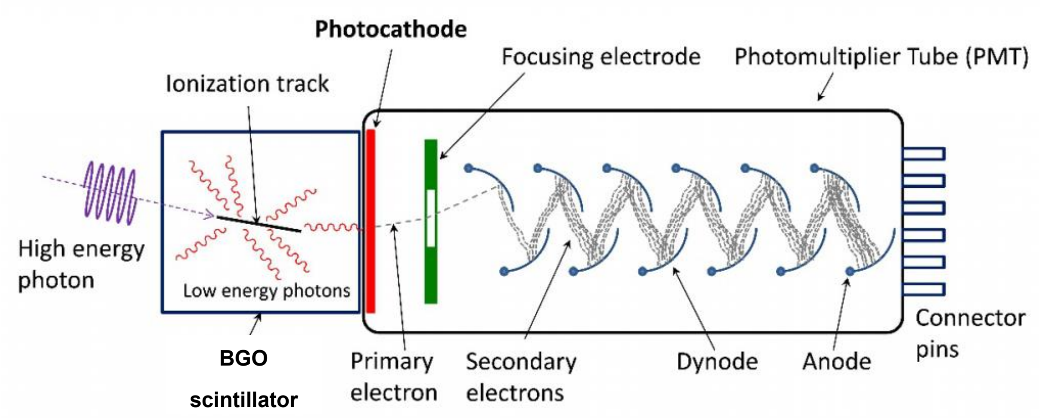

Fig. 1-9. Schematic diagram of BGO scintillator detector.37)

1.2.4 Development and application of BGO scintillators

Durif21) was the first researcher to synthesize BGO polycrystals via the solid-state reaction in 1957, while Nitsehe38) was the first one to prepare the single crystal BGO in 1965. Johnson et al.39) prepared the BGO:Nd single crystal in 1969. In 1973, Weber and Monchamp1) were the first scholars to propose BGO for use as high-energy X-ray and γ-ray detection scintillators. The details are shown in Table 1-7.

Table 1-7 Physical properties of common scintillation crystals.40-46)

Crystal	Density(g/cm^3)	Effective atomic	Hygroscopic	Rugged
$CdWO_4$	7.9	64	No	No(cleaves)
Lu_2SiO_5:Ce	7.4	65	No	Yes
$Bi_4Ge_3O_{12}$	7.13	75	No	Yes
Gd_2SiO_5 :Ce	6.71	59	No	No(cleaves)
BaF_2	4.88	53	No	Yes
CsF	4.64	53	High	No
CsI:Na	4.51	54	Yes	Yes
CsI:Tl	4.51	54	Slightly	Yes
NaI:Tl	3.67	51	Yes	No
CaF_2:Eu	3.18	17	No	No

Nestor and Huang47) studied the main scintillation characteristics of BGO. In contrast to the conventional NaI:Tl, BGO has the characteristics of high density, high γ-ray absorption coefficient, good mechanical properties, chemical stability, intrinsic luminescence, and absence of hygroscopic behavior.

The aforementioned advantages enable BGO crystal to be widely used in nuclear medical imaging,48,49) high-energy physical electromagnetic calorimeter,50) complex detectors for astrophysics,51) scanners52) and geological exploration.53)

Compared with common scintillators, BGO crystals have a higher effective atomic number, higher density, and lower self-absorption.54) The high atomic number of BGO crystals enable them to achieve a high probability of photoelectric effect, further suggesting a high probability of being fully absorbed by the annihilation γ-ray at the first interaction site; this scenario lessens the probability of light scattering within the BGO crystals. In addition, the intrinsic background of BGO crystals is low at around 7 cps/ml. The main properties of BGO crystals are presented in Table 1-8.

Table 1-8 The main properties of BGO crystal.53,54)

Item	**Parameter**	**Item**	**Parameter**
Structural formula	$Bi_4Ge_3O_{12}$	Color	None
Crystal system	cubic	Effective atomic number	74
Space group	T_d^6-I43d	Dielectric constant	16
Cell size (nm）	a=1.052	Refractive index (486.1nm / 632.8 nm)	2.149/2.098
Density (g/cm^3)	7.13	Electro-optic index (K41, cm/V)	1.03×10^{-10}
Melting point/°C	1050	Thermal expansion coefficients (℃/cm/cm)	7.15×10^{-6}
Decay time (ns)	300	Light output (photons/MeV)	9000
Hardness (Mohs)	5	Nonlinear optical coefficients (λ=1.0642 μm)	$d_{14}= 1.46 \times 10^{12} d_{il}^2 m/V$ $d_{14}= 0.47 \times 10^{2} \delta_{il}^2 m/V$

BGO crystal exhibits good scintillation properties[56,57], such as good ER, high effective atomic number, relatively short decay time, high density, high LO, low afterglow, well radiation hardness, ruggedness, and good sensitivity to a variety of particles.[58] Table 1-9 presents several desired properties of BGO scintillator crystals in medical imaging systems, particularly for positron emission tomography (PET).[59]

Table 1-9 Several desired scintillation properties for PET.[55,56,59]

Crystal Property	**Purpose**
High Density	High gamma ray detection efficiency
High atomic number	High gamma ray detection efficiency
Short decay time	Good coincidence timing
High light output	Allows large number of crystal elements per photodetector
Good energy resolution	Clear identification of full energy events
Emission wavelength near 400 nm	Good match to photomultiplier tube response
Transparent at emission	Allows light to travel unimpeded to photomultiplier
Index of refraction near 1.5	Good transmission of light from crystal to photomultiplier tube
Radiation hardness	Stable crystal performance
Nonhygroscopic	Simplifies packing
Rugged	Allows fabrication of smaller crystal elements
Economic growth process	Reasonable cost

PET, the medical imaging metord is used to assess metabolism. For example, by injecting two 511 keV quanta to a beam in a quanta-collinear manner, the positron can be annihilated, consequently addressing certain particular tissue. By coincidence counting using position-sensitive detectors, the two quanta are detected. As shown in Fig. 1-10, a PET system consists of many rings with thousands of scintillation detectors in general. The most commonly used scintillator is BGO because of its high density, high atomic number, and large probability of photoelectric effect (511 keV quanta).[60]

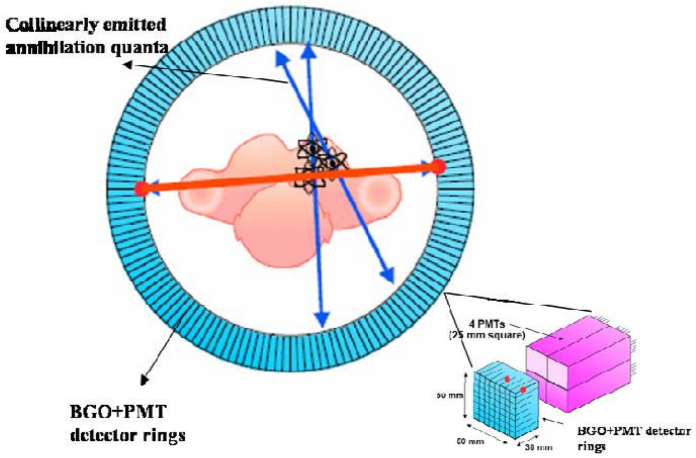

Fig. 1-10. Schematic diagram of PET with the inset illustrating BGO detectors coupled with PMT.$^{60)}$

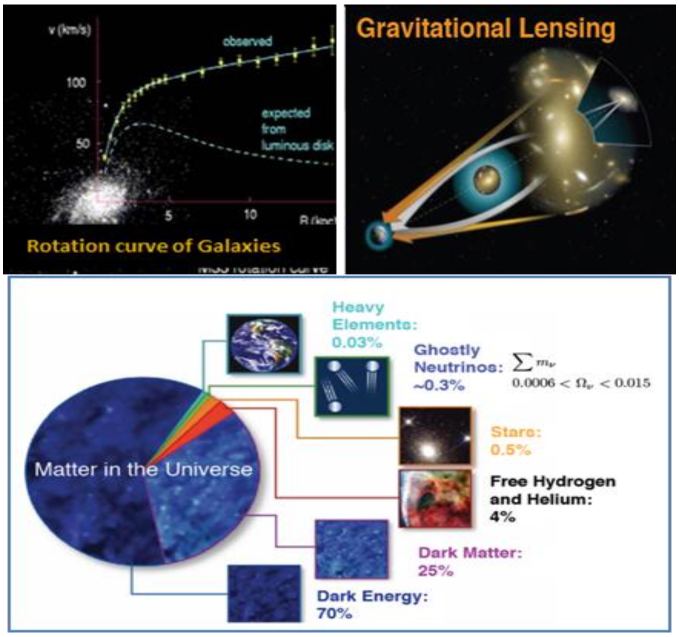

Fig. 1-11 Dark matter in the universe.$^{62)}$

The BGO crystals with large-size, high-quality, and good properties are prepared in large quantities in SICCAS that is famous in the world. Since 1998, BGO crystals grown by SICCAS have been applied in General Electric Company (GE) healthcare, accounting for more than 85% of the world market.$^{61)}$

Another important application of BGO crystals is in the DArk Matter Particles Explorer (DAMPE) of spaces sciences. Reportedly, 95% of matter in the universe is 25% dark matter and 70% dark energy. Searching for dark matter in the universe is an

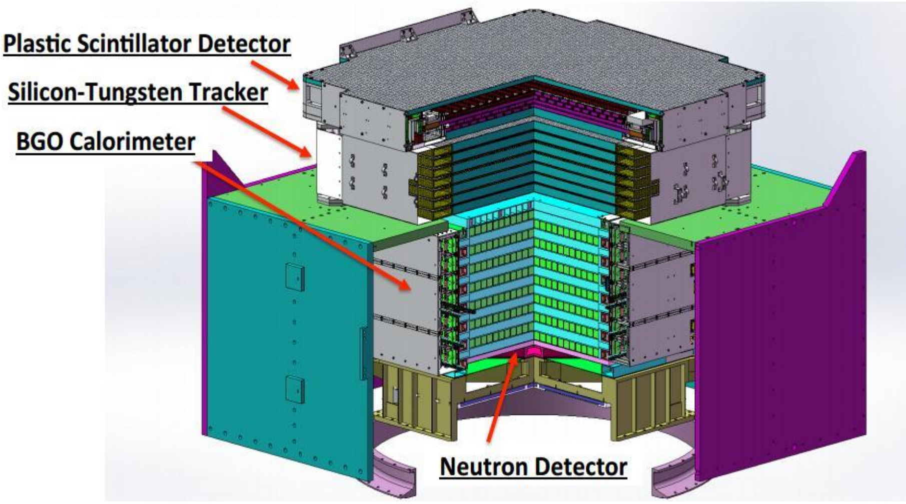

Fig. 1-12 Payload structure of DArk Matter Exploration satellite.[69)]

important and challenging task in the world.[62-64)] In 2015, China launched DAMPE,[65-69)] the first space dark matter detection satellite, to find evidence for the existence of dark matter particles in space (Fig. 1-11).

A key part of DAMPE is the BGO calorimeter, which is called the “golden eye” of the satellite. The BGO calorimeter is used to observe dark matter from possibly annihilation products (high-energy electrons and γ-rays).[67)] The BGO calorimeter is composed of a stack of 25 mm × 25 mm × 600 mm BGO scintillation crystals (Fig.1-12).[69)]

These 600 mm-long crystals should have high optical quality, high ER, and good LRU. The LRU represents the dependence in the PMT collection of scintillation light along the long axis of the crystal. The LRU of the 600 mm-long BGO crystal is the most important measure of the calorimeter properties.

In conventional techniques, such as Czochralski[30)] or Bridgman[70-72)] techniques, large-size BGO crystals is difficult to achieve. The fluctuation of temperature profiles at the solid–melt interface and the component’s undercooling or segregation during the growth process easily lead to the creation of scattering particles, impurity cores and point defects within the BGO crystals. The existence of these defects will seriously and negatively affect the optical transmission, scintillation properties, and LRU of the BGO. For large-size and high-quality BGO crystals, the challenge is not only to achieve the

600 mm-long crystals but also to optimize their scintillation properties. The motivation of this thesis is to determine the suitable conditions for obtaining high-quality and large-size BGO crystals and optimize their performances, such as transmittance, LRU, and ER by comprehensively understanding the reasons behind the various defects and knowing how to reduce them.

1.3 Thesis objectives and organization

1.3.1 Research objectives

This thesis entails three objectives. The first objective is to prepare large-size BGO crystals via the modified vertical Bridgman (MVB) method to meet the requirements of the large-size electromagnetic calorimeter in DAMPE. First, we investigate the process of fabricating high-quality BGO crystals with good properties, especially the optimization process via the MVB technique. The crystal growth mechanism is also investigated in terms of the kinetics on thermal transportation, the shape of the solid–melt interface, the mass transportation from melt to crystal, and the reaction of $[GeO_4]^{4-}$ and $[BiO_6]^{9-}$ growth units to attain high-quality full-size BGO crystals.

The second objective of this thesis is to investigate the mechanism of BGO crystals affected by various defects and determine how to eliminate them, thus improving the quality and performance of full-size BGO crystals. BGO crystals often exhibit reddish color, a microdefect exhibiting visible absorption bands, especially from 310 to 390 nm, during crystal growth when growth parameters fluctuate. The reddish color inevitably results in the deterioration of scintillation properties, including optical transmission, LO, ER, and LRU. In this thesis, after comprehensively explaining the formation mechanism of various defects in the as-grown BGO crystals, a corresponding technique is established to eliminate the reddish color.

The third objective of this thesis focuses on the characterization of optical transmittance and ER of BGO crystals to identify the regulation of as-grown full-size BGO crystals. The statistical distribution of the LRU of the 600 mm-long BGO crystals is investigated in detail to better understand structure-property relationship, and find the way to improve performance of BGO crystals, especially since DAMPE needs hundreds of 600 mm-long BGO crystals with high optical quality and LRU.

1.3.2 Thesis organization

This thesis consists of seven chapters. Chapter 1 introduces the development and application of inorganic scintillation crystals. It includes the fundamentals of radiation detectors and a background of some material properties of BGO crystals.

Chapter 2 presents the experimental methods for characterizing the properties of the BGO crystals.

In Chapter 3, the crystal growth of hundreds of high-quality large-size BGO crystals via the MVB method is discussed. The formation reasons of various defects were analyzed by the kinetics on thermal transportation and the shape of the solid–melt interface. The effect of the various defects is further investigated in terms of optical transmittance of BGO crystals.

In Chapter 4, the defects and their vital role are verified by means of a series of experimental techniques. The mechanism of how to remove the oxygen vacancy ($V_o^{\bullet\bullet}$) and bismuth vacancy (V_{Bi}''') in the BGO lattice is discussed.

In Chapter 5, an effect of annealing in different atmospheres on the optical transmittance and scintillation properties for the reddish BGO crystal is reported. An effective annealing technique to eliminate the reddish is established for the reddish BGO crystal. The origin of the reddish in BGO crystal and the essence of annealing are investigated.

In Chapter 6, the optical transmittance and scintillation properties for 600 mm-long BGO crystals are characterized by building a now test platform and adopting the corresponding methods. For a few initial unsatisfied crystals, the post-treatment, such as air annealing, reflective materials, and surface treatment, is investigated. Then the best scintillation properties of 600 mm-long BGO crystals are reported.

Finally, in Chapter 7, the conclusions of this thesis are summarized, and relevant future studies are considered.

References

1) M. J. Weber, J. Lumin., **100**, 35 (2002).
2) M. Ishii, and M. Kobayashi, Prog. Cryst. Growth Charact. Mater. **23** ,245 (1992).
3) C. Greskovich, and S. Duclos, Annu. Rev. Mater. Sci., **27**, 69 (1997).
4) P. A. Rodnyi, Physical processes in inorganic scintillators. CRC press, New York, 1997.
5) S.K. Sahi, Synthesis and characterization of nanocomposite scintillators for radiation detection[D], The University of Texas at Arlington, 2016.
6) P. Lecoq, Inorganic scintillators for detector systems physical principles and crystal engineering. Springer-Verlag Berlin and Heidelberg, 2006.
7) G. Bizarri, J Cryst. Growth, **312**, 1213 (2010).
8) C.W.E. vanEijk, Nucl. Instrum. Meth. A, **460**, 1 (2001).
9) E. Hell, W. Knfer, and D. Mattern, Nucl. Instrum. Meth. A, **454**, 40 (2000).
10) G.F. Knoll, Radiation detection and measurement. New York: Wiley, 2000.
11) S.N. Ahmed, Physics and engineering of radiation detection. Academic Press, 2007.
12) B. Adeva, et al., Nucl. Instrum. Meth. A, **289**, 35 (1990).
13) D. Graham, and C. Seez, CMS Note, (1996) 96/002.
14) C. L. Melcher, J. Nucl. Med., **41**, 1051(2000).
15) C. W. E. van Eijk, Radiat. Prot. Dosim., **129**, 13 (2008).
16) S. E. Derenzo, W. W. Moses, J. L. Cahoon, R. C. C. Perera, and J. E. Litton, IEEE Trans. Nucl. Sci., **37**, 203 (1990).
17) E. Browne, and H. Junde, Nucl. Data Sheets, **84**,337 (1998).
18) C.C. Watson, M.E. Casey, L. Eriksson, T. Mulnix, D. Adams, and B. Bendriem, J. Nucl. Med.**, 45**, 822 (2004).
19) S. Yamamoto, H. Horii, M. Hurutani, K. Matsumoto, and M. Senda, Anal. Nucl. Med., **19**,109 (2005).
20) A.L. Goertzen, J.Y. Suk, and C.J. Thompson, J. Nucl. Med., **48**, 1692 (2007).
21) A. Durif, Crystallographic Data. 170., Anal Chem., **30**, 1161 (1958).
22) P. Fischer, and F. Waldner, Solid State Comm., **44**, 657 (1982).

23) G.M. Kuz’micheva, I.A. Kaurova, L.I. Ivleva, E.V. Khramov, P.A. Eistrikh-Geller, V.B. Rybakov, T.V. Chukhlovina, and S.V. Firstov, Arab. J. Chem. **11**, 1270 (2018).

24) T.I. Mel’nikova, G.M. Kuz’micheva, and N.B. Bolotina, Crystallogr. Rep. **59**, 353 (2014).

25) R. Nitsche, J. Appl. Phys., **36**, 2358 (1965).

26) S. Fan, et al, Princeton University, Department of Physics, 103 (1982).

27) S. Fan, G.S. Shen, J.L. Li, and W. Wang, Cryst. Properties and Preparation, **36**, 38 (1991).

28) http://niic.nsc.ru/institute/881-niic/3729-bgo-crystal.

29) https://www.saint-gobain.com/en.

30) R. Mao, A Study on Mass produced Lead Tungstate crystal and improvement of light output[D], Shanghai Institute of Ceramics, Chinese Academy of Science, 2003 (in Chinese).

31) Y. Huang, Luminscence properties and doping effects in Lead Tungstate single crystals[D], Shanghai Institute of Ceramics, Chinese Academy of Science, 2003 (in Chinese).

32) P.W. Bridgman, Proc. Am. Aca. Arts Sci., **60**, 305 (1925).

33) F.M. Carlson, A.L. Fripp, and R.K. Crouch, J. Cryst. Growth, **68** (1984) 747-756.

34) P.C. Sukanek, J. Cryst. Growth. **58**, 208 (1982).

35) P.A. Williams, and A.H. Rose, et al, Appl. Opt., **35**, 3562 (1996).

36) C. Greskovich, and S. Duclos, Annu. Rev. Mater. Sci., **27**, 69 (1997).

37) H. Kume, K. Okano, and P. Hamamatsu, Photomultiplier tube: principle to application: photon is our business. Hamamatsu Photonics. 1994.

38) R. Nitsche, J Appl Phys., **36**, 2358 (1965).

39) T.F. Johnson, and A.A. Ballman, J Appl Phys., **40**, 297 (1969).

40) S.E. Derenzo, et al., Nucl. Instrum. Meth. A, **505**,111 (2003).

41) C.W.E. van Eijk, Nucl. Instrum. Meth. A, **392**, 285 (1997).

42) R. Novotny, Nucl. Instrum. Meth. A, **537**, 1 (2005).

43) W.W. Moses, et al., J. Lumin., **59**, 89 (1994).

44) C.W.E. van Eijk., J. Lumin., **60**, 936 (1994).

45) Y. Huijun, et al., J. Lumin., **31**, 833 (1984).

46) K.S. Shah, et al., IEEE Trans. Nucl. Sci., **50**, 2410 (2003).

47) O.H. Nestor, and C.Y. Huang, IEEE Trans. Nucl. Sci., **22**, 68 (1975).

48) Z.H. Cho, and M. Farukhi, J. Nucl. Med., **18**, 840 (1977).

49) S.E. Derenzo, IEEE Trans. Nucl. Sci., **28**, 131 (1981).

50) Y.K. Akimov, Phys. Part. Nucl., **25**, 92 (1994).

51) E. Costa, E. Massaro, and L. Piro, Nucl. Instrum. Meth. A, **243**, 572 (1986).

52) A.C. Rester, G.J. Bamford, and R.L. Coldwell, Nucl. Instrum. Meth. A, **297**, 258 (1990).

53) J. Liao, C. Ye, and P. Yang, Chemical Research, **15**, 52 (2004) (in Chinese).

54) A. Yoshikawa, and M. Nikl, Shaped Crystals, **143** (2007).

55) C.W.E. van Eijk, Nucl. Instrum. Meth. A, **460**, 1 (2001).

56) S. Polosan, E. Apostol, M. Secu, and A. Gh, Phys. Status Solidi, **2**, 93 (2005).

57) D. A. Poster, and K. E. Easterling, IEEE Trans. Nucl. Sci., **54**, 1459 (2007).

58) Y.K. Akimov, Phys. Part. Nucl., **25**, 92 (1994).

59) V. Sank, R. Brooks, W. Friauf, W. Yee, and G. Dichiro, J. Nucl. Med., 23, 95 (1982).

60) T.K. Tseng, Luminescent oxide nanocomposite: synthesis, characterization and scintillation application[D], the University of Florida (2010)

61) Y. Zhang, and S. Wang, Scientific Chinese, **66**, (2006) (in Chinese).

62) J.P. Ostriker, P. Steinhardt, Science, **300**, 1909 (2003).

63) J. Chang, Journal of Engineering Studies, **2**, 95 (2010).

64) A.A. Abdo, M. Ackermann, and M. Ajello, Phys. Rev. Lett., **102**, 181101 (2009).

65) O. Adriani, G.C. Barbarino, and G.A. Bazilevskaya, Nature, **458**, 607 (2009).

66) J. Chang, J.H. Adams, H.S. Ahn, G.L. Bashindzhagyan, M. Christl, O. Ganel, T.G. Guzik, J. Isbert, K.C. Kim, E.N. Kuznetsov, M.I. Panasyuk, A.D. Panov, W.K. Schmidt, E.S. Seo, N.V. Sokolskaya, J.W. Watts, J.P. Wefel, J. Wu, and V.I. Zatsepin, Nature, **456**, 362 (2008).

67) J. Chang, and J. Wu, High energy electron and gamma-ray observation by

TANSUO mission, Proceedings of the 31st ICRC [C], **1** (2009).

68) J. Chang, DArk Matter Particle Explorer (DAMPE)[R], (2012).

69) Z. Ji, A Study on Light Response Uniformity of 600mm Long BGO Crystals for Dark Matter Detection in Space[M], Shanghai Institute of Ceramics, Chinese Academy of Science, 2013 (in Chinese).

70) V. Sank, R. Brooks, W. Friauf, W. Yee, and G. Dichiro, J. Nucl. Med., **23** (1982) 95.

71) M. Ishii, K. Harada, N. Senguttuvan, M. Kobayashi, and I. Yamaga, J. Cryst. Growth, **205**, 191 (1999).

72) H. V. Piltingsrud, J. Nucl. Med., **20**, 1279 (1979).

Chapter 2 Experimental Methods

2.1 Structure characterization

2.1.1 X-ray diffraction

The lattice structure and phase purity within BGO crystal are investigated by an X-ray diffraction (XRD) pattern of powder samples.[1-4] The technique is based on the incidence of beam of X-ray beam to BGO crystal, and the collection of the diffracted X-ray beam. In this thesis, the XRD pattern was measured by high resolution powder X-ray diffractometer using CuKα radiation (Bruker, D8 ADVANCE) to verify the composition of yellow powder deposited on the chamber exit of the furnace during annealing experiments in vacuum and nitrogen atmosphere. The power of the X-ray generator was set to 40 kV and 150 mA. The energy resolution of the energy dispersive array detector is better than 380 eV. The 2θ angle is scanned from 10° to 80°.

2.1.2 Raman spectroscopy

Raman spectroscopy probes the photon energy originated from the vibration and rotation modes [5,6] in BGO crystal sample. In this thesis, Raman spectra of the BGO samples at different temperatures (25, 200, 400, 600, 800, 1050 and 1100 °C) were performed by Renishaw Raman microscopy with 532 nm wavelength laser, 2 mW power, 1 s exposure time, and 50× objective lens.

2.2 Defects characterization

2.2.1 X-ray photoelectron spectroscopy

X-ray photoelectron spectroscopy (XPS) is performed to determine the surface composition in terms of elements and oxidation states of the BGO crystal samples.

In the thesis, XPS was obtained with a Thermo Fisher ESCALAB 250 X-ray spectrometer. The chamber pressure was kept below 2 x 10^{-10} mbar during measurement. The instrument ER was below 0.45 eV and the spatial resolution was less 20 μm. The composition of bismuth and oxygen were estimated by comparing the photoelectron peak intensities of the Bi 4f with the O 1s core level peaks.

2.2.2 Electron paramagnetic resonance

Electron paramagnetic resonance (EPR) is sensitive to the unpaired spins of electron/holes captured at such color centers in crystal. In this thesis, EPR spectrum was carried out using a Bruker A300 spectrometer with gradual heating from 25 to 1050 ℃ to identify the information of paramagnetic substances within BGO crystals by identifying spins and their interaction with the surroundings. The microwave X-band frequency is fixed at 9.85 GHz with 100 kHz modulation and phase-sensitive detection to obtain the first derivative signal. The reddish BGO samples at different temperatures (range of 25 to 1050 ℃) and the reddish BGO crystals after N_2, and O_2 annealing were performed.

2.2.3 Thermoluminescence

Another method to investigate the luminescence of BGO crystals is thermoluminescence (TL)-thermally stimulated emission of light after exposure to ionizing radiation.[7,8] The TL measurements were performed using a ROSB TL 3DS TL spectrometer after X-ray irradiating with a heating rate of 0.5 K/s from 50 to 250 °C. For TL measurements, small size BGO samples were cut from the large-size as-grown crystal due to space limitations of the instruments sample holder. TL curves of the reddish BGO crystal before and after oxygen annealing are obtained to analysis the traps change of defects.

2.2.4 Transmission electron microscopy-energy dispersive spectroscopy

Transmission electron microscope (TEM) is a conventional technique for imaging scintillation crystals to obtain quantitative information of BGO crystals. TEM could get the micrograph from the transmission of a focused electron beam in an ultrathin reddish BGO crystal, producing a magnified image.9)

In this thesis, TEM (FEI Tecnai G2 F20, USA) and AC-STEM (Hitachi HF5000, Japan) were used with dual energy dispersive spectroscopy (EDS) (Oxford X-Max, UK). FEI TEM has a high voltage (200 kV) and a point resolution (0.24 nm). Hitachi HF 5000 is an ultrahigh resolution TEM with an accelerated high voltage of 200 kV and a point-to-point resolution of 0.23 nm. BGO samples were ground manually to a thickness of ~50 μm by using SiC slurry and further polished via 5 kV Ar ion milling with 8 ° non-modulations (PIPS II 695, Gatan, USA).

High-resolution transmission electron microscopy (HRTEM) was performed by a JEM-2100F field emission transmission electron microscope. This is an ultrahigh resolution TEM with a resolution of 0.19 nm. HRTEM micrograph offered a more complete view of the microstructures of the reddish BGO crystal.

2.3 Scintillation property characterization

2.3.1 Photoluminescence spectroscopy

The luminescence of corresponds the emission of light from the state of excitation energy returned to the ground state.10) Due to the specific molecular structure in different materials, the distribution of excited state energy levels has unique characteristics. This characteristic of energy state can be reflected in the fluorescence. The characteristic emission peak of BGO crystal is around 480 nm. BGO crystal samples are stimulated in an excitation light source, usually a xenon lamp. The light with specific wavelengths is generated by a filter of excitation monochromator. The emitted photons are commonly collected and analyzed by the monochromator connected by a PMT detector.11,12)

In this work, PL measurements were performed by using a spectrofluorometer (an Edinburgh FLS920) equipped with a 450 W xenon lamp and double light monochromators for both excitation and emission (Fig. 2-1). The excitation wavelength is constant in emission spectra, and the emitted light is measured at different wavelengths from 300 to 700 nm.

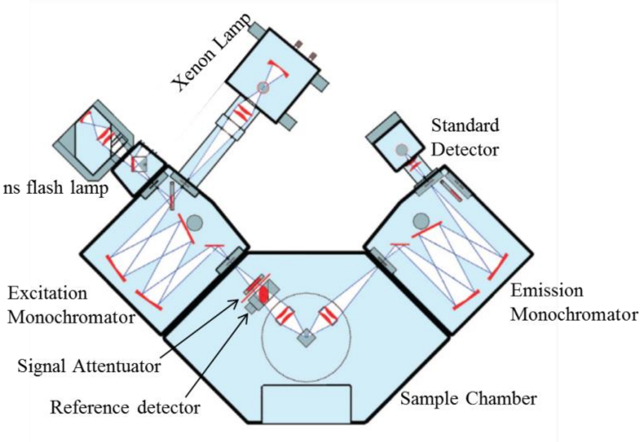

Fig. 2-1 Structure schematic of FLS920 fluorescence spectrometer.$^{12)}$

2.3.2 Optical transmittance

The properties of BGO crystals depend partially on their transparency. A double beam UV/visible spectrophotometer was used in this thesis. It allowed investigation of BGO crystals transparency in UV and visible range as a function of wavelength.$^{13-15)}$

The measurements of optical transmittance are taken using a Perkin Elmer Lambda 950 UV/visible/near infrared spectrophotometer equipped with dual beam, dual monochromator, large sample room and integrating sphere detector lined with Spectralon (Fig. 2-2). For all measurements, the reference sample holder is empty. Spectra are taken from 300 to 700 nm with a spectral resolution (1 nm), and a slit width (2 nm). The compared crystals were approximately the same thickness, therefore, the results were not corrected by the BGO sample thickness.

The optical transmission spectra of the BGO crystals and the reflectivity of the reflector materials were measured by a Perkin Elmer Lambda 950 spectrophotometer equipped with a general purpose optical bench (GPOB) with a Spectralon-coated integrating sphere and beam apertures. It was less than 0.2% in the systematic uncertainty for repeated measurements.$^{16)}$

The measurement setup of optical transmittance was home-made and the light path was designed for 600 mm-long BGO crystals (Fig. 2-3).

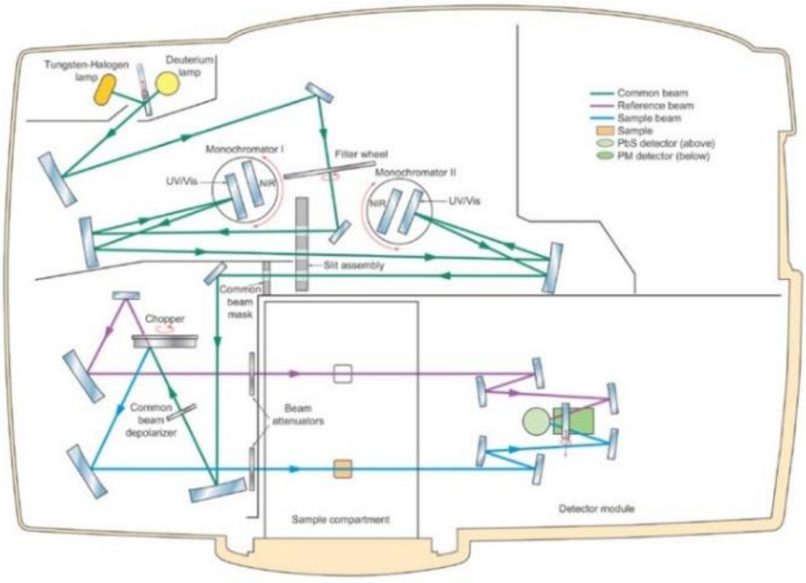

Fig. 2-2 Schematic setup of PE Lamda950 spectrophotometer.12)

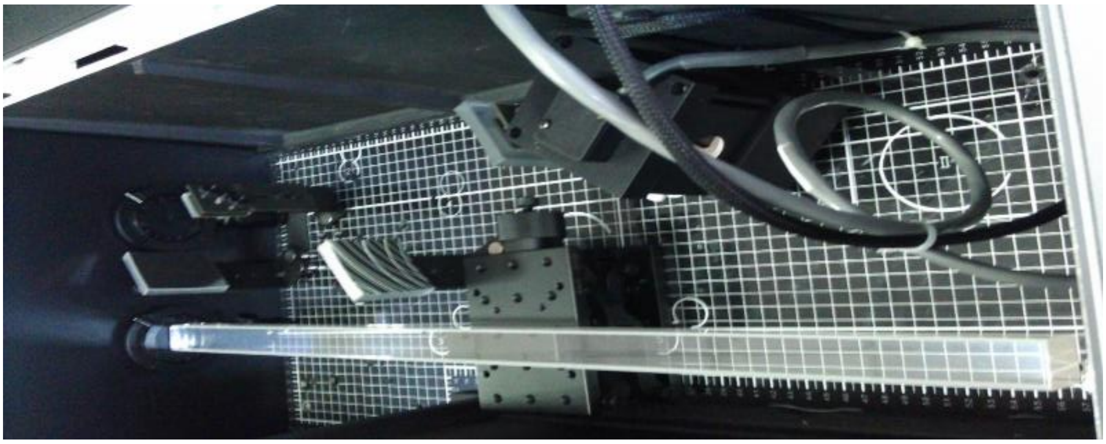

Fig. 2-3 Measurement system of optical transmittance for 600 mm-long BGO crystals.

2.3.3 Light out and energy resolution

The LO and ER of BGO crystals were measured by the multichannel analysis system of EG & G ORTEC. The dual-end readout mode was tested using two Hamamatsu PMTs with a borosilicate glass window and by irradiating the crystal with a collimated ^{137}Cs γ-rays source (2 μCi) at eleven positions evenly distributed along the crystal's longitudinal axis (means the direction of the longer optical path, Fig. 2-4 (a)).16) All other surfaces of the samples were wrapped with the reflective materials.

In this thesis, the scintillation response was measured by using Hamamatsu PMT detectors. By Hamamatsu preamplifier ORTEC 113 and shaped with a spectroscopy ORTEC amplifier Model 671, PMT output was further amplified. Multi-channel analyzer was an EG&G ORTEC 4001C MCA. The schematic diagram of the pulse processing chain is presented in Fig. 2-4 (b).

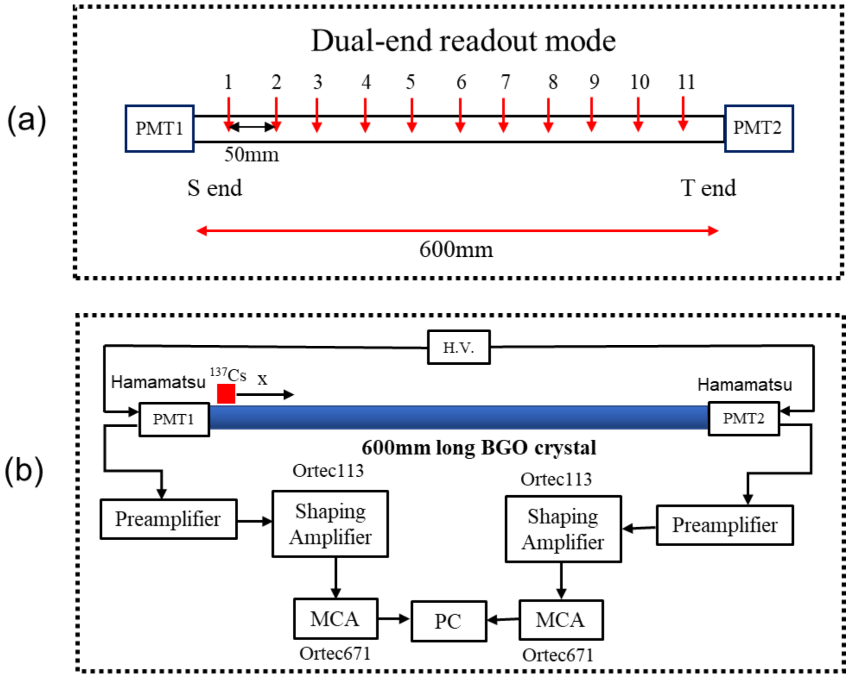

Fig. 2-4 Schematic diagrams of dual-end readout mode (a) test principle of the LRU and (b) pulse processing chain for the LO acquisition.16)

2.3.4 Light response uniformity

The LRU of BGO crystals was performed using two Hamamatsu PMTs operated at -900V and 2 μs shaping time in a dark box (Fig. 2-5), together with the power supply, control, and data acquisition electronics. The setup involves mounting a radioactive source above BGO crystal and coupling the BGO crystal to a PMT with optical grease. The full energy peak was determined by a single Gaussian fit. The pulse heights at these eleven positions along the crystal were fit to a normalized function,16-18)

$$\frac{\mathrm{LO}}{\mathrm{LO}_{av}} = 1 + \delta\left(\frac{x}{x_{\mathrm{mid}}} - 1\right) \quad (2\text{-}1)$$

where $\mathrm{LO}_{\mathrm{av}}$ represents the average LO of the sample, x is the distance from the end coupled to readout device and $\delta_{(\mathrm{S\ or\ T})}$ represents the deviation of the LRU. The schematic illustration of the δ is shown in Fig. 2-6. The measurement errors were estimated by repeatedly measuring the LRU of the long crystal. The δ_S and δ_T mean the results derived from the seed end and tail end of the crystal coupled with the PMT, respectively.[16)]

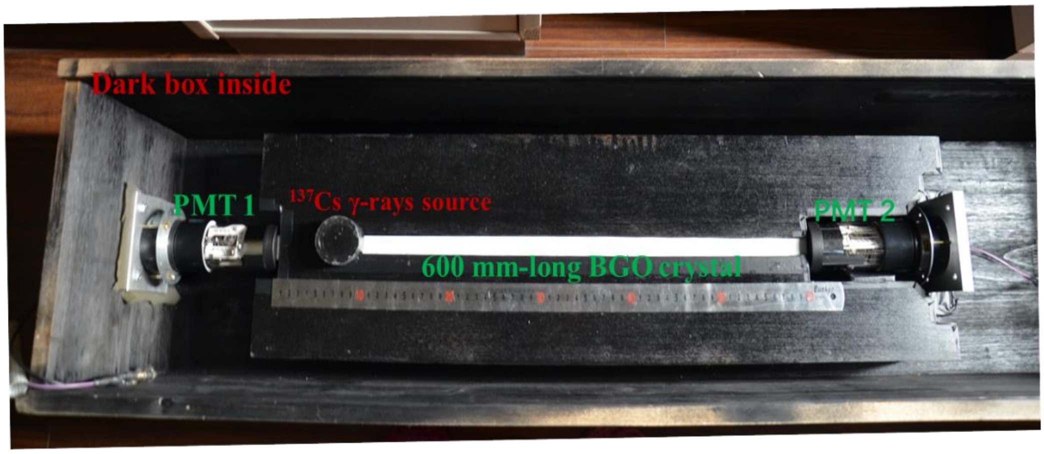

Fig. 2-5 Setup of multichannel analysis system in dark box inside.

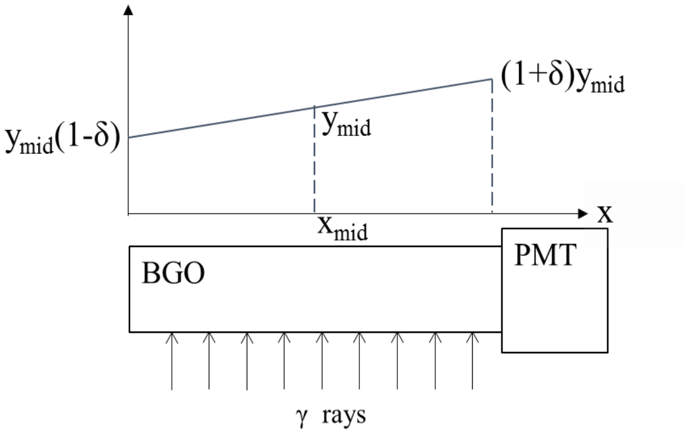

Fig. 2-6 Schematic illustration of the LRU.[18,19)]

References

1) B.D. Cullity, Elements of X-ray diffraction, Reading, Mass: Addison-Wesley Pub. Co., 1956.
2) Y. Leng, Materials Characterization: Introduction to Microscopic and Spectroscopic Methods, Wiley-VCH, Germany, 2013.
3) Z. Guo, and L. Tan, Fundamentals and applications of nanomaterials. Artech House, (2009)152.
4) R. Jenkins, R.L. Snyder, Introduction to X-Ray Powder Diffractometry, John Wiley & Sons, Inc., New York, 1996.
5) G. Gouadec, P. Colomban, Prog Cryst Growth Ch, 53 (2007) 1-56.65
6) N.B. Colthup, L.H. Daly, S.E. Wiberley, Introduction to infrared and Raman spectroscopy, 3rd ed., Academic Press, San Diego, 1990.
7) T. Artem, Microstructure, Luminescence, and Performance of Garnet Polycrystalline Ceramic Scintillators[D], Clemson University, 2018.
8) R. Chen, S.W.S. McKeever, Theory of Thermoluminescence and Related Phenomena, World Scientific, Singapore, 1997.
9) C.W. Oatley, The Scanning electron microscope. London: Cambridge University Press, 1972.
10) J. Solé, L. Bausa, D. Jaque, An Introduction to the Optical Spectroscopy of Inorganic Solids, John Wiley & Sons, Ltd, 2005.
11) R.J.D. Tilley, Luminescence, in: Colour and the Optical Properties of Materials, John Wiley & Sons, 2011.
12) Z. Ji, A Study on Light Response Uniformity of 600mm Long BGO Crystals for Dark Matter Detection in Space[M], Shanghai Institute of Ceramics, Chinese Academy of Science, 2013 (in Chinese).
13) G.F. Knoll, Radiation Detection and Measurement, 4th ed., John Wiley & Sons, Inc, Michigan, 2010.
14) Kumar, C.S.S.R. UV/Vis and photoluminescence spectroscopy for nanomaterials characterization. Springer Berlin, Heidelberg, 2013.

15) H.H. Perkampus, UV/Vis spectroscopy and its applications. Berlin, New York: Springer-Verlag, 1992.
16) L. Yuan, H. Ni, Z. Ji, J. Chen, G. Song, X. Qi, X. Li, S. Sun, and S. Wang, IEEE Trans. Nucl. Sci. **65**, 1403 (2018).
17) Z. Ji, H. Ni, L. Yuan, J. Chen, and S. Wang, Nucl. Instrum. Methods Phys. Res. Sect. Accel. Spectrometers Detect. Assoc. Equip. **753**, 143 (2014).
18) R. Zhu, Nucl. Instrum. Meth. **340**, 442 (1994).
19) J. Chen, L. Zhang, and R. Zhu, IEEE Trans. Nucl. Sci. **59**, 2224 (2012）.

Chapter 3 Crystal Growth and Characterizations

3.1 Crystal Growth

3.1.1 Phase diagram of Bi_2O_3-GeO_2 system

The phase diagram of the binary oxide (Bi_2O_3-GeO_2) system in Fig. 3-1 shows four compounds, namely, $Bi_2Ge_3O_9$, $Bi_4Ge_3O_{12}$, Bi_2GeO_5, and Bi_2GeO_{20}. Bi_2GeO_5 is an orthogonal crystal comprising a 1:1 molecule ratio of GeO_2 to Bi_2O_3. $Bi_2Ge_3O_9$ comprises is an excellent acousto-optic material comprising a 3:1 molecule ratio of GeO_2 to Bi_2O_3. $Bi_{12}GeO_{20}$ is a cubic crystal and an excellent optic-electric material comprising a 1:6 molecule ratio of GeO_2 to Bi_2O_3. $Bi_4Ge_3O_{12}$ (BGO) is a congruent melting compound, and it can be grown directly from a melt in the same composition. The melting temperature is 1317 ± 4 K (1044 ± 4 °C), corresponding with the composition $2Bi_2O_3$:$3GeO_2$1-5). In our experiment, the melt point of BGO is around 1050 °C.

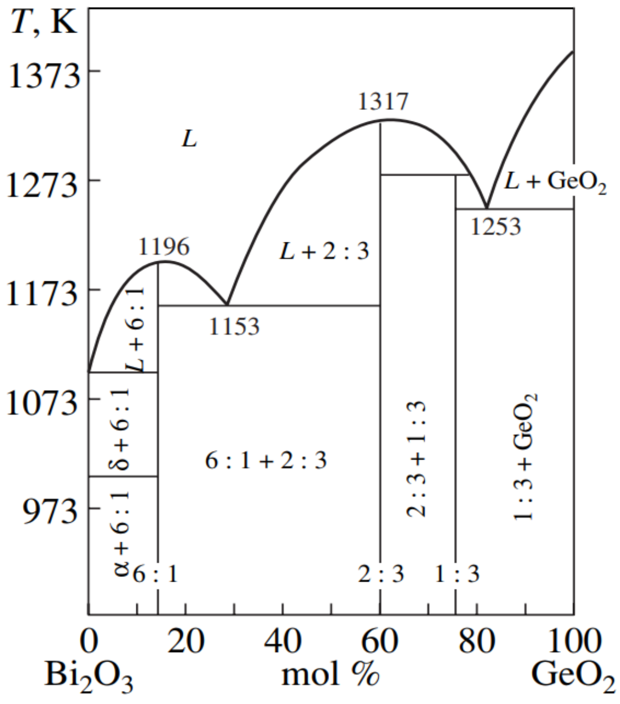

Fig. 3-1 Phase diagram of Bi_2O_3-GeO_2 binary system.1)

3.1.2 Vertical Bridgman technique

Based on the principle of directional solidification, the Bridgman method is an important crystal growth technique.[6,7] The growth of BGO single crystal is achieved by melting the raw oxides of Bi_2O_3 and GeO_2 in a platinum (Pt) crucible and freezing melt from one end (seed) to the other end (tail). Our proposed technique involves the movement of solid-melt interface along the vertical direction. The crystal growth configuration comprises multiple-crucible furnaces with a temperature profile designed as a negative gradient parallel to the growth direction, primarily in the vicinity of the solid-melt interface with the major portion of the melt and growing crystal. The BGO single crystal seed is positioned on one end of the vertical Pt crucible. Crystal growth is implemented by the controlled shifting of the temperature profile relative to the crucible.[8] This process is achieved by mechanically moving the Pt crucible relative to the fixed baffle inside the furnace.

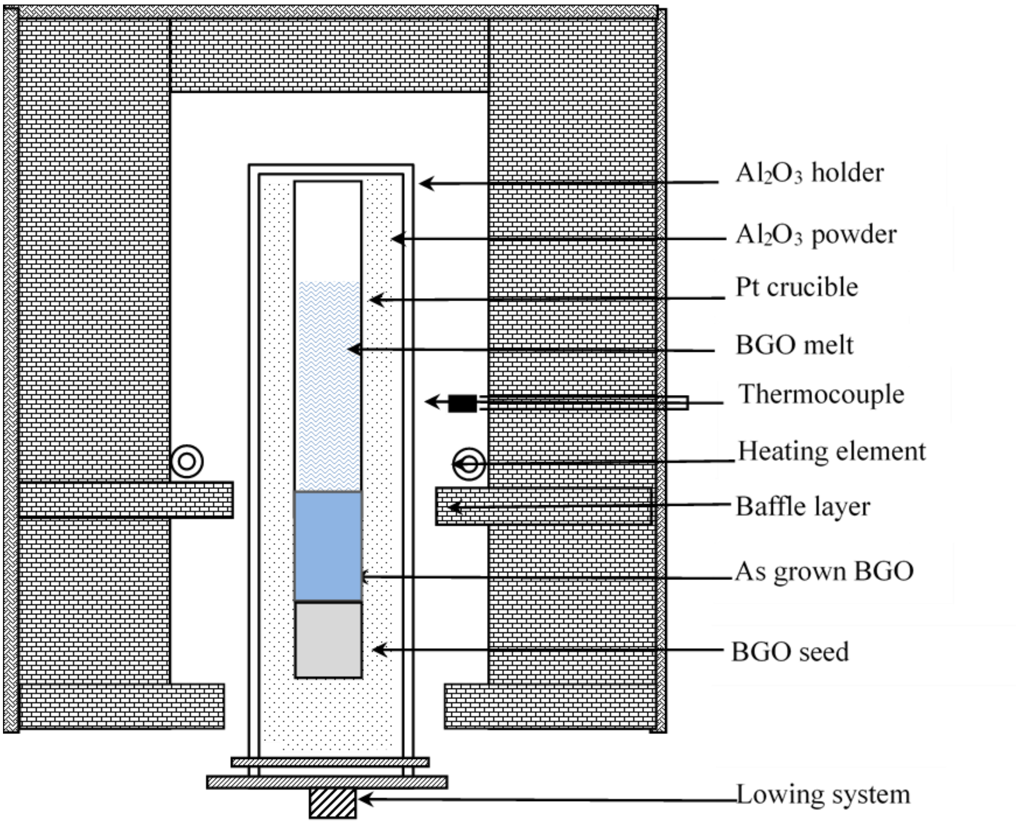

Fig. 3-2 Schematic of vertical Bridgman furnace.[8]

The vertical configuration with multiple crucibles has been used for many years to mass-produce BGO crystals in SICCAS, as it has the advantage of much higher yield (i.e., BGO crystals from multiple Pt crucibles). The side view is shown in Fig. 3-2.

The increasing interest in the Bridgman technique can be attributed to the simplest principle of melt growth. This technique also offers several advantages such as crystal shaping, low volatility, massive production, and cost-effective in contrast to the Czochralski method. The Bridgman technique is suitable for computer modeling and automatic process control because long BGO crystals can be produced without any diameter control, and the thermal stress inside a growing crystal is low. The equipment costs are also lower than those for Czochralski techniques.

Three different temperature sections can be divided from the top to bottom in the Bridgman furnace. The high temperature area is designed for melting polycrystals with the raw oxides GeO_2 and Bi_2O_3. The gradient temperature area is designed for crystallization, and the low temperature area with lower heating power is designed to prevent the crack of BGO pulling away from the baffle layer, as shown in Fig. 3-3.

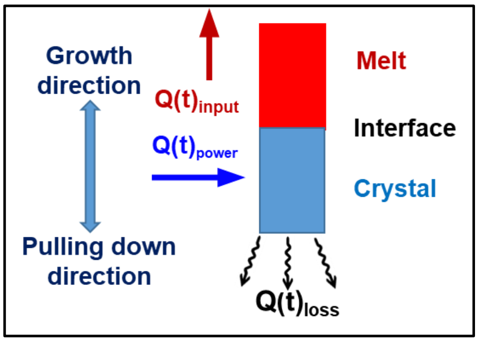

Fig. 3-3 Illustration of thermal equilibrium during crystal growth.

The furnace chamber is primarily made of high-temperature insulation alumina bricks, and some asbestos fibers are used as a thermal insulation layer out of the furnace framework. Silicon molybdenum rods are used as heating elements, which could provide a stable temperature profile, maintaining 1200 °C in the high-temperature area, which is about 150 °C above the melting temperature of BGO crystals.

Considering the kinetics of and thermal balance during a Bridgman growth is important, as shown in Fig. 3-3 and Eq.3-1. Stability of the solid–melt interface is achieved by the dynamic control of thermal balance.

$$Q(t)_{power} = Q(t)_{input} + Q(t)_{loss} \tag{3-1}$$

where $Q(t)_{power}$ is the total thermal energy supplied by heating power, $Q(t)_{input}$ is the thermal energy maintaining for crystal growth, and $Q(t)_{loss}$ is the thermal loss from pulling down bulk crystal.

$$\frac{\partial Q(t)_{power}}{\partial t} = \frac{\partial Q(t)_{input}}{\partial t} + \frac{\partial Q(t)_{loss}}{\partial t} \approx \frac{\partial Q(t)_{loss}}{\partial t} \tag{3-2}$$

According to Eq. 3-2, as the heat required for crystal growth is basically constant, the heating power supply for the furnace is added suitably as the amount of heat dissipation increases with the bulk crystal. With a growing crystal is pulled down away gradually from the baffle layer during the growth process, the thermal loss increases, especially at the later period for the 600 mm-long BGO crystal.

3.1.3 Modified vertical Bridgman method

For the reason mentioned above, an innovative design is created for the furnace to prepare 600 mm-long BGO crystals. Apart from the main heating section, an auxiliary heating module$^{4)}$ is adopted in the Bridgman furnace to provide a continuous heat supply and thus ensure a thermal equilibrium for the dynamic process of thermal transportation during the growth process, as shown in Fig. 3-4. This strategy is called the MVB technique in SICCAS.

The MVB furnace has two heating sections, one is the upper main heating module, situated near the baffle layer, with the temperature (1250 – 1350 °C) set to be higher than the melting point of 1050 °C to ensure sufficient melting of the raw oxides (Bi_2O_3 and GeO_2). Another is auxiliary heating module (around 500 °C) at the lower section of the furnace is situated far from the baffle to control the thermal dissipation during growth. The function of the lower section is heating to reduce the thermal conduction of the as-grown long BGO crystal boule, as shown in Fig. 3-4.

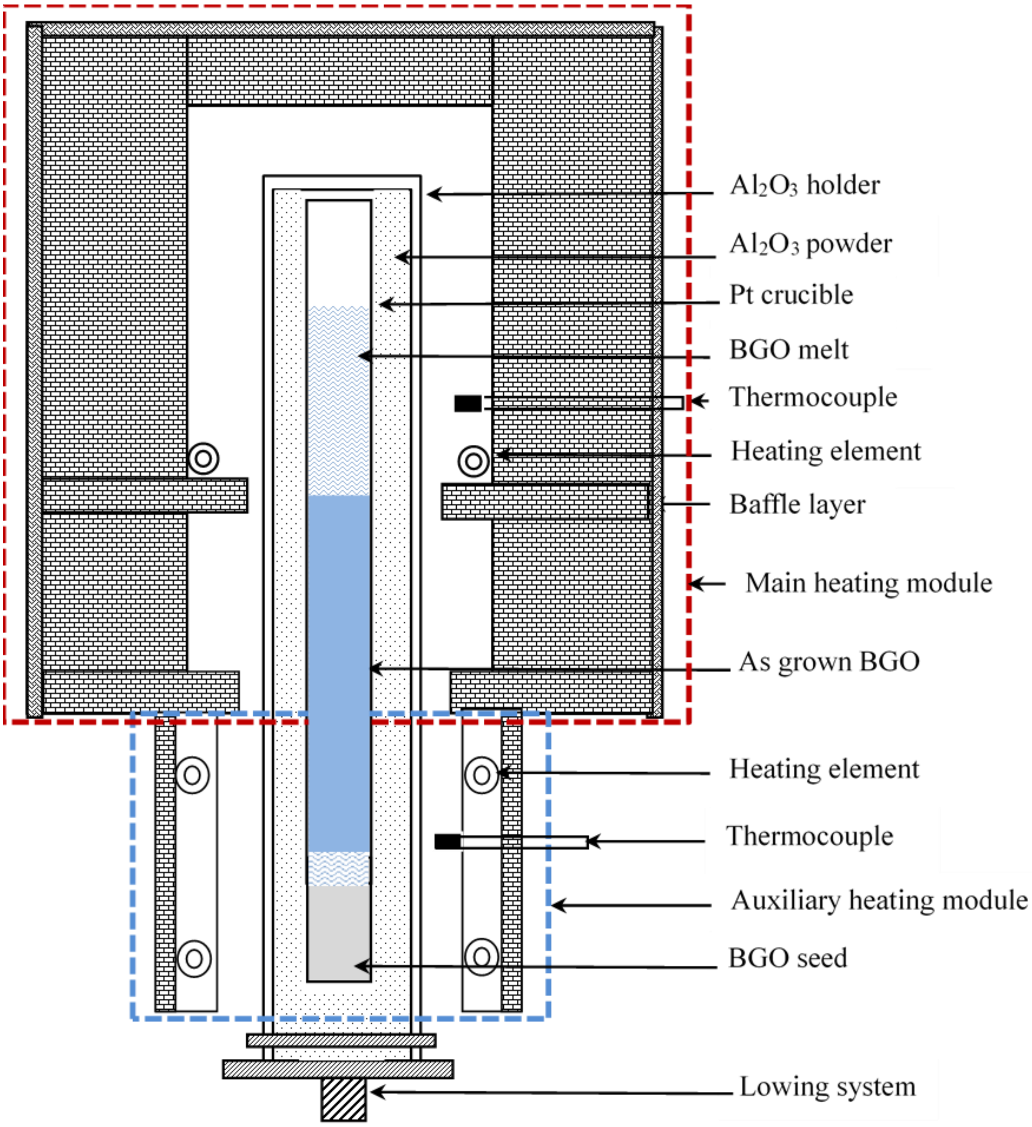

Fig. 3-4 Schematic of vertical Bridgman furnace modified by auxiliary heating module.8)

Between the high and low temperature zones is an insulating layer in the furnace with a certain thickness, which is usually made of high-quality refractory materials to provide an appropriate gradient for crystallization.9,10) It is a key point for growing high-quality 600 mm-long BGO crystals as its controls the driving force of a longitudinal temperature gradient or the supercooling at the solid-melt interface during the vertical solidification of BGO crystals. By designing the furnace configuration with the thickness and shape of the thermal-insulation layer and its relative position with the crucible, as well as by changing the position heating power, the temperature gradient is effectively optimized to fit the crystallization for growing high-quality 600 mm-long

BGO crystals. The Pt crucible is placed in the aluminum oxide (Al_2O_3) holder and filled with Al_2O_3 powder used to support the soft Pt crucible at high temperature. Several Al_2O_3 holders are placed at the parallel pedestals on the same layer of the framework to grow more BGO crystals at the same time. The automatic pulling-down mechanism is used to control the crucibles up and down with various speeds automatically in the Bridgman furnace. The thermocouple Pt-Rh protected by a corundum tube is used for the temperature measurement and the power control for the heating system of a furnace. Two thermocouples are placed at the upper and lower positions of the Al_2O_3 holder. The upper thermal couple is used to measure the high temperature in a crucible to monitor the solid–melt interface, and the lower thermal couple is just at the top level of the seed crystal to ensure seeding at a suitable temperature.11)

3.1.4 Transportation of growth units and interfacial reaction

Apart from the temperature profiles and pulling-down speed, thermal-dissipation control is a key issue in the growth process of 600 mm-long BGO crystals. To maintain the interface stability and keep a suitable temperature gradient, a tiny convex close to the plane of the solid-melt interface is formed. The three typical solid-melt interfaces12-15) are shown in the Fig. 3-5.

If the heating supply at the later period is insufficient for growing 600 mm-long BGO crystal, the temperature gradient decreases, thereby easily forming a convex interface. The unstable convex solid-melt interface produces scattering particles. If the added

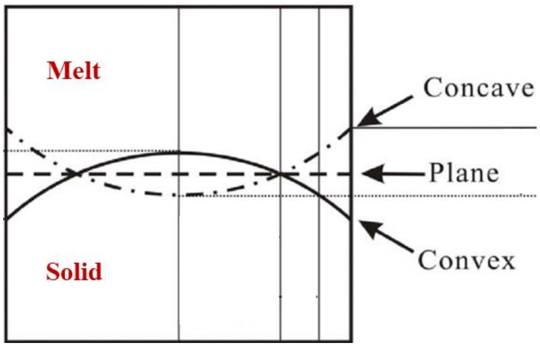

Fig. 3-5 Schematic of solid-melt interfaces.12)

heating power is excessively high, the temperature gradient becomes too large. Consequently, a concave solid-melt interface forms, and negatively affects the compositional segregation to easily produce some defects. Meanwhile, an as-grown crystal is easier to crack due to the large temperature gradient at the bottom part of the BGO crystal.

For a seeded growth, an almost 900 mm-long Pt crucible was adopted to accommodate the shaping requirements of DAMPE for the BGO crystals. Compared with other metal crucibles, Pt had a smaller coefficient for thermal expansion and acquired less induced strain and stress during cooling after the growth process. The crucible movement was automatically controlled by an upward-downward module, and the longitudinal temperature profile was optimized by adjusting the upper and lower heating powers of the furnace.

Before the crystal growth, the raw materials, GeO_2 and Bi_2O_3 powders, were mixed and then the mixture was heated. This process made it possible to feed more volume of GeO_2-Bi_2O_3 in the Pt crucible to grow ultra-long BGO crystals. During the MVB growth, the Pt crucible was heated at about 1200 °C (150 °C above the melting point) for approximately 48 h to ensure complete melting of the raw oxides, thereby allowing the formation of a homogeneous melt before the starting process of crystal growth. The oxidation atmosphere could prevent the decomposition and volatilization of BGO melt components during crystallization.

As mentioned in Section 1.2.1 and Fig. 1-5, the BGO atomic arrangement is characterized by its distorted octahedral $[BiO_6]^{9-}$ and isolated tetrahedral $[GeO_4]^{4-}$.15-18) BGO crystal growth involves two processes; one is a transportation of growth units from melt to crystal surface, and another is an interfacial reaction. There is a transition region from melt to crystal in the growth process, which is called the boundary layer. This structural feature in the boundary layer is differs from that in the melt and crystal. The Bi-O-Ge bond vibration and Bi-O-Bi and O-Bi-O bond vibration disappear in the melt, and the tetrahedral $[GeO_4]^{4-}$ and Bi^{3+} exist independently. Then, the long-range order structure disappears. However, $[GeO_4]^{4-}$ and $[BiO_6]^{9-}$ exist in the boundary layer, which is much similar with the lattice structure of BGO crystal than the melt.[19)]

In the boundary layer, Bi-O-Ge bridge bonds connect tetrahedral $[GeO_4]^{4-}$ and Bi^{3+} stepwise to form a growth unit comprising distorted octahedral $[BiO_6]^{9-}$ and isolated tetrahedral $[GeO_4]^{4-}$. The schematic of structure transforms of the growth units from melt to crystal is shown in Fig.3-6.[11)]

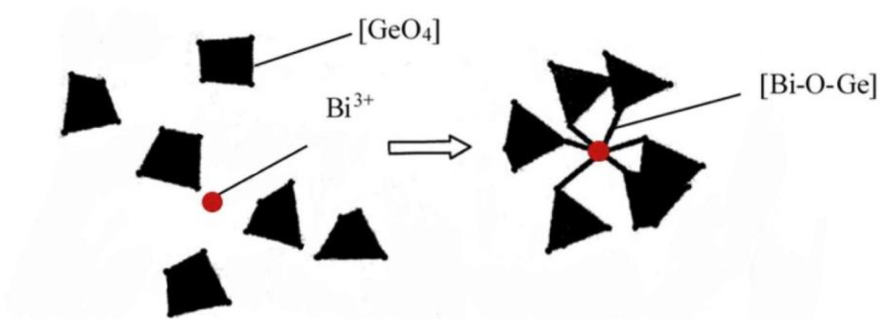

Fig. 3-6 Schematic diagram of transform of growth units from melt to crystal.[11)]

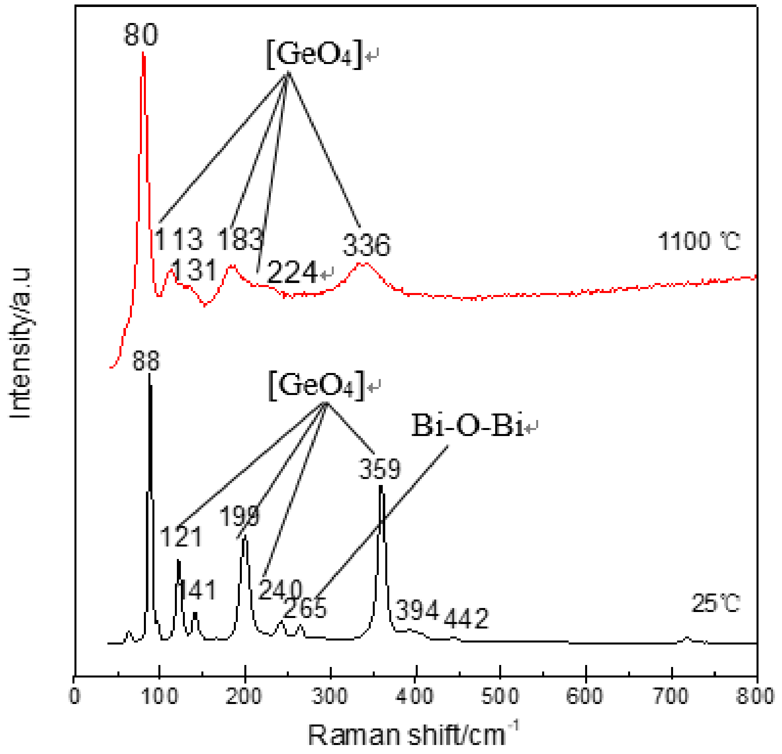

Fig. 3-7 Raman spectrum of BGO crystal at 25 °C and 1100 °C.

During transport process of the growth units, the temperature profile governs the transport rate of the growth units in the Bridgman furnace. In particular, the supercooling temperature in the boundary layer of the solid-melt interface determines the diffusion and transport rate of the growth units.

$[GeO_4]^{4-}$ and $[BiO_6]^{9-}$ and their clusters from the melt to crystal surface could be evidenced directly by the Raman peaks of BGO at room temperature and its melt, as shown in Fig 3-7. Notably, the centers of the peak shift to the low frequencies to different degrees with the increased temperature.

Transport rate of the growth units from melt to the interface could be effectively controlled to ensure an optimized reaction rate of the growth units on the crystal interface for growing high-quality BGO crystals by designing the furnace configuration with a precise temperature profile, and placing the Pt crucible in the appropriate furnace position.

During the process of interfacial reaction, the growth units $[GeO_4]^{4-}$ and $[BiO_6]^{9-}$ will combine with the free bonds of various ions on the crystal surface to induce large crystal growth gradually.19) When the supercooling is large, it is difficult to control rate surface reaction, and large clusters of the growth units $[GeO_4]^{4-}$ and $[BiO_6]^{9-}$ form. Consequently, growing high-quality BGO crystal becomes difficult. When the undercooling is low, the growth units $[GeO_4]^{4-}$ and $[BiO_6]^{9-}$ with small clusters are well organized on the surface reaction by the two-dimensional layer growth mechanism, thereby avoiding the roughening surface growth mechanism with a fast rate for growing BGO crystals.11) The prefect lattice structure of BGO crystal can be easily obtained during the two-dimensional layer growth mechanism with the high-quality BGO crystals.

Anion-coordination polyhedrons are of two types, namely, tetrahedral $[GeO_4]^{4-}$ and octahedral $[BiO_6]^{9-}$ in a unit cell, where $[GeO_4]^{4-}$ tetrahedron is primarily a covalent bond with much stronger force than that of $[BiO_6]^{9-}$ octahedron with ionic bond. Therefore, the structure of BGO crystal is primarily governed by the connection mode of tetrahedral $[GeO_4]^{4-}$. The projection of four $[GeO_4]^{4-}$ tetrahedra connected on the

(100) plane with the vertex forms a regular quadrangle. The edges of this quadrangle are the edges of the tetrahedron. The four quadrangles are connected by four $[GeO_4]^{4-}$ tetrahedra to form a longitudinal and transverse bond chain, which is parallel to the unit cell axis ***a*** and ***b***.11)

The structures of the growth units are usually in agreement with the elementary anion-coordination units within the BGO crystal during the surface reaction. They are connected to one another by a tetrahedral $[GeO_4]^{4-}$ chain on the (001) face with a stable structure during the surface reaction. Thus, the growth rate is slow along [001], and the impurity segregation proceed well, benefiting the growth of high-quality BGO crystals. They are also connected to one another by a plane of the tetrahedral $[GeO_4]^{4-}$chain along <111>.10) This structure is less stable in the surface reaction, so the growth rate is the fastest along <111>, and the process of impurity segregation is difficult to complete. Consequently, various defects easily form, which confers difficulty in the growth of high-quality BGO crystals.

Therefore, crystal growth along <001>-orientation is better for growing high-quality BGO crystals with a low driving force of supercooling.

Many efforts have been exerted to optimize the growth parameters (e.g., the two heating-power sections, temperature profile, and pulling-down speed) for high-quality and large-size BGO crystals through the MVB method. As-grown BGO crystals with dimensions of 25 mm × 25 mm × 680 mm are shown in Fig. 3-8.

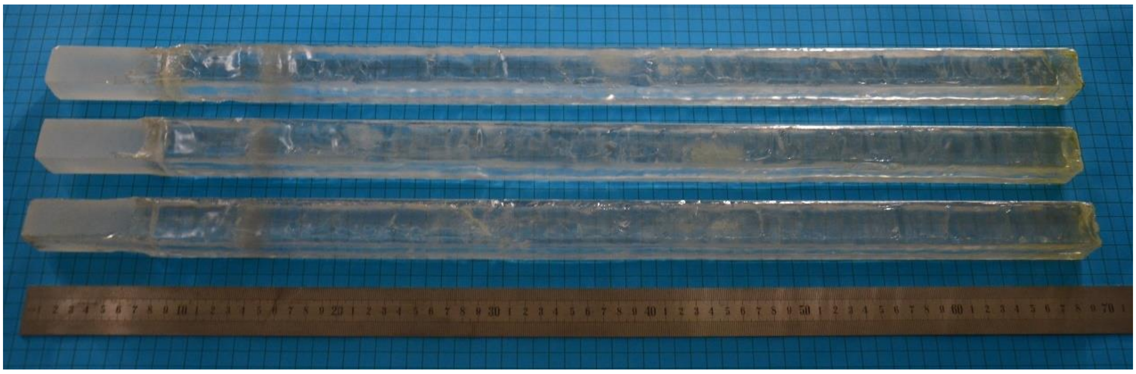

Fig. 3-8 BGO crystal boules (680 mm-long) grown by MVB in SICCAS.

3.2 Defects in BGO crystals

Many defects were easily found at the earlier growth period of the 600 mm-long BGO crystals, including the macro-defects and the micro-defects.

3.2.1 Distribution and formation of scattering particles

Macro-defects included scattering particles and impurity cores, which were easily observed by light scattering using a 532 nm solid laser beam. The scattering particles fully occupied the BGO crystals, especially in the later period of crystal growth. They were arranged periodically in layers and perpendicular to the growth direction (Fig. 3-9), obviously resulting from the fluctuation of the growth parameters.

The stability of the solid-melt interface was the key factor affecting high-quality crystal growth. The temperature gradient of less than 40 K/cm and the pulling-down speed faster than 1.0 mm/h resulted in an unstable convex solid-melt interface.

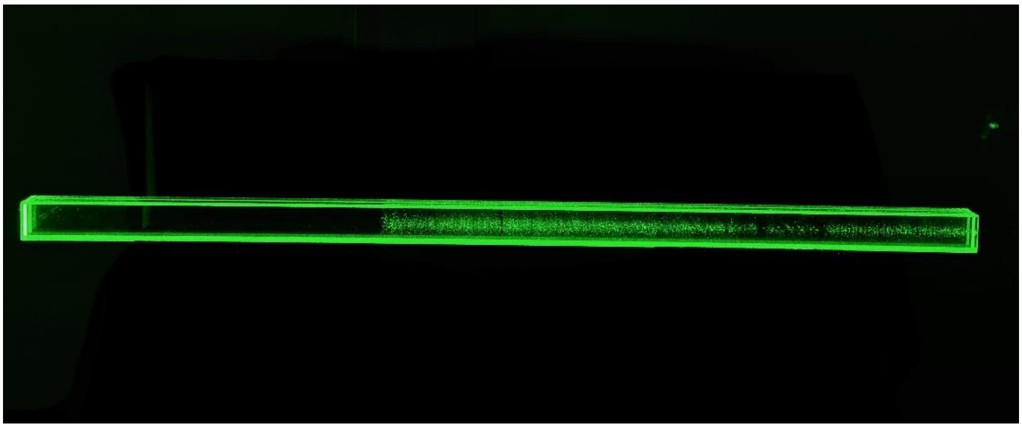

Fig. 3-9 A 600 mm-long crystal with scattering distribution.

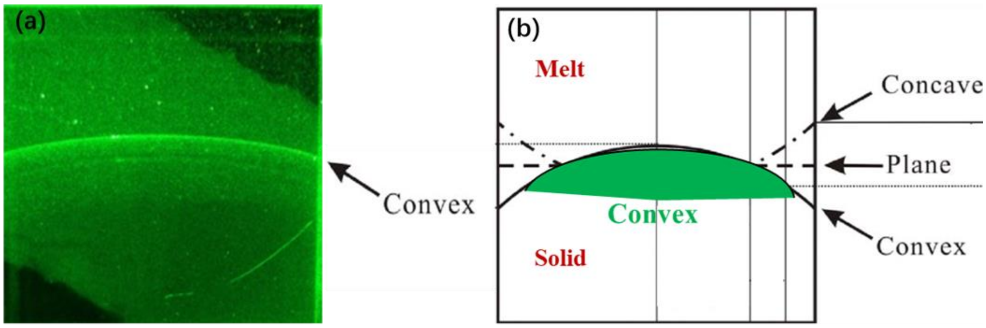

Fig. 3-10 Scattering particles (a) and schematic of convex solid-melt interfaces (b).$^{12)}$

Scattering particles were easily accumulated on the solid-melt interface, including various impurities and bubbles. The schematics of convex solid-melt interfaces and the formation of scattering particles are presented in Fig. 3-10.[12,20-22)]

3.2.2 Distribution and formation of impurity cores

Impurity cores were another type of macro-defects, and they were often observed at a later period of BGO crystal growth. They typically appeared at the center of the full-size BGO crystal along the growth direction and take shuttle-shape forms (Fig. 3-11).

The formation mechanism of the impurity core was investigated in relation to the crystal growth process. The heating power was increased at the later section of crystal growth to compensate for the thermal diffusion produced by as-grown BGO crystal boule, which is positioned far from the heating power section. During solidification,

Fig. 3-11 A 600 mm-long crystal with impurity core distribution.

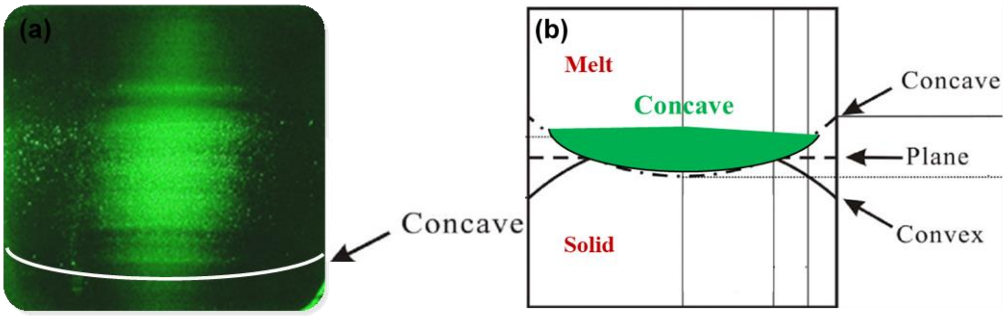

Fig. 3-12 Impurity core (a) and the concave solid–melt interfaces (b).[12)]

if an excessively high heating power is applied to disrupt the thermal balance between heating and dissipation, a concave solid–melt interface easily forms when the temperature gradient is more than 50 K/cm. A concave interface also causes a significant compositional non-uniformity in BGO crystal, even if the melt is mixed perfectly, as presented in Figs. 3-12 (a) and (b). Interface concavity could be reduced by a large longitudinal temperature gradient, but there was a risk of cracking due to high thermal stresses.6)

The impurities at the concave solid-melt interface were difficult to remove, so the impurity core could easily form at the tail end of the growth. The impurity core exerted a stronger influence on optical transmittance, and it might cause an absorption at range within 310 – 390 nm. These findings indicated that temperature stability was critical to the growth of high-optical-quality single crystals.

3.2.3 Distribution and formation of reddish color

A reddish hue was observed occasionally in a colored BGO, especially in 600 mm-long crystals, with a gradually deepening color from the seed to the tail, as shown in Fig. 3-13. The color was unrelated to the distribution position of the macro-defects23,24). These micro-defects were initially investigated by analyzing the reddish BGO crystals in this work, by using the absorption spectrum to determine whether the reddish color could be removed from the raw oxides during crystal growth. Even after many efforts, the reddish BGO crystal was difficult to draw out completely from the purified raw oxides (Bi_2O_3 and GeO_2). No correlation existed between reddish and colorless BGO in impurity concentration, rather than color center, which was a kind of point defect.26)

Fig. 3-13 Photo of as-grown reddish BGO crystal.

The reddish BGO crystals seriously affect the optical and scintillation performance. The method of eliminating the reddish color and its formation mechanism are discussed in Chapters 4 and 5, respectively

3.2.4 Optimized growth parameters

Aiming to reduce the heat conduction of the grown crystal, the thickness of the baffle layer was optimized, and the temperature profile and the position of the solid-melt interface by the heating module were accurately controlled to ensure the growth of high-quality BGO crystals.

The optimized growth process was eventually established through many repeated experiments. The growth parameters were summarized as a temperature gradient of 40 – 50 K/cm on the solid-melt interface, and the pulling-down speed was 0.2 – 1.0 mm/h in the MVB furnace during growth, as shown in Table 3-1.

Table 3-1 Parameters of growth process of 600 mm-long BGO.

Heating power $Q(t)_{power}$	Temperature gradient (K/cm)	Pulling-down speed (mm/h)	Solid–melt interface
Suitable	40−50	0.2−1.0	Tiny convex

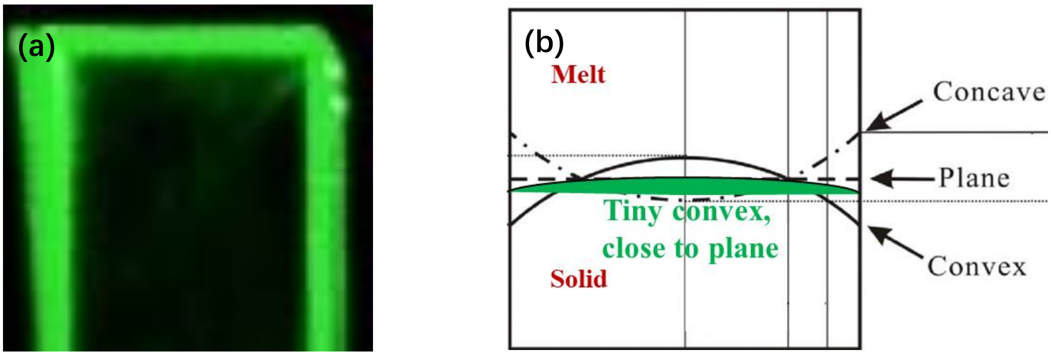

Fig. 3-14 Defect-free crystal (a) and tiny convex solid–melt interfaces (b).12)

To obtain detect-free large-size BGO crystals (Fig. 3-14 (a)), a tiny convex interface close to the plane was maintained, as shown in Fig. 3-14 (b). This could benefit impurity removal by composition segregation. Finally, high-quality and large-size BGO single crystals were prepared successfully by the MVB method (Fig. 3-15).

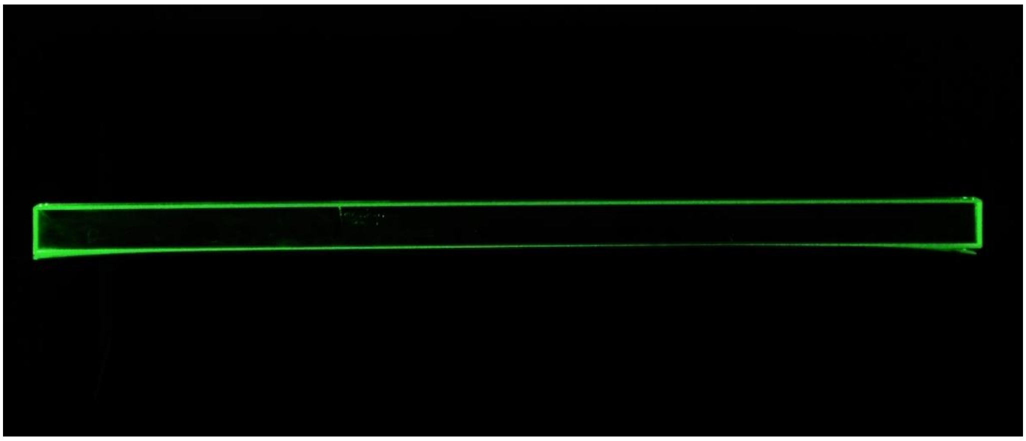

Fig. 3-15 High-quality 600 mm-long BGO single crystals.

3.3 Effect of defects on optical transmittance

The effect of various defects on the optical transmittance of the full-size BGO crystals was also investigated in this thesis. Three types of transmittance curves are shown in Fig. 3-16.

Various defects had different effects on transmittances.25) According to the transmittance spectral results of defects, the high-quality BGO crystals had a high transmittance within the visible wavelength and a sharp absorption edge. It also indicates the absence of defect energy in the energy gap. BGO crystal with impurity particles showed a lower transmittance due to light scattering, but it also did not have a defect energy, giving a relatively sharp absorption edge as well. BGO crystal with an impurity core had an extremely low transmittance, which was primarily due to the heavily absorption caused by the impurities. The reddish BGO showed a low transmittance and several absorption peaks with colored centers.

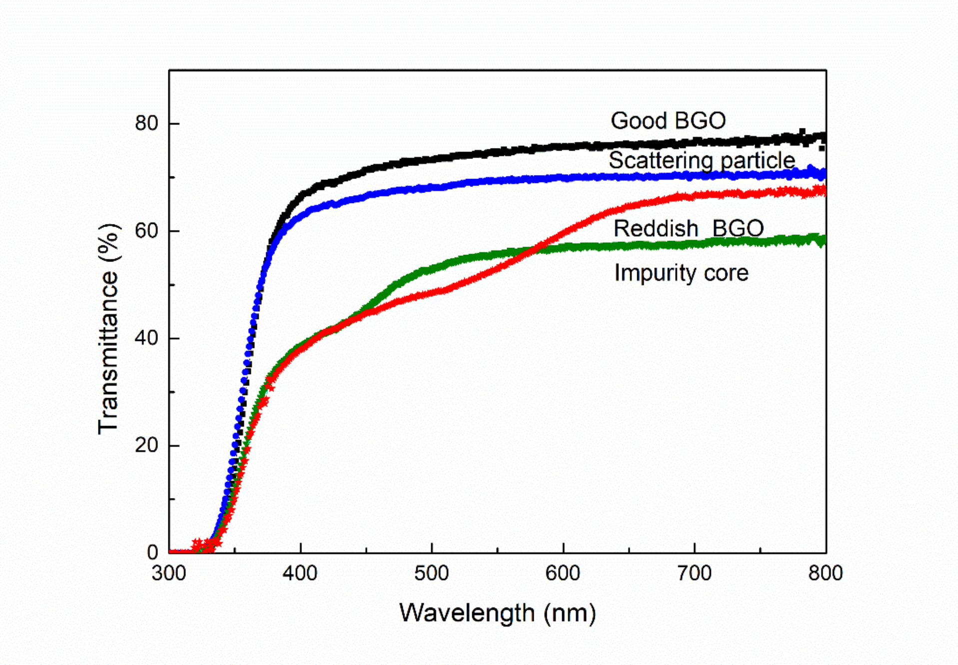

Fig. 3-16 Optical transmittance affected by different defects on BGO crystals.

3.4 Summary

High-quality and large-size BGO crystals were prepared successfully by the MVB method after the growth parameters optimized through many trials. The crystal growth mechanism was investigated by the kinetics on thermal transportation, the shape of the solid-melt interface, and the surface reaction of $[GeO_4]^{4-}$ and $[BiO_6]^{9-}$ growth units. The macro-defects, including scattering particles and impurity core were formed due to unsuitable heating power, temperature gradient and pulling-down speed. The effects of interface shape on the defects formation and distribution, including concave, convex and planar interface were discussed, and the results showed that the solid–melt interface shape influenced the crystal quality significantly. The scattering particles were caused by the convex solid-melt interface and the impurity core mainly resulted from concave solid-melt interface. The defects were remarkably reduced by balancing power heating and thermal conduction during the crystal growth. Furthermore, the micro-defects were also investigated by analyzing the reddish BGO crystals, which affected the optical and scintillation performance seriously.

References

1) V. P. Zhereb, and V. M. Skorikov, Inorg. Mater. **39**, 121 (2003).
2) V. V. Zyryanov, V. I. Smirnov, and M. I. Ivanovskaya, Inorg. Mater. **41**, 618 (2005).
3) L. Dimesso, G. Gnappi, and A. Montenero, J. Mater. Sic. **26**, 4215 (1991).
4) A.B. Kaplun, and A.B. Meshalkin, J. Cryst. Growth, **167**, 171 (1996).
5) A.Yeckel, and J. J. Derby, J. Electron. Mater. **33**, 488 (2004).
6) J.C. Brice, Crystal Growth Processes, Glasgow and London, Blackie & Son Ltd. 150 (1986).
7) P.W. Bridgman, Proc. Am. Aca. Arts Sci. **60**, 305 (1925).
8) S. Wang, H. Ni, L. Zhou, J. Chen, G. Liu, P. Zhao, L. Yuan, X. Zhou, J. Zhang, G. Song, X. Qi, Y. Li, Y. Lu, Y. Du, W. Li, M. Li, L. Xu, S. Sun, and X. Liu, An equipment and method for growing 500-1000mm long BGO crystal by modified vertical Bridgman method[P], 2012 (in Chinese).
9) M. Ishii, and M. Kobayashi, Prog. Cryst. Growth Charact. Mater. **23**, 45(1992).
10) J. J. Derby, A. Yeckel, Handbook of Crystal Growth (Second Edition), Bulk Crystal Growth, 793 (2015)
11) H. Luo, W. Zhong, China material engineering canon, Cryst. Mater. 189 (2004) (in Chinese).
12) H. Li, T. N. Wong, and N.T. Nguyen, Micro Nanosyst. **3**, 296 (2011).
13) Y. Gao, C. Wang, T.N. Wong, C. Yang, N.T. Nguyen, K.T. Ooi, J. Micromech. Microeng. **17,** (2) 358 (2007).
14) Y.F. Kargin, V.P. Zhereb, and V.M. Skorikov, Izv. Akad. Nauk SSSR, Neorg. Mater. **13**, 135 (1977)
15) P. Tissot, and H. Lartigue, Thermochim. Acta, **127**, 377(1988)
16) A. rzechnik, Acta Cryst. C **65,** i63 (2009).
17) R.A. Jackson, and M.E.G. Valerio, Nucl. Instrum. Methods Phys. Res. B **218**, 145 (2004).
18) X. Jiang, L. Su, X. Guo, H.Tang, X. Fan, Y. Zhan, Q. Wang, L. Zheng, H. Li and J. Xu, Opt. Lett. **37**, 4260 (2012).

19) S. Yin, Microcosmic mechanism of crystal growth and boundary layer model of crystal growth, Beijing, Science and Technology Publishing Press, 37 (2020) (in Chinese).

20) N.G. Bourago, A.I. Fedyushkin, and V.I. Polezhaev, Adv. Space Res. **24**, 1245 (1999).

21) V.D. Golyshev, M.A. Gonik, and V.B. Tsvetovsky, Int. J. Modern Phys. B **16**, 34 (2002).

22) D. Yao, X. Qi, G. Song, L. Yuan, and W. Zhong, J. Synth. Cryst. **33**, 940 (2004) (in Chinese).

23) F. Smet, W.J.P. van Enckevort, J. Cryst. Growth, **88**, 169 (1988).

24) S. Fan, J. Inorg. Mater. **6**, 399 (1991).

25) Z. Wei, Study on BGO doping effect and irradiation damage mechanism[D], Shanghai Institute of Ceramics, Chinese Academy of Science[D], 1987 (in Chinese).

Chapter 4 Verification of Defects in Reddish BGO Crystals

Although scintillation characteristics and radiation resistance have been described in detail in some reports, the essence of the reddish BGO single crystals still remains some puzzles for debate. Several mechanisms are proposed, and various point defect configurations are considered for free-charge-carrier capture and color-center creation to provide a microscopic interpretation of color-induced optical absorption.1) For example, the coloration of single crystals is caused by the distribution of defects, especially correlating with the existence of $V_o^{\bullet\bullet}$ in scintillation crystals.2) The $V_o^{\bullet\bullet}$ are considered as parent sites of electron traps in color-induced damage mechanism at RT.3) Similar research is also carried out in $PbWO_4$ crystal, in which a cluster of two Pb vacancies and one $V_o^{\bullet\bullet}$ is suggested as a parent site for the capture of two holes at neighboring oxygen anions.4–9)

4.1 Trace impurities

BGO crystals were prepared by the modified vertical Bridgman method. During the growth of high-quality and large-size BGO, a few reddish BGO crystals were found in the massive growth of large-size and -scale BGO crystals, as shown in Fig. 4-1.

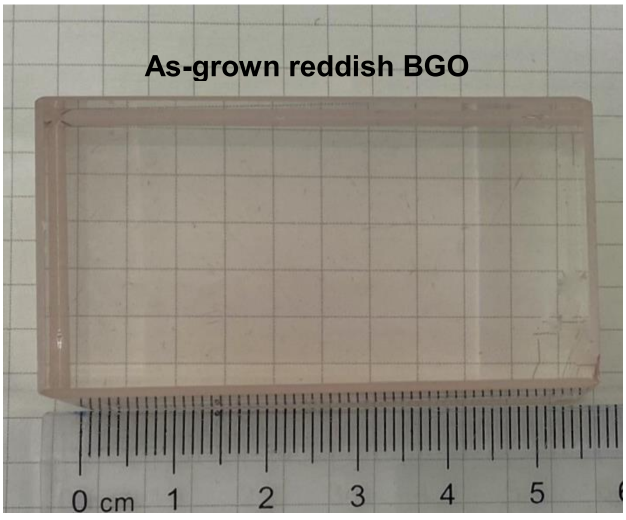

Fig. 4-1 As-grown reddish BGO crystal.

Quantitative analysis of impurity elements is a key factor to identify the mechanisms of the special coloration. Presence of impurities such as Fe and Pb may cause the coloration of BGO crystals.10,11) Therefore, the relationships between the reddish color and trace impurities were determined firstly by glow discharge mass spectroscopy (GDMS) analysis. The result of GDMS analyses for the trace elements in reddish BGO crystals are listed in Table 4-1. The trace impurities had no notable distinction between the reddish BGO and reference standard colorless BGO crystal. No clear correlations were found between the detected impurities and the reddish color in the crystal samples.

Table 4-1 Result of GDMS traces analysis (ppmw) for colored BGO samples.

Element	K	Na	Mg	Ca	Al	Si	Pb	Cr	Fe	TM[a]	RE[b]
Sample1	2.7	4.2	<0.04	1.9	0.5	2.3	<0.2	<0.03	0.13	1.0	0.18
Sample2	1.7	2.2	<0.05	1.4	0.3	1.4	<0.2	<0.03	0.43	1.3	0.10
Ref. [c]	1.8	5.2	<0.06	2.6	1.3	3.8	<0.2	<0.03	0.35	1.1	0.11

[a] Sum of transition metals.
[b] Sum of rare earths.
[c] Trace impurities in colorless BGO crystal

4.2 Oxygen vacancy

4.2.1 XPS spectrum

XPS was performed to determine the surface composition in terms of the elemental and oxidation states of the reddish BGO samples. Bi 4f XPS of the reddish BGO samples is fitted in Fig. 4-2, showing that two strong Bi^{3+} peaks with a typical Bi 4f spin-orbit doublet splitting, appear at 159.1 eV (Bi $4f_{7/2}$) and 164.4 eV (Bi $4f_{5/2}$). It was obvious that a low bonding energy tail was located in the reddish BGO. The Bi 4f peaks appeared with regard to the lowest binding energies of 156.8 eV and 162.0 eV, which indicated that there was an existence of different valence Bi ions.12,13) The curve fitting of the Bi $4f_{5/2}$ enveloped into two peaks at 164.4 and 162.0 eV, and Bi $4f_{7/2}$ enveloped into two peaks at 159.1 and 156.8 eV. The typical value of 3.0 ± 0.1 eV[14,15)] between Bi^0 and Bi_2O_3 was higher than this fitting result of 2.3 or 2.4 eV. This meant that Bi with a low valence between +3 and 0 might existed in reddish BGO. Dharmadhikari et al[16)] first considered that this low banding energy tail was owing to the appearance of the low valence state bismuth, Bi^+ and/or Bi^{2+}.

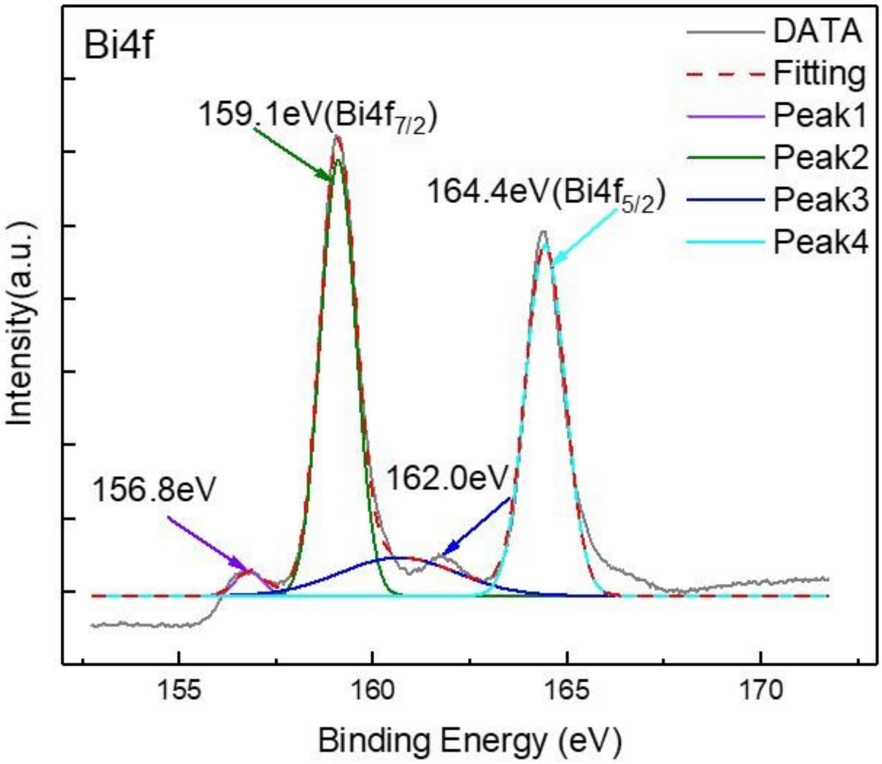

Fig. 4-2 Bi 4f XPS of reddish BGO sample.

Eqs. 4-1 and 4-2 illustrate that the formation of these low valence state bismuth centers (Bi^+ and/or Bi^{2+}) and $V_o^{\bullet\bullet}$ during the crystal preparation thermal process.[17,18)]

$$Bi_2O_3 \overset{\Delta T}{\Rightarrow} 2BiO + \frac{1}{2}O_2 \uparrow \overset{\Delta T}{\Rightarrow} Bi_2O + \frac{1}{2}O_2 \uparrow \tag{4-1}$$

$$2Bi^{3+} \leftrightarrow 2Bi^{2+}/Bi^{+} + V_O^{\cdot\cdot} \tag{4-2}$$

However, when thermal treatment is carried out in an environment with high oxygen concentration, there is also the reverse process. Bi^+ will be oxidized to Bi^{2+} or Bi^{3+} when BGO crystal annealed in oxygen or air atmosphere.

Interestingly, the reddish BGO was characterized by a series of emission peaks at the longer wavelengths.19) Emission spectrum was closely related to the valence state of Bi in crystals.20) The luminescence peaks at the longer wavelengths were ascribed to low valence state Bi centers (Bi^+ and/or Bi^{2+}).21-23) The reddish BGO could be a promising broadly ultrashort-pulse laser material based on its broadband emission characteristics.24)

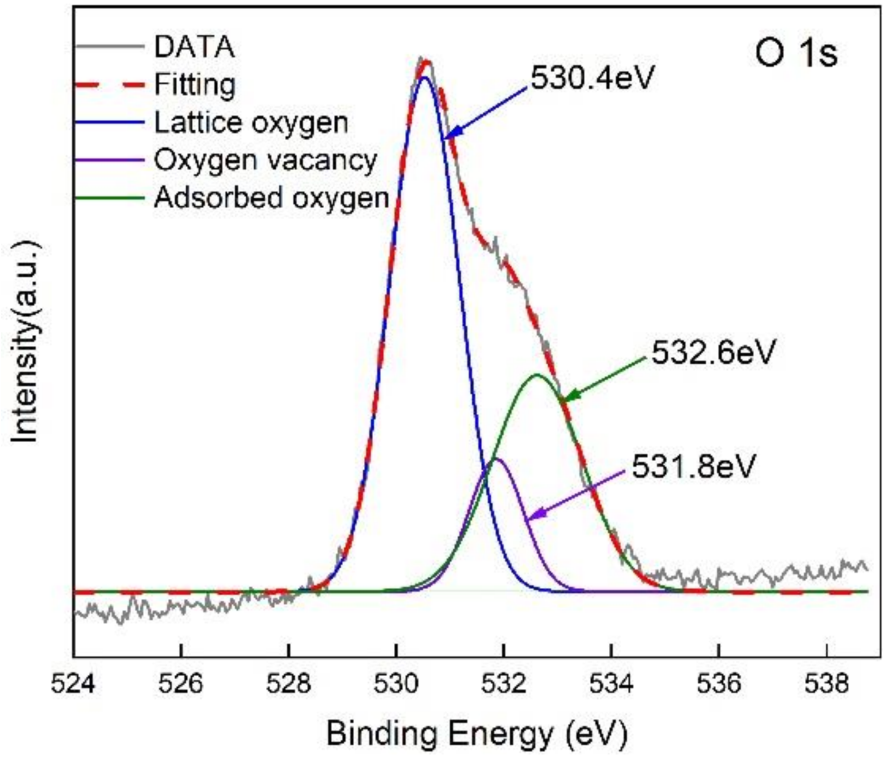

Fig. 4-3 O 1s XPS of reddish BGO sample.

Fig. 4-3 shows O 1s XPS of the reddish BGO samples. The data were fitted with Gaussian curves. There were three Gaussian components, centered at 530.4, 531.8, and 532.6 eV, respectively, indicating the presence of three types of oxygen.25) The peak at 530.4 eV corresponding to the highest intensity, was caused by lattice oxygen in BGO, whereas the peak at 531.8 eV was attributed to O^{x-} (O^{2-} and/or O^-) ions caused by $V_o^{\bullet\bullet}$;

and the peak at 532.6 eV corresponded to the adsorbed oxygen on the surface.$^{26)}$ The presence of the peak at 531.8 eV in the XPS revealed the appearance of $V_o^{\bullet\bullet}$.

4.2.2 EPR analysis

Electron paramagnetic resonance (EPR) is sensitive to the spin of $V_o^{\bullet\bullet}$ and captured $V_o^{\bullet\bullet}$ in color centers. The $V_o^{\bullet\bullet}$ is a mobile ionic defect in BGO crystals. It plays an important role in numerous chemical and physical processes.$^{27)}$ As such, identifying its structure is important for fundamental and technical points of view. Oxygen defects can be characterized through EPR, which is a highly sensitive and rapid technique.$^{28)}$

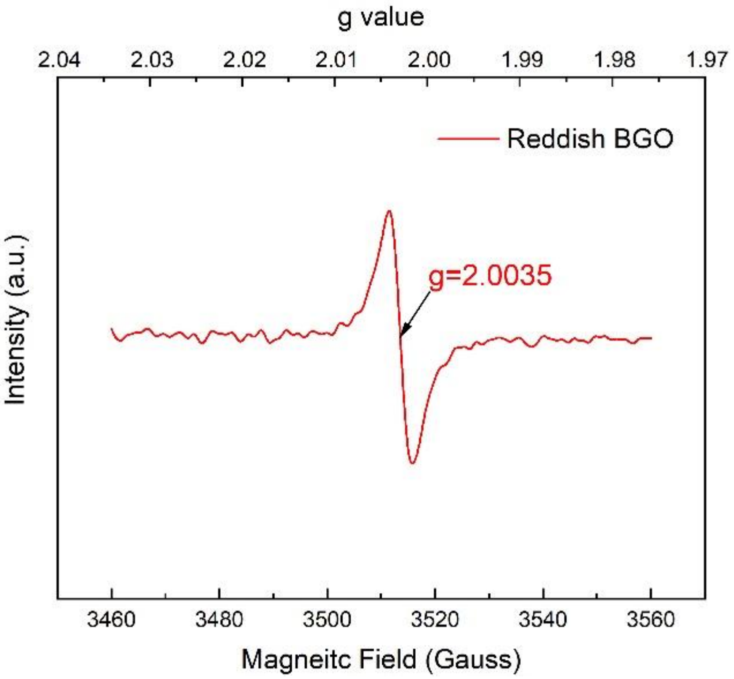

Fig. 4-4 EPR spectra of the reddish BGO sample.

When the quantum of the electromagnetic wave energy hν incident was equal to the energy difference between near energy levels, which could be described by the following resonance condition$^{29)}$, an EPR signal was observed.

$$h\nu = g\mu_B B_0 \tag{4-3}$$

where g is the spectroscopic splitting factor correlated with the kind of paramagnetic center, B_0 is the induction of the external magnetic field, and μ_B is the Bohr magneton.

RT EPR was performed to further examine the existence of $V_o^{\bullet\bullet}$ in the reddish BGO. As shown in Fig.4-4, the results revealed only one unique peak in the magnetic field range of 3460 – 3560 G, indicating that one kind of vacancy defect existed in the reddish BGO crystal lattice. Typically, a peak at 2.001 – 2.004 was attributed to natural $V_o^{\bullet\bullet}$.30) In Fig. 4-4, the reddish BGO gives an intense RT EPR signal at around 3510 G with g = 2.0035, which is attributed to the electron-trapped center around the site of $V_o^{\bullet\bullet}$.31) This finding was consistent with the XPS results.

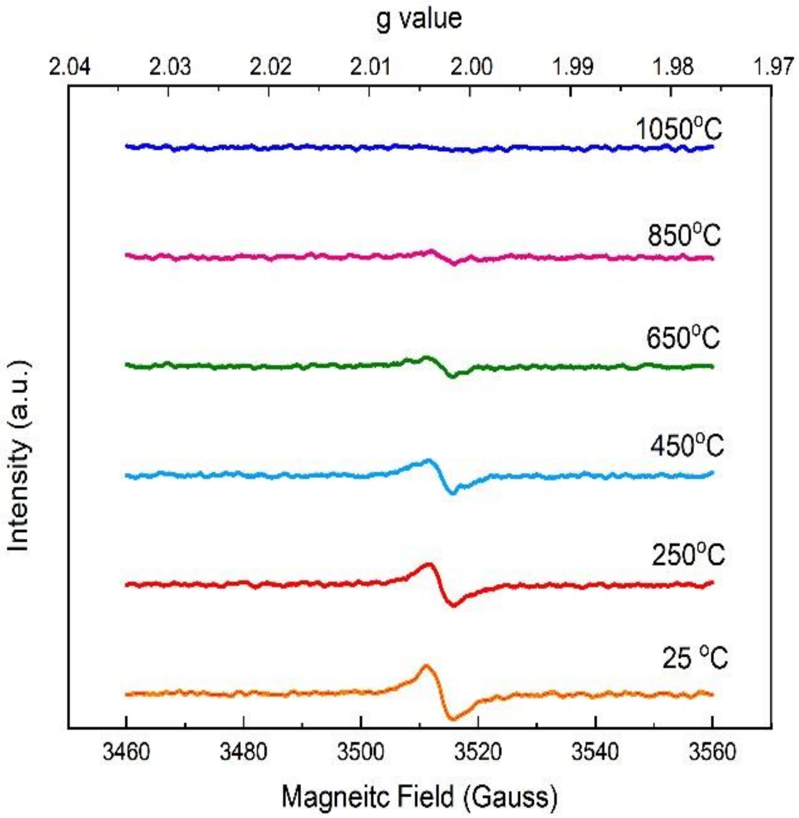

Fig. 4-5 EPR spectra of the reddish BGO samples at different temperatures.

The EPR investigation was carried out at different temperatures (range of 25 to 1050 °C) to gain more insights into the dynamic process of $V_o^{\bullet\bullet}$ and competing magnetic interactions on reddish BGO. In Fig. 4-5, the EPR spectrum shows the signal intensity at different temperatures. A strong and symmetric signal centered at the beginning was observed at $T = 25$ °C. As temperature increases, however, the signal at around 3510 G (g = 2.0035) weakened. The signal was associated with a paramagnetic behavior at different temperature.

The signal was not obviously observed in the EPR spectrum at 1050 °C, compared with that at a lower temperature because of the missing complex $V_o^{\bullet\bullet}$. At the melting temperature of BGO at 1050 °C, EPR signal of $V_o^{\bullet\bullet}$ disappeared.

4.2.3 Raman spectrum

The Raman spectra of the reddish BGO investigated from RT to its melting point 1050 °C was carried out to cross-check the EPR results, as presented in Fig. 4-6. To better understand the cluster vibrations in a reddish BGO crystal responsible for the characteristic bands observed in Raman spectra, it was useful to consider a simple model derived from classical mechanics with two masses m_1 and m_2 connected by a massless spring. The result was that the frequency of vibration was strongly dependent on the mass and the force constant (related with chemical bond) given the restoring force for unit displacement from the equilibrium position. The corresponding bond lengths between atoms increased, and the force constant among atoms increased, and

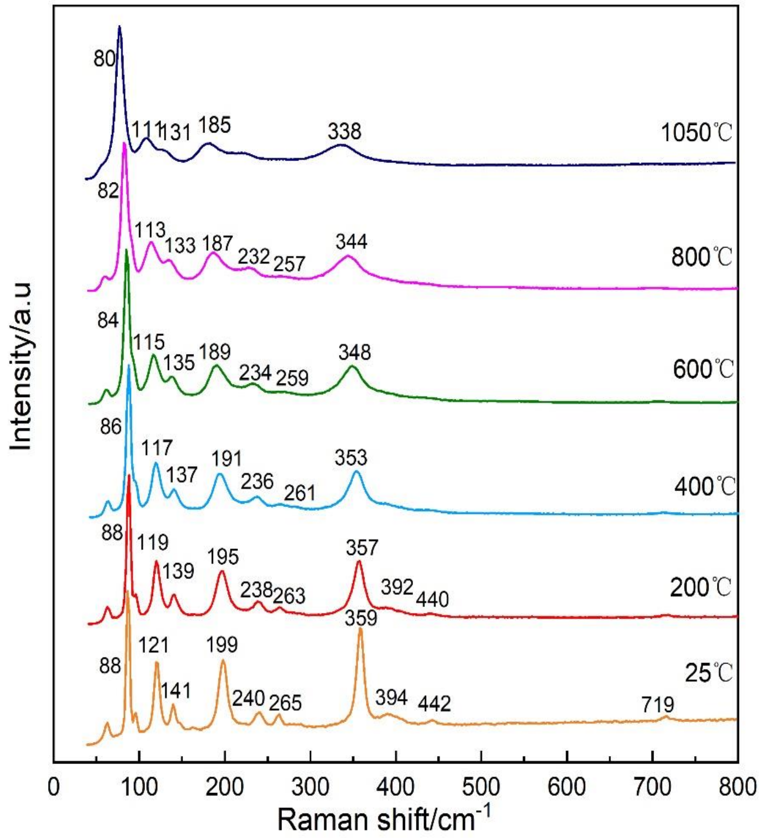

Fig. 4-6 Raman spectra of the reddish BGO samples at different temperatures.

the effort among atoms decreased with temperature increase. All the Raman peaks broadened at different degrees and shifted obviously to low frequencies as temperature increasing.32) At different temperatures, the peaks around 121, 199, and 361cm^{-1} could be obviously observed, and they were attributed to the vibrations of the tetrahedral $[GeO_4]^{4-}$.32,33) Therefore, $[GeO_4]^{4-}$ tetrahedron existed in the reddish BGO crystal and the melt. The peaks at 121 and 265 cm^{-1}, which were attributed to the bridge bond of the Bi-O-Bi and Bi-O-Ge bond, disappeared in the melt. The Bi-O bond was ionic and weaker than the Ge-O bond in BGO crystals.32,33-35) Tetrahedral $[GeO_4]^{4-}$ was connected by the Bi-O bridge bond to form a growth unit during crystal growth. When the crystal melted, $[GeO_4]^{4-}$ tetrahedron and Bi ions existed independently in the melt.32,36) This observation was consistent with our EPR results at the same temperature 1050 °C.

4.3 Bismuth vacancy

4.3.1 TEM analysis

Fig. 4-7 (a) shows a TEM micrograph of the reddish BGO crystals. Fig. 4-7 (b) is the magnified version of one cross-section of Fig. 4-7 (a). The morphological characteristics were monodispersed spheres with similar shapes and a smooth surface. HRTEM micrograph of Fig. 4-7 (c) offered a more complete view of the microstructures of the reddish BGO crystal. During the test, the higher the images resolution, the higher the temperature of the detecting electron beam. Similar to XRD, selected area electron diffraction (SAED) could provide the structural information of these samples. The dark dots shown in Figs. 4-7 (a) – (c) were nanocrystals that agree well with the results of Haro-Poniatowski.37) Fig. 4-7 (d) shows concentric diffraction rings that are characteristics of amorphous structures. The values in Fig. 4-7 (d) were consistent with the powder diffraction data file (PDF) card of the oxidations of Bi, indicating that the oxidations of Bi precipitated to the surface from the reddish BGO. It might be also significant evidence of a number of Bi vacancies produced in reddish BGO crystal.7)

$$Bi_4Ge_3O_{12} \leftrightarrow V_O^{\cdot\cdot} + V_{\mathrm{Bi}}^{'''} + Bi_2O_3 \qquad (4\text{-}4)$$

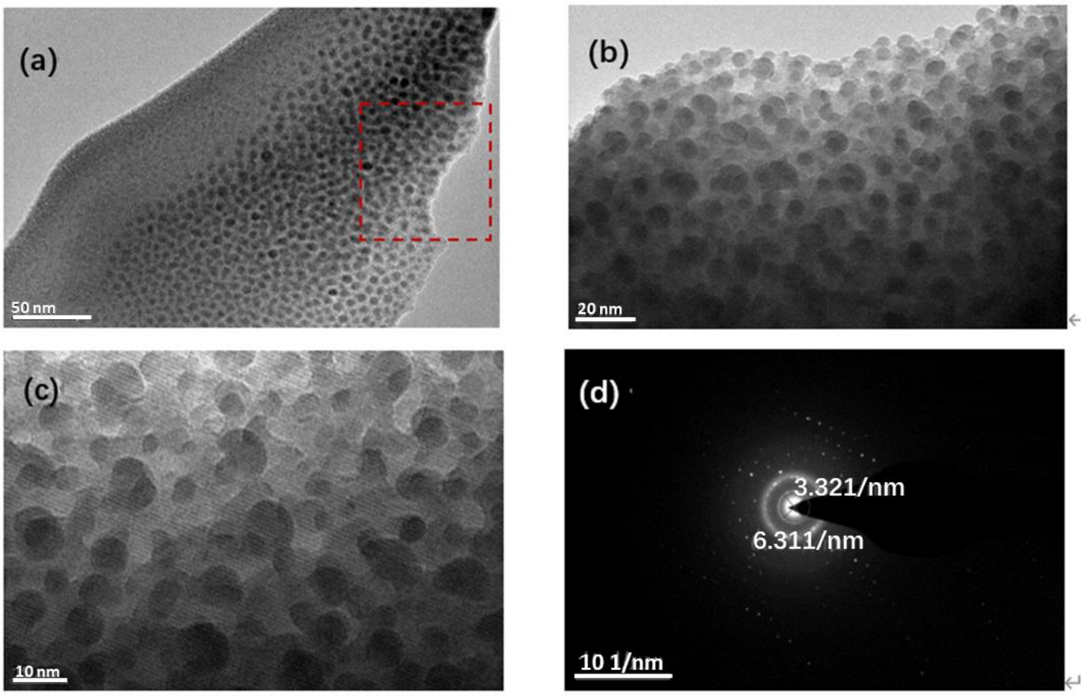

Fig. 4-7 TEM images (a) and (b), HRTEM image (c), and SAED information corresponding to (c) of reddish BGO sample (d).

This process depends on thermal treatment temperature and oxygen partial pressure in BGO. When the partial pressure of oxygen in an annealing atmosphere is high enough, Eq. 4-4 does not shift to the right-hand side as temperature increases.[38)] Thus, the crystal structure is relatively complete.

4.3.2 High-angle annular dark-field-STEM analysis

Atomic resolution high-angle annular dark-field (HAADF)-STEM was conducted to identify the crystalline structure and distribution[39)] of Bi in the reddish BGO. In Fig. 4-8, elemental mapping with sub nanometer resolution shows the nonuniformity uncorrelated spatial distribution of Bi, Ge, and O, which reveals lower Bi compared with Ge and O. Fig. 4-9 shows the TEM and nanoprobe EDS results of the reddish BGO sample. The probe size of the electron beam was about 2 nm for the EDS. The material composition was measured at two points via EDS: point 1 at the surface and point 2 at 30 nm far from the surface.[39,40)] As shown in Figs. 4-8 (c) and 4-9 (b), the TEM and

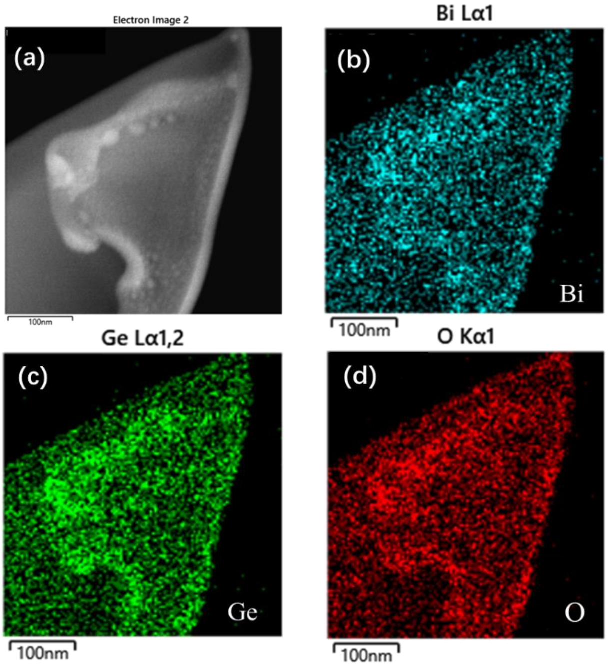

Fig. 4-8 HAADF-STEM (a) and the corresponding elemental (Bi, O, and Ge) mapping images (b – d).

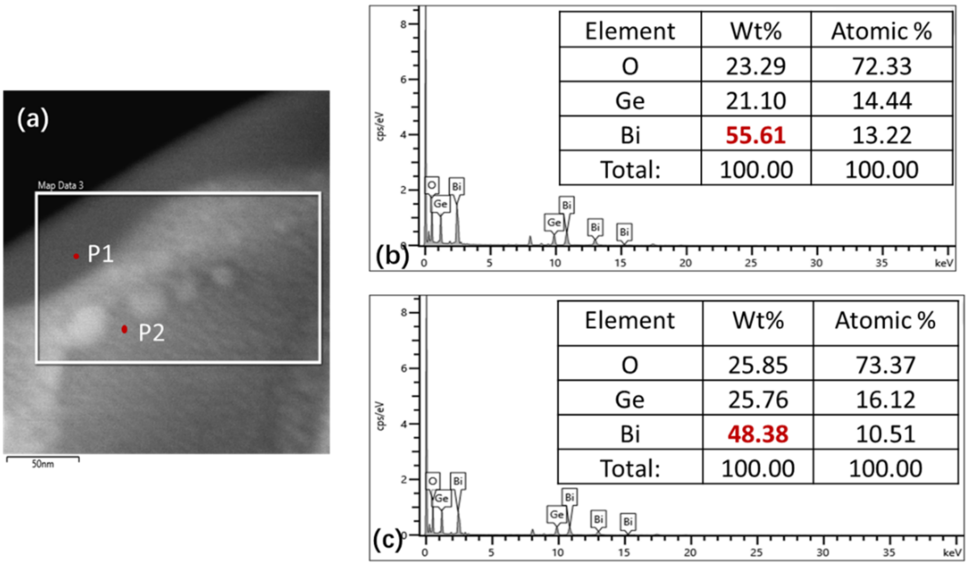

Element	Wt%	Atomic %
O	23.29	72.33
Ge	21.10	14.44
Bi	**55.61**	13.22
Total:	100.00	100.00

Element	Wt%	Atomic %
O	25.85	73.37
Ge	25.76	16.12
Bi	**48.38**	10.51
Total:	100.00	100.00

Fig. 4-9 STEM image (a) and the corresponding EDS mapping images of Bi, O, and Ge (b, c) for the reddish BGO.

EDS results indicated that the amount of Bi in the reddish crystals was seriously lower, i.e., 55.61% and 48.38%, which deviated severely from 67.04%, the stoichiometric percentage of Bi in normal BGO crystals. Consistent with the result of the elemental mapping of the reddish BGO crystal, this finding was another important evidence that a number of Bi vacancies existed.

4.4 Summary

The presence of $V_o^{\bullet\bullet}$ in the reddish BGO crystal was confirmed through EPR spectroscopy. It gave an intense signal of g ~2.0035, which was typical of a singly ionized $V_o^{\bullet\bullet}$. When BGO melted at 1050 °C, $[GeO_4]^{4-}$ tetrahedron and Bi ions existed independently. At this temperature, EPR signal of $V_o^{\bullet\bullet}$ disappeared, coinciding with the result of Raman spectra at the same temperature. It was inferred that bismuth with a low valence state might existed in the reddish BGO. In addition, the existence of V_{Bi}''' was verified by analyzing the precipitation of Bi oxidations on the crystal surface and the lack of Bi in crystal lattice. During crystal growth, $V_o^{\bullet\bullet}$ and V_{Bi}''' were produced because of the evaporation of Bi_2O_3. By annealing in the oxidizing atmosphere, oxygen in air might diffuse into the crystals, filling the lattice.

References

1) V. V. Laguta, M. Martini, A. Vedda, E. Rosetta, M. Nikl, E. Miho´kova´, J. Rosa, and Y. Usuki, Phys. Rev. B **67**, 205 102(2003).
2) R. Zhu, IEEE Trans. Nucl. Sci. **45**, 686 (1998).
3) A. Annenkov, E. Auffray, M. Korzhik, P. Lecoq, and J.P. Peigneux, Phys. Status Solidi A **170,** 47 (1998).
4) Y. B. Abraham, N. A. W. Holzwarth, R. T. Williams, and G. E. Matthews, Phys. Rev. B **64**, 245 109(2001).
5) Q. Lin, X. Feng, and Z. Man, Solid State Commun.**118**, 221 (2001).
6) Q. Lin, X. Feng, and Z. Man, Phys. Status Solidi A **181**, R1 (2000).
7) Q. Lin, X. Feng, and Z. Man, Phys. Rev. B **63**, 134105 (2001).
8) W. Zhu, X. Feng, and Z. Wu, Physica B **324**, 53 (2002).
9) L. Yuan, H. Ni, J. Chen, G. Song, X. Qi, X. Li, T. Karaki, and D. Wang, Ceram. Int. **47**, 11856 (2021).
10) R. Zhu, H. Stone, H. Newman, T. Zhou, H. Tan, and C. He, Nucl. Instrum. Methods Phys. Res. Sect. Accel. Spectrometers Detect. Assoc. Equip. **302**, 69 (1991).
11) Z. Yin, X. Feng, and G. Hu, Ferroelectrics. **151**, 287 (1994).
12) S. Kang, R. C. Pawar, Y. Pyo, V. Khare, and C. S. Lee, J. Exp. Nanosci. **11**, 259 (2015).
13) A. Aytimur, İ. Uslu, Ş. Durmuşoğlu, and A. Akdemir, Ceram. Int. **40** (8), 12899 (2014).
14) W.E. Morgan, W.J. Stec, and J. R. Vanwazer, Inorg. Chem.**12,** 953 (1973).15
15) M.W. Chu, M. Ganne, M.T. Caldes, and L.Brohan, J. Appl. Phys. **91,** 3178 (2002).
16) V.S. Dharmadhikari, S.R.Sainkar, S. Badrinarayan, and A. Goswami, J. Electron Spectrosc. Relat. Phenom. **25**, 181 (1982).
17) X. Jiang, L. Su, X. Guo, P. Yu, X. Guo, H.Tang, X. Xu, L. Zheng, H. Li and J. Xu, Laser Phys. **23**, 105812 (2013).
18) O. Sanz, E. Haro-Poniatowski, J. Gonzalo, and J. F. Navarro, J. Non-Cryst. Solids **352**, 761 (2006).

19) J.A. Duffy, J. Non-Cryst. Solids. **196**, 45 (1996).

20) R. Cao, M. Peng, L. Wondraczek, and J. Qiu, Opt. Express. **20**, 2562 (2012).

21) X. Guo, H. Li, L. Su, P. Yu, H. Zhao, Q. Wang, J. Liu and J. Xu, Opt. Mater. **34**, 675 (2012).

22) A.N. Romanov, Z.T. Fattakhova, A.A. Veber, O.V. Usovich, E.V. Haula, V.N. Korchak, V.B. Tsvetkov, L.A. Trusov, P.E. Kazin and V.B. Sulimov, Opt. Express. **20**, 7212 (2012).

23) H.T. Sun, B. Xu, T. Yonezawa, Y. Sakka, N. Shirahata, M. Fujii, J. Qiu and H. Gao, Dalton. Trans. **41**, 11055 (2012).

24) B. Yang, S. Oh, and Y.J. Kim, IEEE Trans. Nucl. Sci. **61**, 2071 (2014).

25) Y.G. Cui, J. Instrum. Anal. **15**, 17 (1996).

26) Y. Tu, S. Chen, X. Li, J. Gorbaciova, W. P. Gillin, S. Krause, and J. Briscoe, J. Mater. Chem. C **6**, 1815 (2018).

27) Y. Lv, C. Pan, X. Ma, and R. Zong, Appl. Catal. B **138**, 26 (2013).

28) Y. Lv, Y. Liu, and Y. Zhu, Mater. Chem. A **2**, 1174 (2014).

29) V. P. MLenahan, Micro. Engin. M. Bednarowicz, B. Dobosz, R. Krzyminiewski, M. Hałupka-Bryl, T. Deptuła, Y. Nagasaki, Mater.Chem. Phys., **161**, 250 (2015).

30) V. Ischenko, S. Polarz, and D.Grote, Adv. Funct. Mater. **15**, 1945 (2005).

31) Y. Lv, Y. Liu, and Y. Zhu, J. Phys. Chem. C **117**, 18520 (2013).

32) X, Zhang, S. Yin, S. Wan, J. You, H. Chen, S. Zhao, and Q. Zhang, Chin Phys. Lett, **24,** 1898 (2007).

33) H. Qiu, A. Wang, and X. Liu, Spectrosc. Spectral Anal. **25**, 529 (2005).

34) G.D. Chryssikos, M.S. Bitsis, J.A. Kapoutsis, E.I. Kamitsos, and J. Non-Cryst. Solids 217 (1997).

35) M. Srinivasa Reddy, G. Naga Raju, G. Nagarjuna, and N. Veeraiah, J. Alloys Compd. **438**, 41 (2007).

36) P. Yu, L. Su, H. Zhao, and J. Xu, J. Lumin. **154**, 520 (2014).

37) E. Haro-Poniatowski, M. Jimenez de Castro, J.M. Fernandez Navarro, J.F. Morhange and C. Ricolleau, Nanotechnology **18,** 315703 (2007).

38) O. Sanz, E. Haro-Poniatowski, J. Gonzalo and J M F, Navarro, J. Non-Cryst. Solids **352**, 761 (2006).

39) J. Di, C. Chen, S. Yang, S. Chen, M. Duan, J. Xiong, and C. Zhu, Nat. Commun. **10**, 2840 (2019).

40) X. Wu, J. Zhou, A. Duda, J. C. Keane, T.A. Gessert, Y. Yan and R. Noufi, Res. Appl. **14**, 47 (2006).

Chapter 5 Annealing Effects on the Reddish BGO Crystals

The BGO crystals prepared by the MVB method [1-7] occasionally exhibit reddish colors, especially in the large-size crystals, resulting in the deterioration of optical transmissions, LO, and ER for DAMPE application.[6,7]

Even if the growth conditions are optimized under the detailed consideration, reddish BGO cannot be avoided totally in as-grown crystals. The BGO sample with dimension of 20 mm × 20 mm × 30 mm was cut from the full size of 25 mm × 25 mm × 600 mm, shown in Fig. 5-1. The coloration of single crystals is caused by the distribution of defects, especially correlating with the existence of $V_o^{\bullet\bullet}$ in scintillation crystal,[8] as mentioned in Chapter 4. It is reported that the reddish BGO crystals might be associated with the presence of OH^- substitutes an O^{2-} and OH^- and/or color centers, and thus affecting the energy level of some Bi^{3+} particles.[9] The formation mechanism on the model of defects should be further studied in order to eliminate the reddish in BGO.

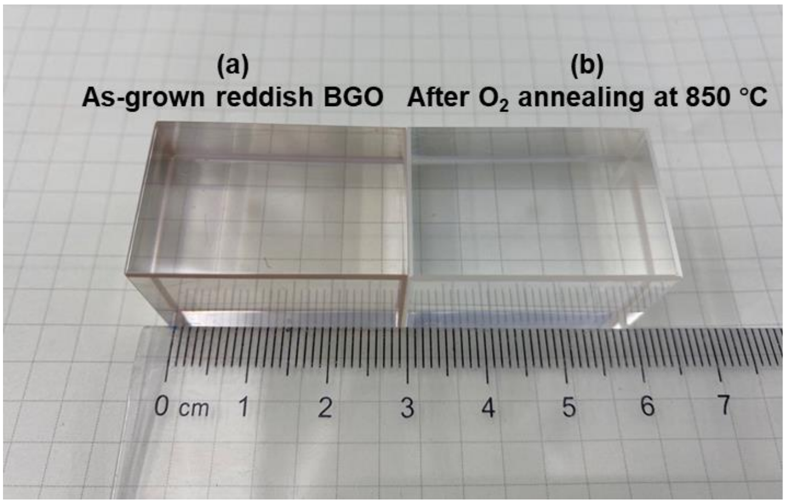

Fig. 5-1 As-grown reddish BGO (a) and reddish BGO after O_2 annealing at 850 °C (b).

First of all, the problem on great majority of the reddish BGO crystals could be solved in growth process. Then annealing experiments were conducted for the reddish crystals treated with a series of temperature and different atmosphere (oxygen, nitrogen, and vacuum) to verify the origin of the reddish BGO crystals.[10] The annealing experiments on reddish BGO crystals were performed at 250, 450, 650, and 850 °C for 4 h, respectively, keeping the gas (oxygen, vacuum, and nitrogen) flow rate at 15 ml/s for 12 h, including 4 h heating and 4 h cooling.

5.1 Oxidizing atmosphere annealing

As shown in Fig. 5-1 (b), the reddish color in BGO could be effectively eliminated via thermal annealing at 850 °C for 4 h under oxygen atmosphere.

5.1.1 Improvement of transmittance

The optical transmission of the reddish BGO crystal keeps constant if the annealing process is below 650 °C. However, the crystal quality could be greatly improved by increasing the annealing temperature. The reddish color changed into colorless after annealing in an oxygen atmosphere at sufficiently high temperature ($\geq$850 °C). The optical transmission is greatly increased by approximately 20% at 480 nm after annealing in oxygen until 850 °C.

To determine the optimum oxygen annealing condition, the annealing temperature was increased in oxygen atmosphere to 900 °C /4 h. The properties of the samples were not further improved even if the annealing time was extended from to 4 h to 10 h. This finding indicated that the annealing at 850 °C for 4 h was enough for eliminating the reddish color in BGO crystals. Hence, 850 °C/4 h in oxygen annealing is the optimized experimental condition to eliminate the reddish in BGO crystals.

Considering that the reddish color could be removed by the annealing under the oxygen atmosphere, the formation of the color centers was investigated with the existence of $V_o^{\bullet\bullet}$. We compared the optical transmittances and absorptions of both the reddish crystals before and after annealing in the visible range of 300 – 700 nm in order to verify the $V_o^{\bullet\bullet}$.

Fig. 5-2 presents the transmittance spectra of reddish crystals before and after annealing and the theoretical transmittance T_S that could be calculated as follows:[11,12)]

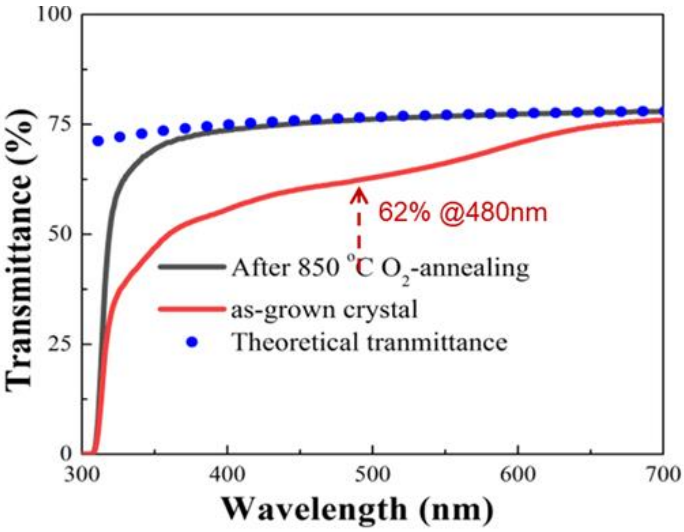

Fig. 5-2 Transmission spectra before and after 850 °C O_2 annealing for as-grown reddish BGO crystals. The theoretical transmittance is also presented.

$$T_s = (1-R)^2 + (1-R)R^2(1-R) + \cdots$$

$$= (1-R)/(1+R), \tag{5-1}$$

where

$$R = (\frac{n_{BGO}-n_{air}}{n_{BGO}+n_{air}})^2, \tag{5-2}$$

where n_{BGO} and n_{air} are the refractive index of BGO and air, respectively. The crystal's optical quality can be justified from the measured transmittance and T_s.

The reddish crystal had a poor transmittance before annealing in the wavelength range of 300 – 700 nm, especially below 600 nm, which was much lower than the theoretical value of approximately 62% at 480 nm, as shown in Fig. 5-2. After annealing, the crystal became good and approached to the theoretical transmittance.

Fig. 5-3 shows difference of subtracting transmittance spectra of the reddish BGO from that of the O_2-annearfed BGO shown in Fig. 5-2. The difference curve corresponds to the induced absorption caused by the reddish color. Before annealing, the reddish BGO crystals exhibited notably three more peaks in the visible absorption band than the O_2-annearfed BGO at approximately 506, 389, and 332 nm, corresponding to the energy levels of 2.45, 3.20, and 3.74 eV, respectively. Usually, the defect of $V_o^{\bullet\bullet}$ in an oxide has been reported in yellow-color energy region. For example, energy level of

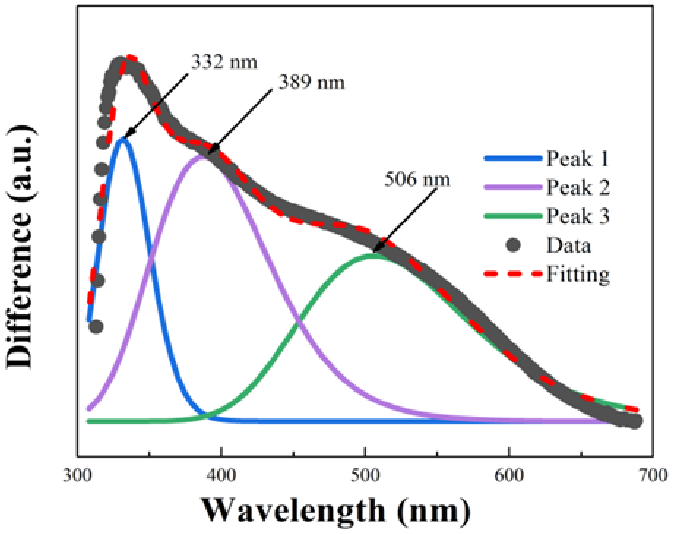

Fig. 5-3 Induced absorption spectra caused by the reddish color.

$V_o^{\bullet\bullet}$ in ZnO was 2.2 eV (563 nm).[13)] Color centers at 610 nm (2.02 eV) was attributed to $V_o^{\bullet\bullet}$ defects in Er_2O_3.[14)] Therefore, the 506 nm absorption band in the reddish BGO is inferred resulting from the electron centers connected to $V_o^{\bullet\bullet}$, as verified in Chapter 4.

In $PbWO_4$ crystal, the defects corresponding to the absorption bands were proposed, and the commonly accepted viewpoint is that 350 and 420 nm absorption bands are related to hole centers connected to V_{Pb}''.[8)] Accordingly, the 332 and 389 nm absorption bands in the reddish BGO could be attributed to the hole centers connected to V_{Bi}''' with three negative charges, as discussed in Chapter 4. The coloration of BGO crystals was caused by the existence of color centers, especially correlating with the distribution of vacancy defects.

5.1.2 Decrease of vacancy defects

By annealing at 850 °C in oxygen atmosphere, the O 1s XPS of the reddish BGO crystal changed, as shown in Fig. 5-4. The peak corresponding to $V_o^{\bullet\bullet}$ (531.8 eV, as mentioned in Chapter 4) decreased obviously. The decrease in $V_o^{\bullet\bullet}$ concentration during the annealing under high oxygen partial pressure could be attributed to the reactions between oxygen in the annealing gas, followed by the diffusion of oxygen ions into the crystal structure to oxygen-deficient regions.15)

$$Bi_4Ge_3O_{12}+V_O^{\cdot\cdot}+\frac{1}{2}O_2 \leftrightarrow O_O+2h^{\cdot} \qquad (5\text{-}3)$$

where $Bi_4Ge_3O_{12}$ denotes the whole crystal. The atom in BGO crystal on a lattice does not keep static, but hops around the center of balance position.8) When annealed at 850 °C, oxygen might diffuse into the BGO lattice, thereby filling the $V_o^{\cdot\cdot}$ affecting the color center. Consequently, the absorption band disappeared directly.

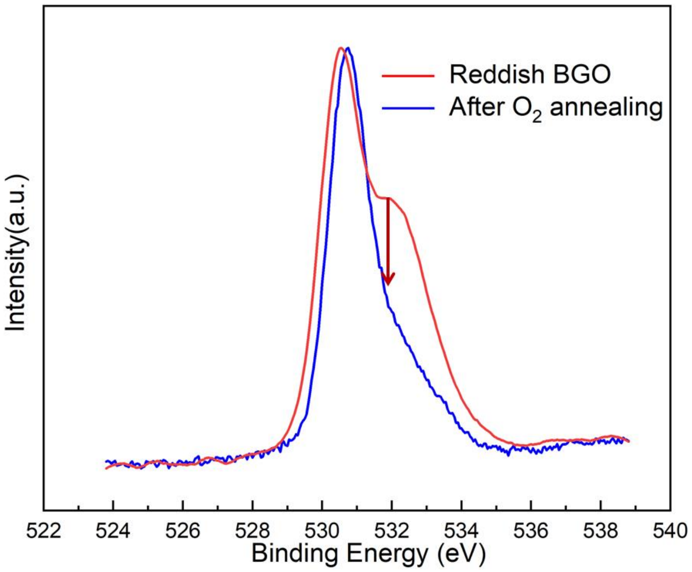

Fig. 5-4 O 1s XPS of the reddish BGO samples before and after annealing.

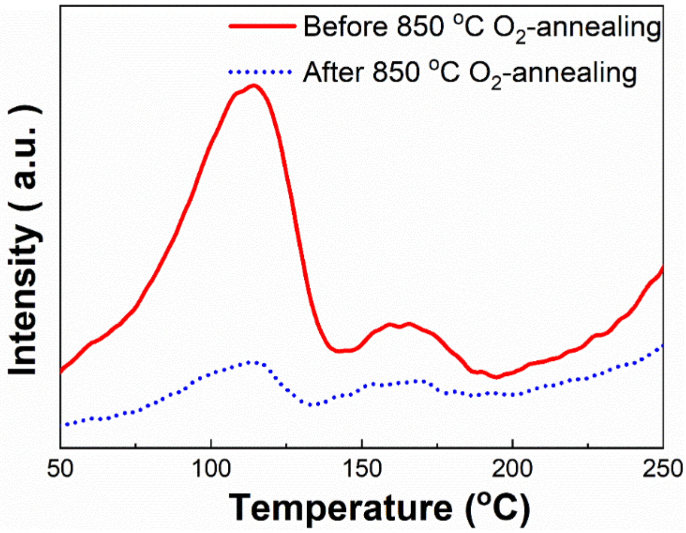

Fig. 5-5 TL curves of the reddish BGO before and after oxygen annealing.

In the reddish BGO, the stimulated carriers could be captured by the traps caused by ion vacancies.8) When the reddish BGO crystals were heated to high temperature, the captured carriers could be released out and form a complex with the capture center providing signals of TL. Fig. 5-5 displays a remarkably difference glow curves between the before and after annealing. Two strong peaks appeared at 120°C and 160 °C in the reddish BGO sample. However, after annealing, only a broad, weak peak was observed.

The temperature position of TL peak depended on the depth of the trap. The higher the temperature corresponded to TL peak, the deeper the trap existed in crystal.16) Hence, at high intensity corresponding to TL peak, a large amount of the traps (vacancy density) existed in the reddish BGO crystal. After annealing in oxygen at 850 °C for 4 h, the main peak intensity of TL glow curve markedly decreased, resulting in decreasing numbers of $V_o^{\bullet\bullet}$ and V_{Bi}'''.

5.1.3 Improvement of scintillation properties

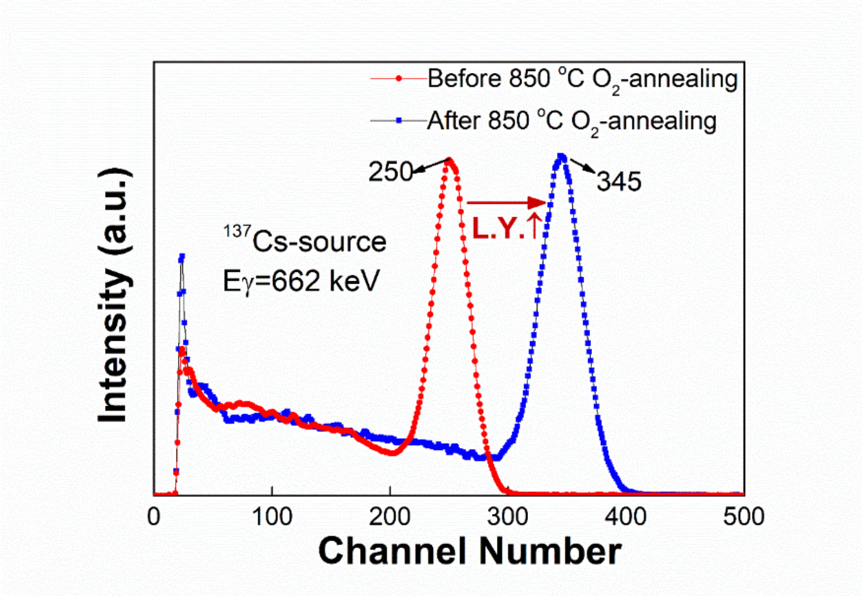

Fig. 5-6 LO before and after annealing under oxygen atmosphere.

With the decrease of vacancies, the optical transmission was also significantly improved. Fig. 5-6 shows the channel number of LO increased remarkably from 250 channels to 345 channels. Moreover, the FWHM of luminescent peak became narrower, resulting in increased ER, as shown in Fig. 5-7. Modified oxygen-annealing was the most effective way to eliminate the reddish of BGO crystals, and this process greatly improved the optical transmission and scintillation properties.

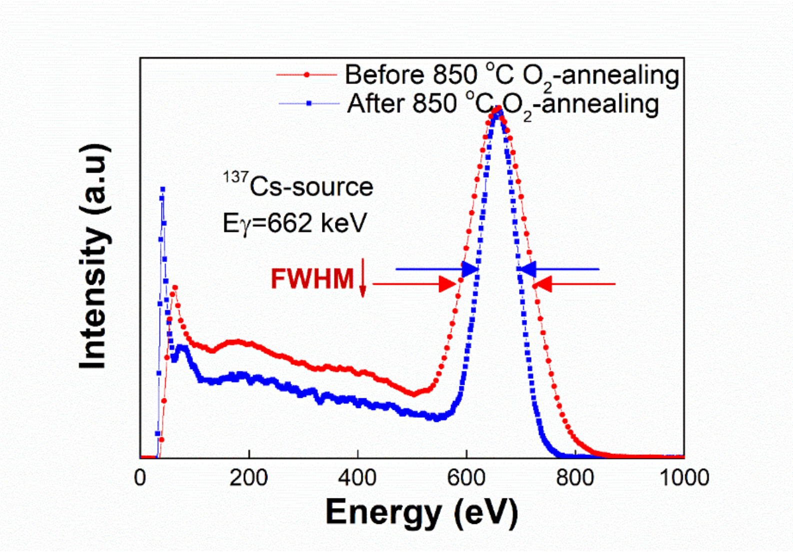

Fig. 5-7 ER before and after annealing under oxygen atmosphere.

5.2 Non-oxidizing atmosphere annealing

5.2.1 Transmission changes in non-oxidizing atmosphere

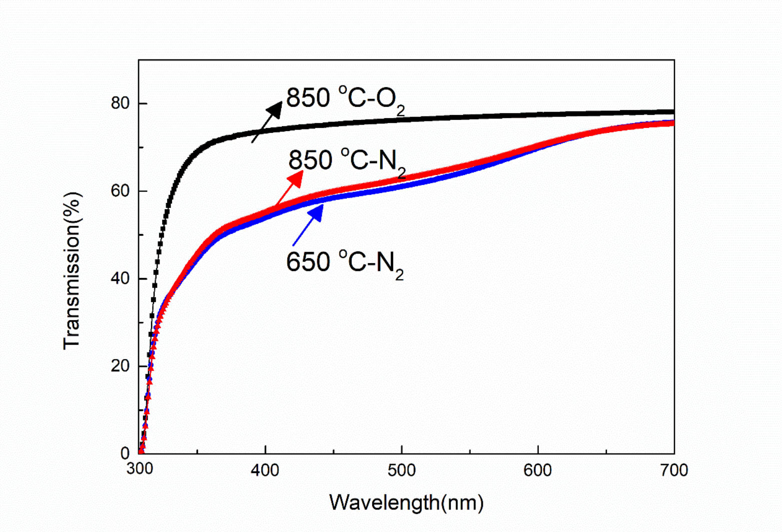

Fig. 5-8 Transmission changes of the reddish BGO annealed at different temperatures in nitrogen atmosphere.

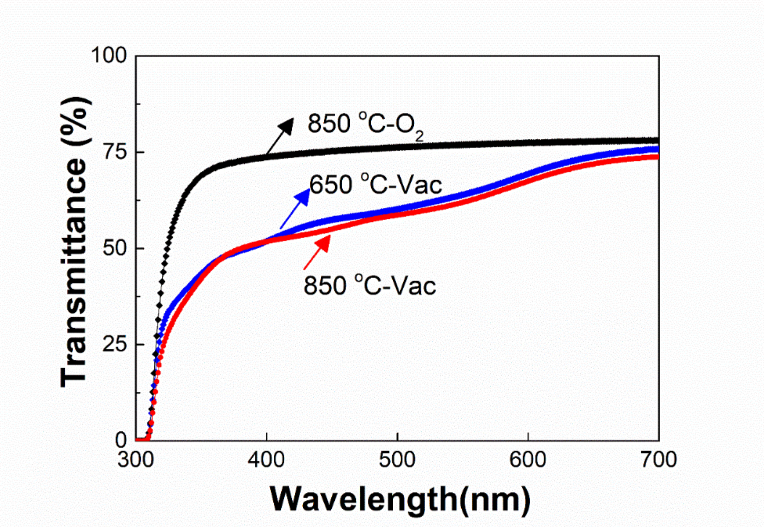

Fig. 5-9 Transmission changes of the reddish BGO annealed at different temperatures in vacuum

However, the annealing of the reddish BGO crystal in a non-oxidizing atmosphere (vacuum and nitrogen) showed distinct results. Figs. 5-8 and 5-9 show the transmission changes of the reddish BGO annealed at different temperatures in vacuum and nitrogen atmospheres, respectively. After annealing below 650 °C, the properties of reddish BGO crystals showed no changes in terms of color and optical transmittance. Even if the annealing temperature was increased to 850 °C, the transmission of the reddish crystal was not enhanced. Therefore, the reddish crystal annealed under the optimized oxygen conditions were more effective than that in vacuum or nitrogen. And the improvement and the partial pressure of oxygen in annealing atmosphere were related.

5.2.2 SEM-EDS analysis

A new phenomenon was also observed. The surface of annealed crystals melted slightly, and a large amount of yellow powder was found attached to the chamber exit of the furnace (Fig. 5-10 (a)). SEM-EDS analysis was performed to obtain the microstructure evolution as well as the elemental composition of the yellow powder surface. Further analysis was carried out by SEM to quantitatively identify the composition of the yellow powder (Fig. 5-10 (b)).

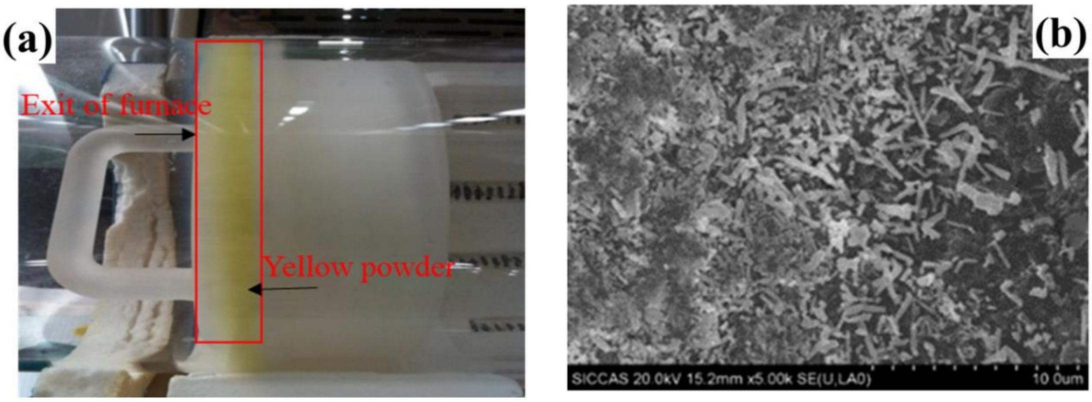

Fig. 5-10 Yellow powder appeared at the exit of furnace chamber after annealing at 850 °C for 4 h in vacuum and nitrogen (a) and SEM images of the yellow powder (b).

Table 5-2 EDS analysis of yellow powder deposited on the chamber exit of the atmosphere furnace after annealing of BGO crystal in vacuum and nitrogen for 4 h.

Element	Weight (%)	Atomic (%)
O	19.97	73.90
Si	0.83	1.74
Ca	1.61	2.38
Bi	77.59	21.98
Totals	100.00	100.00

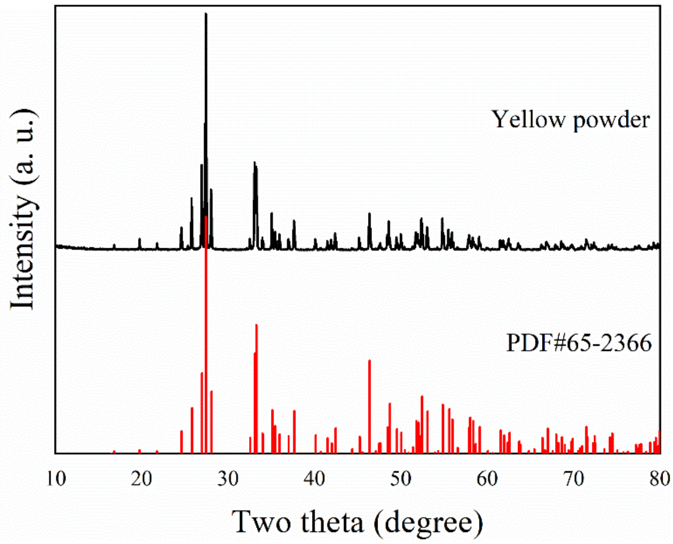

Fig. 5-11 XRD results of the powder samples are well-matched with the standard card PDF# No:65-2366

Table 5-2 presents that the yellow powder is Bi_2O_3, and the content of Bi reached 78%. The XRD pattern of the powder samples was measured, and the results well-matched the standard card PDF# No:65-2366, as shown in Fig. 5-11. Bi and O escaped from as-grown BGO crystal. Thus, $V_o^{\bullet\bullet}$ and V_{Bi}''' appeared in the crystal correspondingly.

5.3 EPR spectra in different atmosphere

The EPR signal is attributed to the paramagnetic singly ionized $V_o^{\bullet\bullet}$. Fig. 5-12 shows the EPR spectra after various annealing treatments of the reddish BGO at different atmospheres (oxygen, vacuum, and nitrogen) to testify the change of $V_o^{\bullet\bullet}$.

The signal intensity at $g = 2.0035$ corresponding to $V_o^{\bullet\bullet}$ decreased with annealing in the oxygen atmosphere, demonstrating that the number of $V_o^{\bullet\bullet}$ in the reddish BGO decreased, according to Eq. 5-4.[17] Through the modified oxygen annealing, the involvement of two trapped electrons defects $V_o^{\bullet\bullet}$ was removed, and an increase in the lattice order caused these complex vacancies to disappear.[18]

$$V_O^{\cdot\cdot} + 2e' + \frac{1}{2}O_2 \leftrightarrow Bi_4Ge_3O_{12} \tag{5-4}$$

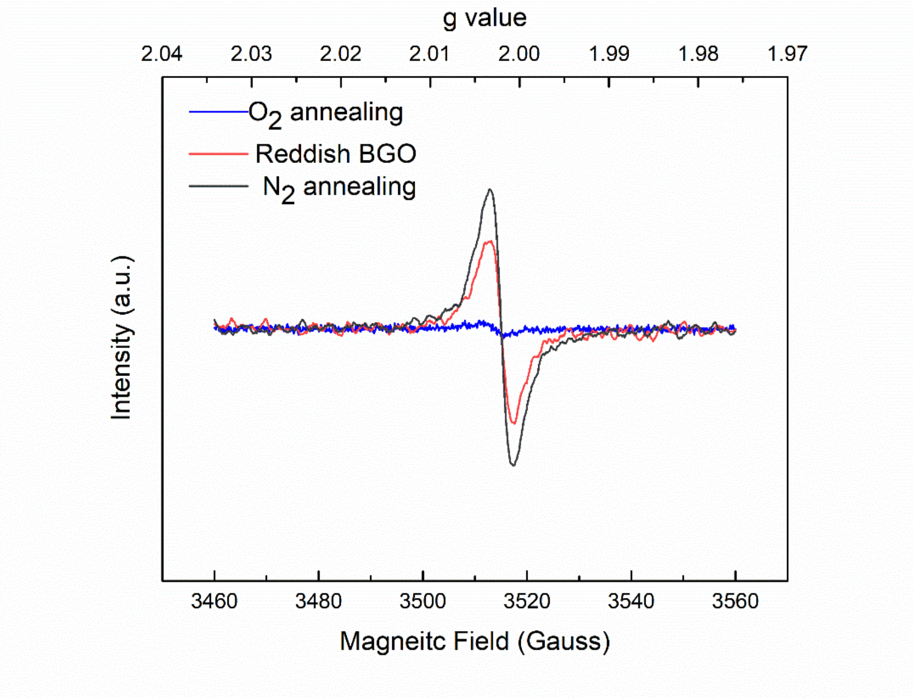

Fig. 5-12 EPR spectra of the reddish BGO sample, after N_2, and O_2 annealing.

Conversely, when it is annealed in a non-oxidizing atmosphere (vacuum and nitrogen) at high temperature, the intensity of EPR signal became larger indicating the generation of more $V_o^{\bullet\bullet}$.[18)]

5.4 Formation mechanism of vacancy defects

While annealed in reducing atmospheres, the partial pressure of oxygen was low. The $V_o^{\bullet\bullet}$ was not decreased by annealing, but O in BGO crystals was easily released. Accordingly, the escape of Bi led to the stoichiometric deviation and collapse of crystal lattices. Correspondingly, the amounts of $V_o^{\bullet\bullet}$ and V_{Bi}''' did not decrease. Therefore, the color of the reddish crystal would not disappear, and the scintillation properties of crystal could not be improved.

The formation of vacancies that could be written as follows:

$$2Bi_{Bi} + 3O_O \rightarrow 2V_{Bi}''' + 3V_O^{\cdot\cdot} + Bi_2O_3 \qquad (5\text{-}5)$$

Based on the above analysis, the reddish BGO crystal was resulted from the color center induced mainly by $V_o^{\bullet\bullet}$ and V_{Bi}'''. The generation of vacancies in the crystals might be attributed to the growth environment. In a practical crystal growth process, some ion vacancies remained in the crystal at high temperature. The activation energy of an oxide was different from that at RT, indicating the presence of ion vacancies. This conclusion was applicable to the preparation of any oxide materials. The equilibrium amount of ion vacancies in crystal depended on the temperature of crystal.[19)]

$$N = N_0 \exp\left(-\frac{Ev}{KT}\right) \qquad (5\text{-}6)$$

where N is the equilibrium amount of ion vacancies in BGO crystals, E_v is the activation energy forming ion vacancies, K is the Boltzman constant, and T is the absolute temperature.

When the growth parameters at high temperature fluctuated in the growth process of BGO, crystal structure could be imperfect. For example, the $V_o^{\bullet\bullet}$ and V_{Bi}''' in crystals could not hop to surface of the crystal. The ion vacancies could act as electron/hole traps that easily made crystals induced color.$^{20\text{-}22)}$

While oxygen compensation was given by thermal annealing in an oxygen atmosphere, the amount of $V_o^{\bullet\bullet}$ and V_{Bi}''' was reduced, and the BGO crystal structure became close to a relatively perfect lattice. Oxygen annealing could efficiently reduce the $V_o^{\bullet\bullet}$ and produce positive electrons according to Eq. 5-7. Then, the V_{Bi}''' with three negative charges, could recombine with the positive electrons to produce optically inert V_{Bi} (Eq. 5-8), and color absorption was not induced.

$$\frac{1}{2}O_2 + V_O^{\cdot\cdot} \leftrightarrow O_O + 2h^{\cdot} \qquad (5\text{-}7)$$

$$3 \times 2h^{\cdot} + 2V_{Bi}'''' \leftrightarrow 2V_{Bi} \qquad (5\text{-}8)$$

5.5 Summary

The reddish crystal was characterized by using the absorption bands in the visible range at 506, 389, and 332 nm and a significant decrease of optical transmissions was observed at 480nm. The reddish BGO crystal was mainly correlated with the distribution of $V_o^{\bullet\bullet}$ and V_{Bi}''', resulting in the presence of color centers. A modified oxygen-annealing was applied to eliminate the reddish color in BGO crystal, reducing the amount of $V_o^{\bullet\bullet}$ and V_{Bi}''' by oxygen compensation, and the BGO crystal structure became more complete accordingly. Based on the comparison of optical performance, the absorption bands in the visible range of the reddish BGO disappeared after annealing, and this phenomenon greatly improved the LO and ER. The intensity of EPR decreased in the oxidizing atmosphere annealing treatment but increased in the non-oxidizing atmosphere treatment. And the reddish color could not be removed by annealing in reducing atmosphere, which was also a significant evidence that there was a relationship between the effectiveness and the partial pressure of oxygen in annealing atmosphere. The essence of annealing at a certain temperature was the exchange of oxygen components between crystals and the environment to modify vacancy defects in the BGO crystals.

References

1) M.J. Weber, and R.R. Monchamp, J. Appl. Phys. **44**, 5495 (1973).
2) R. Moncorgé, B. Jacquier, and G. Boulon, J. Lumin. **14**, 337 (1976).
3) V. Vaithianathan, S. Kumaragurubaran, P. Santhanaraghavan, N. Muralidhar, R. Kumar, A.K. Sinha, P. Ramasamy, and T. Nagarajan, Mater. Chem. Phys. **74(2)**, 121 (2002)
4) Z.S. Macedo, A.L. Martinez, and `A.C. Hernandes, Mater. Res. **6(4)**, 577 (2003).
5) Y.A. Borovlev, N.V. Ivannikova, V.N. Shlegel, Ya.V. Vasiliev, and V.A. Gusev, J. Cryst. Growth. **229(1)**, 305 (2001).
6) Z. Ji, H. Ni, L. Yuan, J. Chen, and S. Wang, Nucl. Instrum. Methods Phys. Res. Sect. Accel. Spectrometers Detect. Assoc. Equip. **753**, 143 (2014).
7) L. Yuan, H. Ni, Z. Ji, J. Chen, G. Song, X. Qi, X. Li, S. Sun, and S. Wang, IEEE Trans. Nucl. Sci. **65**, 1403 (2018).
8) R. Zhu, Nucl. Instrum. Methods Phys. Res. Sect. Accel. Spectrometers Detect. Assoc. Equip. **413**, 297 (1998).
9) P. Yu, L. Su, H. Zhao, and J. Xu, J. Lumin. **154**, 520 (2014).
10) L. Yuan, H. Ni, J. Chen, X. Qi, X. Li, T. Karaki, and D. Wang, Jpn. J. Appl. Phys. **61**, SB1017 (2022).
11) D. Ma, and R. Zhu, Nucl. Instrum. Methods Phys. Res. A **333**, 422 (1993).
12) Z. Ji, H. Ni, L. Yuan, J. Chen, and S. Wang, Nucl. Instrum. Methods Phys. Res. Sect. Accel. Spectrometers Detect. Assoc. Equip. **753**, 143 (2014).
13) W.C. Lim, J.P. Singh, Y. Kim, J. Song, K.H. Chae, and T.Y. Seong, Vacuum. **183**, 109776 (2020).
14) M. Yu, and Z. Zhao, J. Lumin. **225**, 117361 (2020).
15) B. Yang, S. Oh, and Y.J. Kim, IEEE Trans. Nucl. Sci. **61**, 2071 (2014).
16) G. Hu, S. Wang, Y. Li, L. Xu, and P. Li, Ceram. Int. **30**, 1665 (2004).
17) Santosh K. Gupta, P. S. Ghosh, N. Pathak, and R. Tewari, RSC Adv. 5 56526 (2015).
18) L. Zhang, L.Wang, and Y. Zhu, Adv. Funct. Mater. **173**, 781 (2007).
19) R. Zhu, X. Li, Z. Fu, J. Chen, H. Xu, and H. Luo, Ceram. Int. **45**, 13354 (2019).

20) R.A. Jackson, and M.E.G. Valerio, Nucl. Instrum. Methods Phys. Res. Sect. B Beam Interact. Mater. At. **218**, 145 (2004).

21) M. Couzi, J.R. Vignalou, and G. Boulon, Solid State Commun. **20**, 461 (1976).

22) B.C. Grabmaier, and R. Oberschmid, Phys. Status Solidi A. **96**, 199 (1986).

Chapter 6 Assessment and Improvement on the Properties of 600mm-long BGO Crystals

6.1 Assessment of transmittance and light response uniformity

Hundreds of 600 mm-long full-size BGO crystals (shown in Fig. 6-1) play a key role as the direct medium for the possible annihilation of dark matter (energetic electrons and gamma rays) in the Dark Matter detection.1) In the project, they were required with high optical quality and LRU. The LRU here means the difference of the collected light of the PMT excited by gamma rays at different positions along the long axis of the crystal.2-4) In this thesis, it was the first time to investigate the statistical distribution of the LRU on massive growth 600 mm-long BGO crystals. And then post-treatment process studies to optimize initially unsuitable crystals were carried out, including air-annealing, reflective materials, crystal surface treatment with dual-end readout mode, and the specified PMTs according to the design and requirements of DAMPE.5) Characterizations of optical transmittance, ER and LRU of the 600 mm-long full size of BGO crystals were reported.6)

Fig. 6-1 Mass-produced 25 mm × 25 mm × 600 mm BGO crystals grown in SICCAS.5)

6.1.1 Distribution of transmittance

Optical quality of the 25 mm × 25 mm × 600 mm BGO crystals is closely related with the LRU. Fig. 6-2 shows the optical transverse transmission spectrum of one of the mass-produced crystals as a function of wavelength together with the theoretical transmittance limit of BGO (The optical path is 25 mm). The difference of the measured transmittance and T_S may reveal the optical quality of the 600 mm-long BGO crystal. Inset is the distribution of the optical transmittance at 480 nm along the longitudinal direction (600 mm) of the mass-produced 600 mm-long BGO crystals.

The transversal transmittance of the sample was notably in agreement with the theoretical transmittance. The typical longitudinal transmittance at 480 nm approached approximately 72%, although slightly worse than the transversal one. To prove the optical quality of the industrially-grown BGO crystals, the transmittance of hundreds of 600 mm-long BGO crystals along the longitudinal direction was evaluated. Fig. 6-2 inset shows the distribution of the optical transmittance at 480 nm for nearly two hundred crystals. The mean longitudinal transmittance was found to be 67.9% with a width of 4.3%. The fraction of crystals with optical transmittance above 58.0% was about 93.0%.[5)]

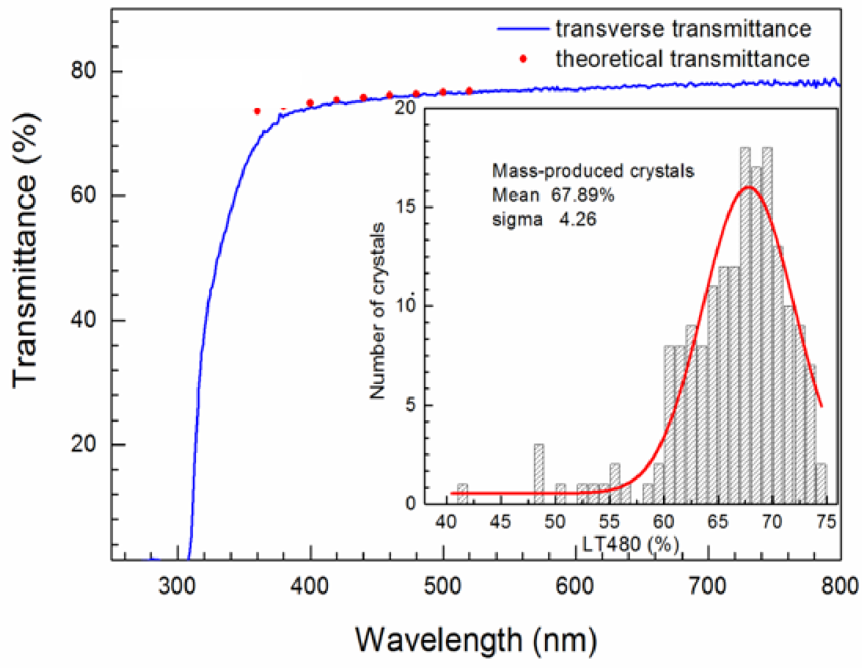

Fig. 6-2 Optical transmission spectrum of a 600 mm-long BGO crystal along the transversal direction.[5)]

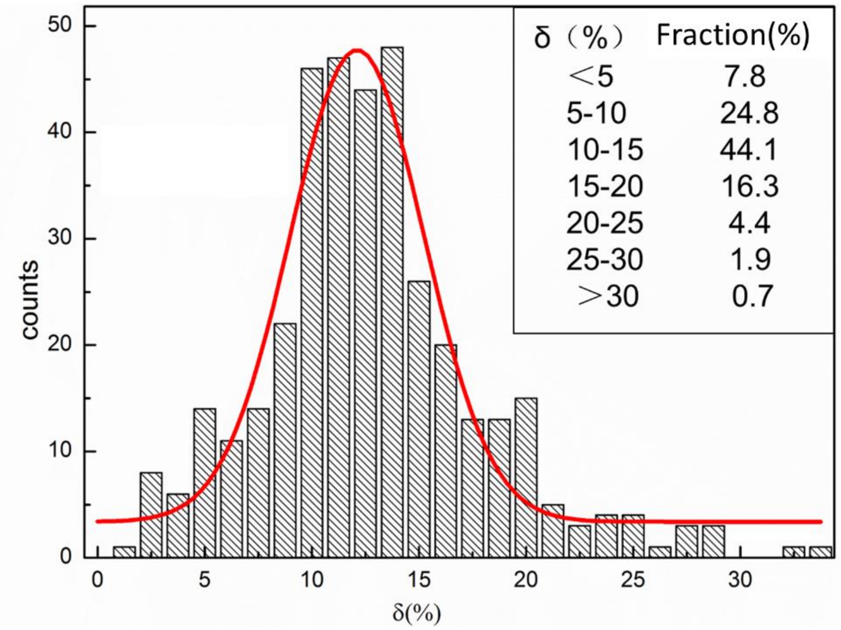

Fig. 6-3 Distribution of the LRU of the mass-produced 600 mm-long BGO crystals.5)

6.1.2 Distribution of light response uniformity

The LRU distribution of the mass-produced 600 mm-long BGO crystals is shown in Fig. 6-3. It was found that around 93% of the as-grown crystals satisfied the DAMPE requirement of the LRU ($\delta \leq 20.0\%$).

6.2 Improvement of transmittance and light response uniformity

The crystals with optical transmittance below 58% at 480 nm and LRU of $\delta > 20.0\%$ did not meet the requirement of the DAMPE detector. The post-treatments were carried out to improve the optical quality and LRU via air-annealing, optimization of reflective materials, and crystal surface treatment.

6.2.1 Effect of air-annealing

The crystals with transmittance below 58% at 480 nm showed the reddish color. The color centers in the reddish BGO were commonly correlated with $V_o^{\bullet\bullet}$.7,8) The $V_o^{\bullet\bullet}$ were the featured point defects in oxide scintillators.9,10) Two reddish samples named Sample 1 and Sample 2 were selected to conduct the air-annealing at 200 °C for 4 h. The optical transmission spectra before and after air annealing are shown in Fig. 6-4.

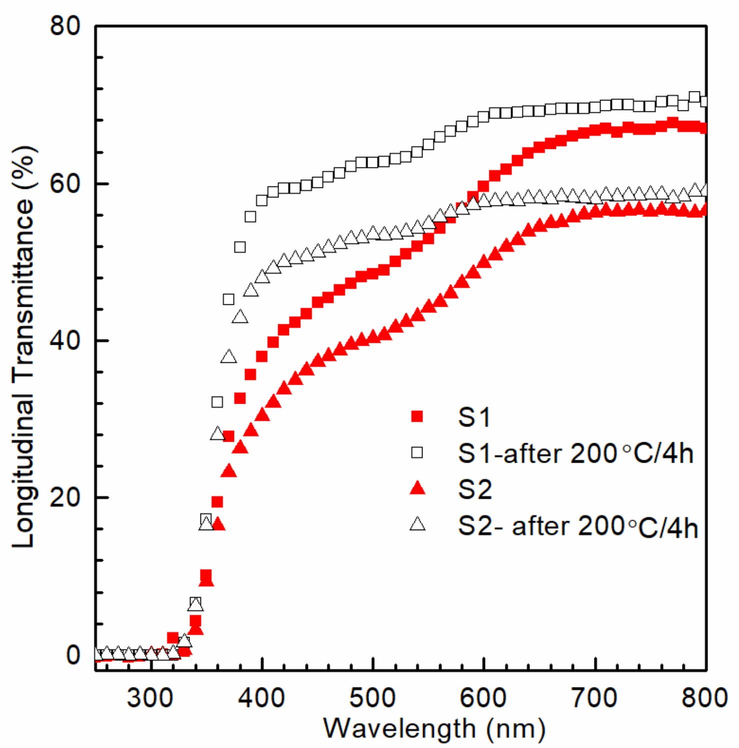

Fig. 6-4 Optical transmission spectra of the 600 mm-long BGO crystals (Sample 1 and Sample 2) along the longitudinal direction before and after air-annealing.5)

Table 6-1 Longitudinal transmittance value at 480 nm before and after air-annealing5)

Sample number	Transmittance of as-grown crystals (%)	Transmittance of air-annealed crystals (%)	Improvement (%)
Sample 1	47.29	62.18	14.89
Sample 2	39.48	52.85	13.37

For the as-grown crystals, a clear absorption band was observed in both Sample 1 and Sample 2, indicating a low transmittance of 47.29% for the Sample 1 and 39.48% for the Sample 2. The transmittance was greatly improved up to 62.18% and 52.85% after air-annealing, respectively. It implied that the absorption induced by color centers mainly originated from the $V_o^{\bullet\bullet}$ related defects. The specific values are listed in Table 6-1.

The LRU of the Sample 1 before and after air-annealing was evaluated and shown in Table 6-2. The results showed that the average LRU decreased from 32.4% to 18.2% for δ_S, and 30.6% to 16.3% for δ_T after air-annealing. The δ_S and δ_T represent the LRUs of the seed and the tail end readout, respectively. It was clear the enhancement of optical transmittance of the crystals positively contributed the LRU. It was worth of mentioning that the annealed samples almost satisfied the LRU standard δ ⩽ 20.0%.

Table 6-2 LRU of as-grown crystal and after air-annealing[5)]

Sample 1	Transmittance at 480 nm (%)	δ_S/±0.8%	δ_T/±0.8%
As-grown	47.29	32.4	-30.6
After air-annealing	62.18	18.2	-16.3

Table 6-3 δ_s and δ_T of BGO crystals wrapped with different reflective materials[5)]

Reflective materials	Thickness of materials (mm)	Emission-weighted reflection (%)	δ_S/±1.2 (%)	δ_T/±1.1 (%)
ESR	0.06	99.10	2.9	-2.2
Teflon	0.15	92.16	7.1	-6.6
Black paper	0.42	6.29	16.6	-14.0

6.2.2 Effect of reflective materials

According to Ref. 11, the higher the reflectivity of the materials used for wrapping crystals, the higher the LO and ER of the scintillation crystals. Three different reflective materials were tested for the LRU, namely, ESR, Teflon, and black paper. The properties of the reflective materials and the LRU of 600 mm-long BGO crystal wrapped with these reflective materials are listed in Table 6-3.

It was found that the use of ESR with highest emission-weighted reflection could achieve the best LRU about δ_s = 2.9% and δ_T = 2.2%, which were much better than the δ_s = 7.1% and δ_T = 6.6% for Teflon and δ_s = 16.6% and δ_T = 14.0% for black paper. It was clear that high reflectivity materials could significantly improve the LRU. As the increase of reflectivity of the reflective materials, the proportion of photons lost from the crystal decreased. The enhancement of the collection efficiency resulted in an increase in the average LO, which led to the improvement of the LRU.

6.2.3 Effect of surface treatments

It was reported that the crystal surface finish could also alter the light response of the scintillation crystals$^{12)}$ and affect the light collection efficiency (LCE).$^{13)}$ The LRU could be changed by adjusting the roughness of one or more lateral surfaces of the crystals, such as BGO for L3,$^{14)}$ lead tungstate for CMS,$^{15,16)}$ and LYSO for SuperB$^{17)}$. Therefore, we tried to depolish one side surface to study the LRU of the 600 mm-long BGO crystals.

Table 6-4 LRU of the 600 mm-long BGO crystal with different surface treatments$^{5)}$

Reflective materials	One side surface depolished and five well-polished surfaces		Six well-polished surfaces	
	δ_S/ ±1.2 (%)	δ_T/ ±1.1 (%)	δ_S/ ±1.2 (%)	δ_T/ ±1.1 (%)
ESR	36.0	-33.0	2.9	-2.2
Teflon	41.3	-37.2	7.1	-6.6

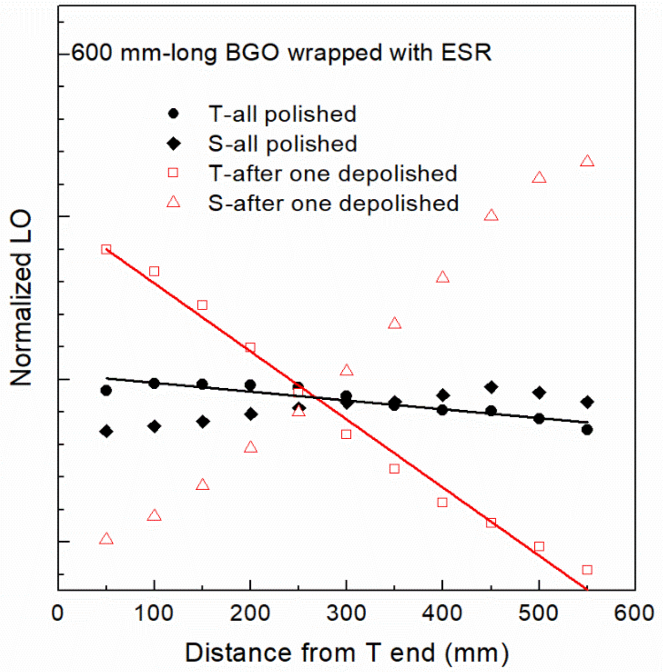

Fig. 6-5 LRU of the 600 mm-long crystal with different surface treatments wrapped with ESR.

The LRUs of the same crystal were compared with two different surface treatments, namely a crystal with six well-polished surfaces and a crystal with five well-polished surfaces and one depolished lateral surface (25 mm × 600 mm) adjacent to the photodetectors. The comparison of the LRU with different surface treatments is listed in Table 6-4.

When using ESR as the reflective material, the LRU of the crystal with all well-polished surface was about 2.9%. For the same crystal with one side surface depolished, its LRU significantly deteriorates to about 36.0%. When using Teflon and black paper as reflective materials, the crystal with one depolished side surface and five well-polished surfaces also showed the worsen LRU compared to the one with all six well-polished surfaces. The harmful effect of surface depolishing could be caused by the direct light scattering on surface, and the multiple light reflection17) due to the change of the surface diffuse reflection on the depolished surface. More quantitatively, the LO at various locations were compared along the longitudinal direction for both surface treatment (Fig. 6-5). The one surface depolishing treatment significantly increased the LO of the crystal when the radioactive source was near the readout end, but severely reduced the LO of the radioactive source away from the readout end. The significant difference caused the variation of LRU. Therefore, it was beneficial to obtain the excellent LRU with a combination of all well-polished surfaces and ESR as high reflective materials.

6.3 Optimal properties of full-size BGO crystals

The quality and scintillation performances of BGO crystals were improved after better understanding the mechanism of crystal growth, optimizing the growth parameters, and reducing defects significantly. The properties of 600 mm-long BGO crystals were enhanced effectively upon the requirements of DAMPE project, and the main scintillation properties of 600 mm-long full-size of crystals are summarized as follows.

6.3.1 Optical transmittance

The longitudinal and transverse transmittance spectra of full-size BGO crystals were measured as a function of wavelength. The results together with the theoretical limit and emission spectrum are in Fig. 6-6.

The transverse transmittance of the 600 mm-long BGO crystal was notably good (76.62%) in the wavelength range of the emission spectrum,6) with optical path of 25 mm. At the maximum emission wavelength (480 nm), the transverse transmittance approached the theoretical transmittance. However, poor longitudinal transmittance, was found, especially below 600 nm wavelength, in contract to the transverse transmittance. The longitudinal transmittance along the 600 mm-long direction at 480 nm was approximately 72.87%, which was much lower than the theoretical value. Compared with the transverse transmittance,6) the absorption edge of the longitudinal transmittance shifted remarkably from 312 nm to 358 nm.

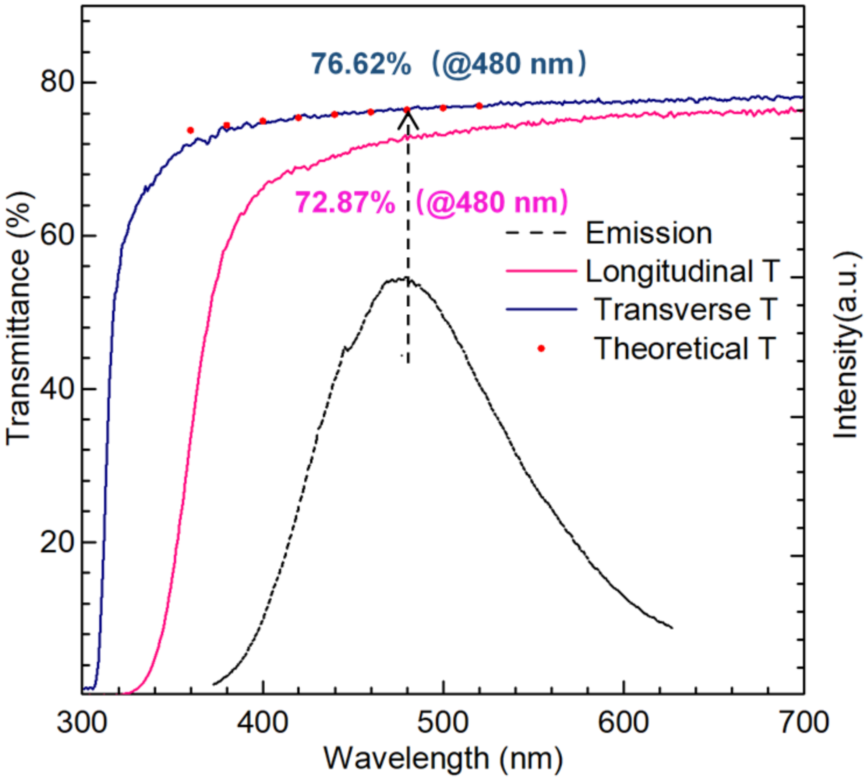

Fig. 6-6 Longitudinal and transverse transmittance spectra are shown for 600 mm-long full-size BGO. The theoretical limit of transmittance and the emission spectrum of BGO are also shown.6)

6.3.2 Energy resolution

The ERs were measured by longitudinal mode and transverse mode. In the transverse mode, it used two PMTs placed on the end faces of BGO to collect LO at eleven positions evenly distributed along the crystal's longitudinal axis, irradiating BGO with a collimated ^{137}Cs γ-rays source. The optical path was 25 mm.

In the longitudinal mode, one PMT was coupled to the one end face of BGO crystal to collect LO, irradiating BGO on another end face with an uncollimated ^{137}Cs. A typical full-size BGO was wrapped with Tyvek, and the gate time was 2000 ns.

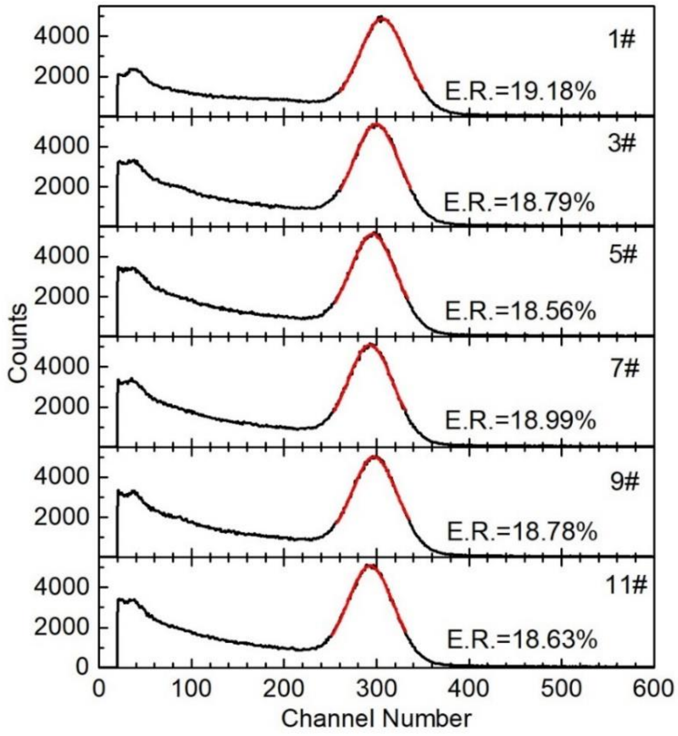

Fig. 6-7 Pulse height spectra (black lines) and corresponding Gaussian fits (red lines) by transverse mode of full-size BGO.$^{6)}$

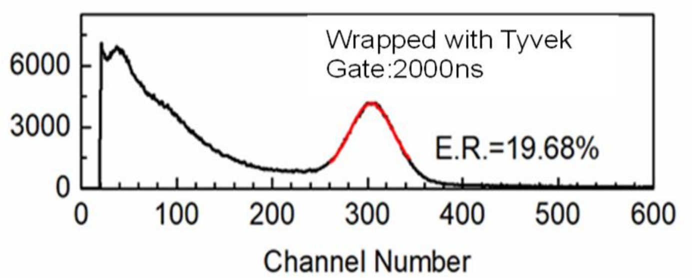

Fig. 6-8 Pulse height spectra (black lines) and corresponding Gaussian fits (red lines) by longitudinal mode of full-size BGO. $^{6)}$

The ERs were achieved approximately 18.80% in the transverse mode by six positions representatively, showing a good uniformity of full-size BGO (Fig. 6-7). In the longitudinal mode (along 600 mm-long crystal), the ER was 19.68%, as shown in Fig. 6-8, while the entire crystal was irradiated from the side with an uncollimated ^{137}Cs.

6.3.3 Light response uniformity

Fig. 6-9 shows the linear fit results of the LRUs wrapped with different reflective materials. The LO gradually decreased as the distance of the irradiation position from the readout end increases. The light collection efficiency photons at the far end from PMT was higher than the near end because the scintillation photons generated at far end from the PMT had to go through a longer light path and more reflections before being detected. This resulted that the light collection efficiency was longitudinal position dependent. It should be noted that the sample showed different sign of δ when the end coupled to the PMT was switched because x was defined as the distance from tail end.

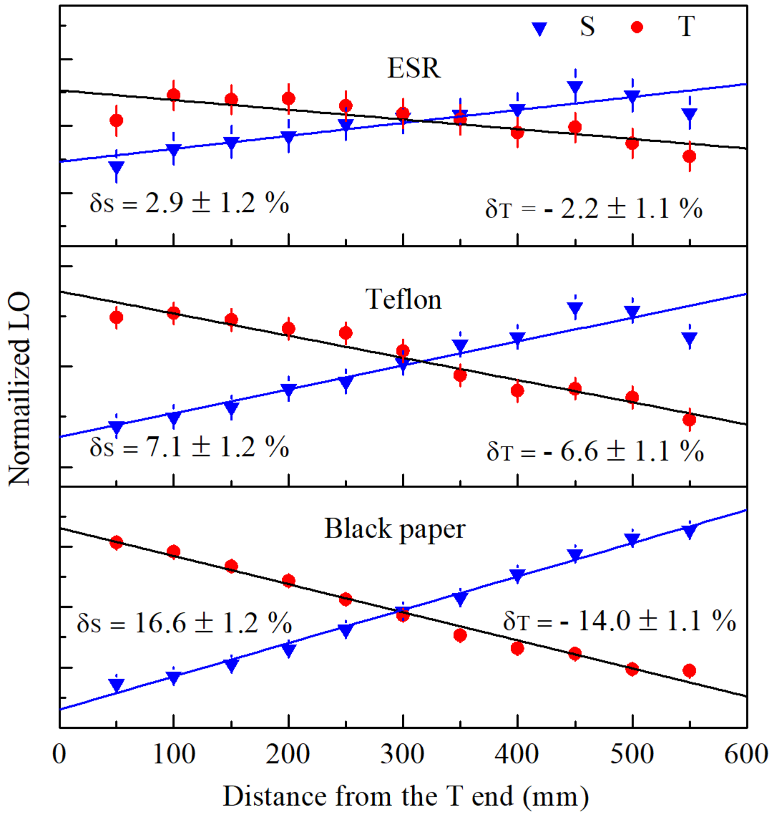

Fig. 6-9 LRU of the 600 mm-long BGO crystal wrapped with different reflective materials by Hamamatsu R5610A PMTs, ESR (a), Teflon (b), and black paper (c).[18)]

The light response uniformity could be achieved to 2.2% at the optimization, while the long BGO crystal as measured from the tail end and wrapped with ESR. The LRU of 600 mm-long BGO crystal with high reflectivity materials primarily depended on internal absorption while relying mostly on the light loss of reflections with low reflective materials.

6.4 Summary

Hundreds of 25 mm × 25 mm × 600 mm-long BGO scintillation crystals were fabricated with high-quality for DArk Matter Particle Explorer (DAMPE). It was found that 93% of produced BGO crystals achieved the DAMPE requirements of $T > 58\%$ and $\mathrm{LRU} \leq 20.0\%$. The optical transmittance and the LRU of the 600 mm-long reddish BGO crystals could be improved by air-annealing at 200 °C via the decreasing of the $V_o^{\bullet\bullet}$ related absorption bands. The LRU could be improved by using of ESR reflective materials, but significantly be deteriorated by the side surface depolishing.

The good optical transmittance was achieved to 76.62% in the transverse mode at 480 nm, and 72.87% in the longitudinal mode at 480 nm for the size of 25 mm × 25 mm × 600 mm BGO for DAMPE. The average ER was achieved approximately 18.80% in the transverse mode, showing a good uniformity of full-size BGO. The ER was 19.68% in the longitudinal mode for the entire crystal. The LRU was achieved up to 2.2%, if the full size of BGO crystal was measured from the tail end and wrapped with ESR.

References

1) The Nobel Prize in Physics 2013, Nobelprize.org. Nobel Media AB., 2014.
2) R. Zhu, Nucl. Instrum. Meth. **340**, 442 (1994).
3) J. Chen, L. Zhang, and R. Zhu, IEEE Trans. Nucl. Sci. **59**, 2224 (2012）.
4) D. Ma, and R. Zhu, Nucl. Instrum. Meth. **333**, 422（1993).
5) L. Yuan, H. Ni, Z. Ji, J. Chen, G. Song, X. Qi, X. Li, S. Sun, and S. Wang, IEEE Trans. Nucl. Sci. **65**, 1403 (2018).
6) Z. Ji, H. Ni, L. Yuan, J. Chen, and S. Wang, Nucl. Instrum. Meth. **537**, 143 (2014).
7) C. L. Melcher, Nature. **313**, 465 (1985).
8) S. G. Raymond, B. J. Luff, P. D. Townsend, X. Feng, and G. Hu, Radiat. Meas. **23**, 195 (1994).
9) F. Meng, Y. Wu, M. Koschan, C. L. Melcher, and P. Cohen, Physica. Status. Solidi. **252**, 1394 (2015).
10) C. Wang, D. Ding, Y. Wu, H. Li, X. Chen, J. Shi, Q. Yang, L. Ye, and G. Ren, Applied Physics A. **123**, 1 (2017).
11) J. Chen, L. Zhang, and R. Zhu, IEEE Trans. Nucl. Sci. **52**, 3133 (2015).
12) J. S. Huber, W. W. Moses, M. S. Andreaco, M. Loope, C. L. Melcher, and R. Nutt, Nucl. Instrum. Meth. **437**, 374 (1999).
13) F. Vittori, F. Notaristefani, T. Malatesta, and D. Puertolas, Nucl. Instrum. Meth. **452**, 245 (2000).
14) E. Auffray, F. Cavallari, M. Lebeau, P. Lecoq, and M. Schneegans, Nucl. Instrum. Meth. **486**, 22（2002).
15) L. Zhang, R. Mao, F. Yang, and R. Zhu, IEEE Trans. Nucl. Sci. **61**, 483 (2014).
16) Y. Wu, A. Lindsey, M. Zhuravleva, M. Koschan, and C. L. Melcher, CrystEngComm. **18**, 7435 (2016).
17) D. Britton, M. Ryan, and X. Qu, Nucl. Instrum. Meth. **540**, 273 (2004).
18) Z. Ji, A Study on Light Response Uniformity of 600mm Long BGO Crystals for Dark Matter Detection in Space[M], Shanghai Institute of Ceramics, Chinese Academy of Science, 2013 (in Chinese).

Chapter 7 Conclusions and Future Works

7.1 Conclusions

Hundreds of 600 mm-long BGO crystals were grown successfully by the novel MVB method. The scintillation properties were effectively improved, especially for the high optical quality and LRU parameters, consequently fully satisfying the application of large-size electromagnetic calorimeter in the DAMPE of China. The conclusions pertaining to the growth, defect formation, and scintillation performances of 600 mm-long BGO crystals can be summarized as follows.

1. The methods of growth and characterization were investigated on 600 mm-long BGO crystals. The high-quality BGO crystals with an as-grown size of 680 mm in length were prepared successfully by the MVB method after the growth parameters were optimized through many efforts and trials.
2. The formation mechanisms of various defects were analyzed by dynamic thermal equilibrium, shape control of the solid–melt interface, and surface reaction of $[GeO_4]^{4-}$ and $[BiO_6]^{9-}$ growth units. The macro-defects, particularly the scattering particles and impurity cores, were significantly reduced in as-grown 600 mm-long BGO crystals. The scattering particles were uniformly distributed in the whole crystal, and they were caused by the convex solid–melt interface due to the fluctuation of growth parameters and effectively reduced by adapting the thermal equilibrium for the crystallization.
3. The impurity core was another type of macro-defect located at the tail section of the BGO crystals. The impurity core was resulted from the concave solid–melt interface by the over-high heating power applied to compensate for the thermal conduction at the later period of crystal growth. The impurity core was remarkably reduced by balancing power heating and thermal conduction during the crystal growth rather than by addressing the over-high temperature gradient at the solid–melt interface.

4. The reddish BGO was found occasionally in the as-grown 600 mm-long crystals, with absorption peaks of 506, 389, and 332 nm. The optical absorptions were originated from the point defects, and their transmittance seriously decreases at the wavelength of 310 – 390 nm near the absorption edge of the energy gap of BGO crystals. No clear correlation was found in the trace impurities between reddish and colorless BGO.
5. It was verified that the formation mechanism of the reddish color was caused by the defects $V_o^{\bullet\bullet}$ and V_{Bi}'''. The color centers were identified via several techniques of structure analysis. The $V_o^{\bullet\bullet}$ was verified by the EPR peaks for the reddish BGO crystal, in which an intense signal of $g = 2.0035$ was typical of a singly ionized $V_o^{\bullet\bullet}$.
6. Bismuth with low valence states was inferred to exist in the reddish BGO by XPS. And the existence of V_{Bi}''' was verified by SEM-EDS analysis. The low Bi content in the lattice caused the reddish color of the BGO. The existence of V_{Bi}''' was also cross-checked via HADDF analysis, which was easily produced by Bi_2O_3 evaporation at high temperature during crystal growth.
7. These findings above confirmed that the reddish color could be largely removed via oxygen annealing rather than by reducing atmosphere. The EPR intensity of the $V_o^{\bullet\bullet}$ decreased, which also fitted well with XPS peaks in the annealing treatment at the oxidizing atmosphere. However, the intense signal increased in the annealing treatment at the non-oxidizing atmosphere. Oxygen compensation was provided by oxygen annealing, achieving a perfect lattice to significantly increase the optical transmission, LO, and ER.
8. The reason behind the process of how to eliminate the reddish color in the BGO crystals were clarified. Oxygen annealing could efficiently reduce $V_o^{\bullet\bullet}$ and produce positive holes, and then V_{Bi}''' with three negative charges could be recombined with positive holes to produce optically inert V_{Bi}.
9. Several techniques were adopted to enhance the LRU of the single-crystal BGO with a size of 25 mm × 25 mm × 600 mm. An effective approach was to increase LRU at the temperature of 200 °C for 4 h. Side-surface depolishing had no

improvement, and could even deteriorate the LRU. Eventually, the LRU could be improved from the unsuitable BGO into an excellent one for DAMPE application via post-treatment approaches, including wrapping the materials with ESR and the air-annealing process.

10. Good optical transmittance could be achieved in the scintillation wavelength range of 300 – 700 nm. The optical transmittance of the BGO crystals was improved by up to 76.62% in the transverse mode and 72.87% in the longitudinal mode at 480 nm for the full-size (25 mm × 25 mm × 600 mm) crystals. The BGO crystals were suitable for DAMPE project due to their good transmittance for dark matter detection.
11. The average ER was achieved to approximately 18.80% on the 662 keV γ-rays source, and the spacing was uniform along six positions in the 600 mm-long BGO crystal. The ER was 19.68% in the longitudinal mode, while the entire crystal was irradiated from the end face. The LRU was 2.2% when the full-size BGO crystal was measured from the tail end and wrapped with ESR. Wrapping the high-reflectivity material with ESR led to LRU improvement.

7.2 Future works

DAMPE1 has obtained most accurate electron spectrum within 1TeV, but there is a spike-like structure at 1.4 TeV. The BGO crystal is also a promising candidate in building ultra-large-area electromagnetic calorimeters for next-generation detection facilities of dark matter particles in space. Ultra-large BGO crystals (800 – 1000 mm-long) can increase the physical acceptance of particle detection and provide high-quality and reliable detection in higher energy range (~1.4 TeV). However, ultra-large BGO crystals present many challenges for next-generation scintillators.

The results of this thesis provides a foundation and support for the ultra-large BGO growth for the next DAMPE. The mechanism and process of crystal growth are also altered when the size of the BGO crystals is increased. The mechanism of crystal growth will be investigated further, at the aim of successfully building large-size high-quality BGO crystals while guaranteeing that their scintillation performance can meet the material specifications of next-generation electromagnetic calorimeters in DAMPE.

Methods of further addressing other defects, including rare earth metal doping to fabricate high-quality, large-area, and ultra-long BGO for next-generation DAMPE in space, will also be investigated.

Techniques how to reduce the segregation of the impurity of dopant elements, characterization of the structures of defects, and comprehensively understanding of the structure-property relationship, will also be investigated systematically with the aim of enhancing the optical transmittance, LO, ER, and LRU of large-scale BGO crystals.

List of Publications

1) **L. Yuan**, H. Ni, J. Chen, X. Qi, X. Li, T. Karaki, and D. Wang
   "Experimental verification of vacancy defects and their vital role on reddish $Bi_4Ge_3O_{12}$ single crystals",
   Japanese Journal of Applied Physics, Vol. 61, SB1017 (2022).
2) **L. Yuan**, H. Ni, J. Chen, G. Song, X. Qi, X. Li, T. Karaki, and D. Wang
   "Effects of annealing on the optical and scintillation properties of reddish $Bi_4Ge_3O_{12}$ single crystals",
   Ceramics International, Vol. 47, 11856 (2021).
3) **L. Yuan**, H. Ni, Z. Ji, J. Chen, G. Song, X. Qi, X. Li, S. Sun, S. Wang
   "High light response uniformity in industrial growth of 600 mm-long BGO crystals for DArk Matter Particle Explorer",
   IEEE Transactions on Nuclear Science, Vol.65, 1403(2018).

List of Presentations

1) **L. Yuan**, H. Ni, J. Chen, X. Qi, X. Li, T. Karaki and D. Wang: “The origin of the reddish BGO scintillators: vacancy and valence state of ions”, The 8th International Symposium on Organic and Inorganic Electronic Materials and Related Nanotechnologies, Online, Toyama, Japan: Jun. 1-3, 2021.